

CORONARY MOTION MODELING FOR CTA TO X-RAY ANGIOGRAPHY REGISTRATION

COERT METZ

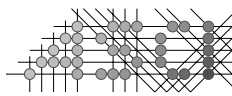
Coronary Motion Modeling for CTA to X-Ray Angiography Registration

Coert Metz

The work in this thesis was conducted at the Departments of Radiology and Medical Informatics of the Erasmus MC, University Medical Center, Rotterdam, The Netherlands and was financially supported by The Dutch Foundation for Scientific Research, NWO, STW and SenterNovem, project IGIT4Health (HTT09011).

Financial support by the Netherlands Heart Foundation for the publication of this thesis is gratefully acknowledged.

Additional financial support for the publication of this thesis was generously provided by the Department of Radiology, Erasmus MC; Erasmus University Rotterdam and the ASCI graduate school.



Advanced School for Computing and Imaging

This work was carried out in the ASCI and COEUR graduate schools.
ASCI dissertation series number 233.

Layout and cover design by Coert Metz.

Printed by GVO Drukkers en Vormgevers BV | Ponsen & Looijen.

ISBN 978-90-6464-473-3

© 2011, C.T. Metz

All rights reserved. No part of this thesis may be reproduced by any means including electronic, mechanical, photocopying, or otherwise, without the written permission of the author.

Coronary Motion Modeling for CTA to X-Ray Angiography Registration

Modelleren van kransslagaderbeweging voor de registratie van CTA met
röntgenangiografie

Proefschrift

ter verkrijging van de graad van doctor aan de
Erasmus Universiteit Rotterdam
op gezag van de rector magnificus

Prof.dr. H.G. Schmidt

en volgens besluit van het College voor Promoties.

De openbare verdediging zal plaatsvinden op
woensdag, 29 juni 2011 om 13.30 uur door

Cornelis Timotheüs Metz

geboren te Ede



Promotiecommissie

Promotor: Prof.dr. W.J. Niessen

Overige leden: Prof.dr.ir. A.F.W. van der Steen
Prof.dr.ir. J.H.C. Reiber
Prof.dr.ir. M. Breeuwer

Copromotor: Dr.ir. T. van Walsum

Contents

1	General Introduction	1
1.1	The Cardiovascular System: Heart and Coronary Arteries	4
1.2	Coronary Artery Disease	5
1.3	Diagnosis of Coronary Artery Disease	5
1.3.1	Conventional coronary angiography	6
1.3.2	Computed tomography angiography	6
1.4	Treatment of Coronary Artery Disease	7
1.5	Percutaneous Coronary Intervention	8
1.6	Integration of Diagnostic and Interventional Information	9
1.6.1	Previous work on the alignment of 3D preoperative coronary CTA data with intraoperative 2D X-ray angiography images	10
1.6.2	This thesis	10
2	Coronary Centerline Extraction From CT Coronary Angiography Images Using a Minimum Cost Path Approach	13
2.1	Introduction	15
2.2	Materials and Methods	17
2.2.1	Imaging data and reference standard	17
2.2.2	Minimum cost path approach	18
2.2.3	Experiments	22
2.3	Results	25
2.3.1	Start point detection	25
2.3.2	Centerline extraction: quantitative evaluation	25
2.3.3	Qualitative evaluation	29
2.3.4	Computation times	29
2.4	Discussion and Conclusions	30
	Acknowledgments	32
3	Standardized Evaluation Methodology and Reference Database for Evaluating Coronary Artery Centerline Extraction Algorithms	33
3.1	Introduction	35
3.2	Motivation	36
3.3	Previous work	37
3.4	Evaluation framework	37
3.4.1	Cardiac CTA data	37
3.4.2	Reference standard	41

3.4.3	Correspondence between centerlines	42
3.4.4	Evaluation measures	44
3.4.5	Observer performance and scores	45
3.4.6	Ranking the algorithms	48
3.5	Algorithm categories	48
3.5.1	Category 1: automatic extraction	48
3.5.2	Category 2: extraction with minimal user interaction	49
3.5.3	Category 3: interactive extraction	49
3.6	Web-based evaluation framework	49
3.7	MICCAI 2008 workshop	49
3.7.1	Fully automatic methods	50
3.7.2	Semi automatic methods	51
3.7.3	Interactive methods	51
3.8	Results	52
3.8.1	Results categorized	53
3.8.2	Algorithm performance with respect to ostium distance	53
3.8.3	More statistics available online	53
3.9	Discussion	55
3.10	Conclusion	55
4	Nonrigid Registration of Dynamic Medical Imaging Data Using nD+t B-Splines and a Groupwise Optimization Approach	61
4.1	Introduction	63
4.1.1	Background	63
4.1.2	Previous work on motion estimation	63
4.1.3	Proposed method	66
4.2	Method	66
4.2.1	Transformation	67
4.2.2	Dissimilarity metric	67
4.2.3	Zero average displacement constraint	68
4.2.4	Optimization	68
4.2.5	Inverse transformation	69
4.2.6	Implementation details	70
4.3	Experiments and results	70
4.3.1	Registration approaches	71
4.3.2	Evaluation measures	73
4.3.3	Quantitative evaluation on synthetic data	73
4.3.4	Quantitative evaluation on 3D+t CT data of the lungs	74
4.3.5	Quantitative evaluation on 3D+t CTA data of the heart	80
4.3.6	Further examples on clinical data	80
4.4	Discussion	82
4.5	Conclusions	84
5	Cardiac Motion Prediction from Single-Phase CTA by Principle Component Regression	85



5.1	Introduction	87
5.2	Method	89
5.2.1	Shape-conditional motion prediction	89
5.2.2	Landmarking	92
5.2.3	Alignment of landmark sequences	95
5.3	Experiments and results	98
5.3.1	Imaging data	98
5.3.2	Landmark propagation	98
5.3.3	Accuracy of shape-conditional and mean motion	99
5.3.4	Training set size	101
5.3.5	Visualization of the relation between shape and motion	103
5.4	Discussion	103
5.5	Conclusions	105
6	Alignment of 4D Coronary CTA with Monoplane X-Ray Angiography: A Feasibility Study	107
6.1	Introduction	109
6.2	Method	110
6.2.1	4D coronary modeling	111
6.2.2	Alignment of 4D coronary model to X-ray sequence	112
6.3	Experiments and results	116
6.3.1	Imaging data	116
6.3.2	Evaluation of registration	117
6.4	Discussion	123
6.5	Conclusion	125
7	Summary and Future Perspectives	127
7.1	Summary	129
7.2	Future perspectives	130
	Bibliography	134
	Samenvatting	150
	Publications	154
	PhD portfolio	159
	Dankwoord	161
	Curriculum vitae	165



1

General Introduction

Clinical diagnosis in a wide range of diseases increasingly relies on medical imaging data. The acquired images contain a wealth of information, which could potentially also improve guidance during minimally invasive interventions. To date, visual feedback during these procedures is often limited to interventional modalities such as X-ray or ultrasound imaging. Efficiently utilizing the additional information from the preoperatively acquired imaging data may have several advantages, such as reduced intervention time, radiation dose and contrast agent usage, or reduced procedural failure.

To fully employ the preoperative imaging data during the intervention the integrated visualization of the image and instruments is needed. Such a visualization requires that the spatial relation between the image and the instruments is known. This relation is often determined indirectly by finding the position of the instruments with respect to a patient coordinate system (often directly related to the coordinate system of the imaging system) and finding the relation between this coordinate system and the preoperatively acquired imaging data (Figure 1.1).

A popular approach to find the relation between the diagnostic image and the patient coordinate system is to align the preoperatively and intraoperatively acquired images by means of image registration techniques. If the target organ is a static structure, such as a bone in orthopedic surgery, it is sufficient to determine the position and orientation of the imaging data with respect to the patient in the intervention room. For soft tissue interventions, such a rigid alignment is often not sufficient, as the tissue is moving non-rigidly due to cardiac motion, respiratory motion or the impact of such motions on the structure of interest.

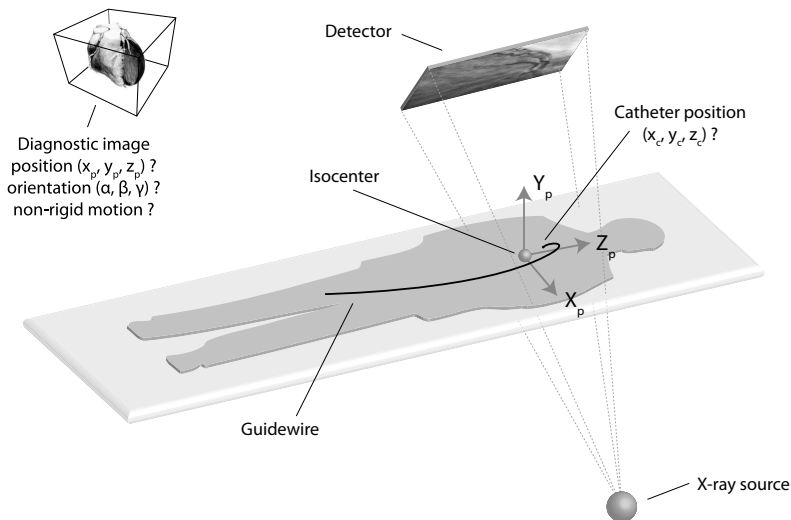


Figure 1.1: Image guidance for interventions relies on knowing the spatial relation between the preoperative imaging data and instruments. This relation is often determined indirectly by finding the position (x_c, y_c, z_c) of the instrument(s) and the position (x_p, y_p, z_p) and orientation (α, β, γ) of the preoperative imaging data with respect to the patient coordinate system (x_p, y_p, z_p).

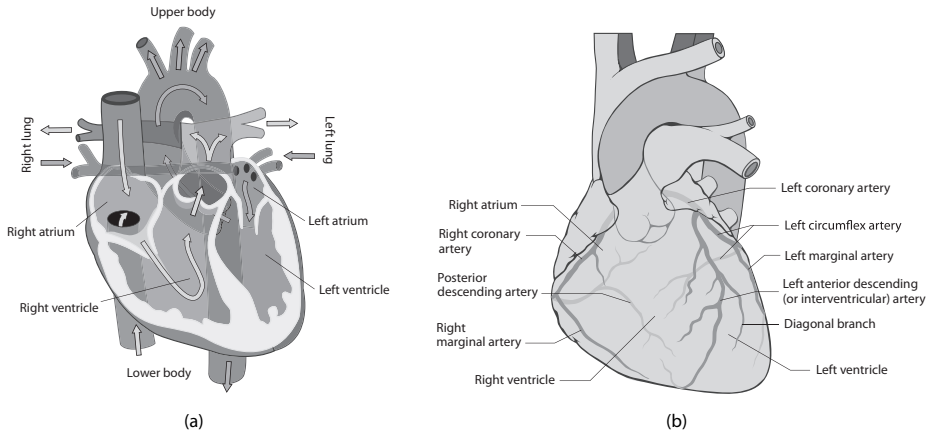


Figure 1.2: (a) The heart is a double pump serving two circuits. The right side of the heart serves the pulmonary circuit; the left side the systemic circuit. The arrows indicate the direction of the blood flow. (b) The heart with the coronary arteries and veins, which form the blood supply for the heart tissue itself.

The goal of the work described in this thesis is to develop and validate techniques to make 3D coronary computed tomography angiography available during percutaneous coronary interventions. The accurate alignment of the preoperative image with the intraoperative situation is very challenging due to the fast and extensive motion of the coronary arteries caused by the cardiac cycle. The main focus of our work is therefore on this alignment problem.

In the remainder of this chapter we provide further information on coronary artery disease, its diagnosis and treatment, challenges encountered during interventions and an overview of the proposed approach to relate diagnostic imaging data of the coronary arteries to the intraoperative situation.

1.1 The Cardiovascular System: Heart and Coronary Arteries

The cardiovascular system is the delivery system of the body (Marieb, 2007). The heart, blood vessels and blood are the main components of this system. They transport oxygen and nutrients to and waste materials from all organs in the body. The heart is the motor of this system and pumps the blood around through the vessels (Figure 1.2(a)). It is a double pump, which serves two circulations: the pulmonary and systemic circuit. The right side of the heart is involved in the pulmonary circuit serving gas exchange. It pumps oxygen-depleted and carbon dioxide-rich blood from the heart to the lungs and returns oxygen rich blood to the left side of the heart. The left side serves the systemic circuit and pumps the oxygen rich blood into the aorta from which it is transported to the body tissues to exchange gases and nutrients. The myocardium is accommodated by the coronary circulation, a subsystem of the systemic circuit (Figure 1.2(b)). It consists of the left and right coronary arteries, which supply oxygen rich blood to the cardiac

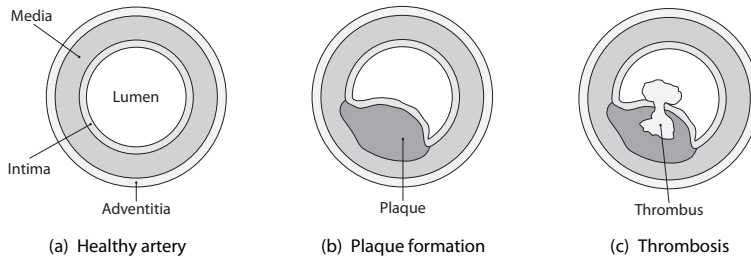


Figure 1.3: (a) A schematic view of a healthy artery wall and its three layers: adventitia, media and intima. (b) Atheromateous plaque builds up just below the intima layer causing lumen narrowing and (c) optionally leading to thrombus formation.

muscle, and veins to transport the deoxygenated blood back to the heart. It is essential that this circulation functions well, as a reduction of myocardial blood supply will affect heart function and may eventually lead to myocardial infarction, commonly referred to as a heart attack.

1.2 Coronary Artery Disease

Coronary artery disease (CAD) is one of the main causes of death worldwide (Brown and O'Connor, 2010) and is caused by atherosclerosis in the coronary arteries. Atherosclerosis is the process in which fatty deposits (also called plaque) build up just below the intima layer inside the vessel wall (Woolf, 1998, Chapter 32). This plaque build up may narrow the lumen, i.e. the cavity through which the blood flows, thus hampering the blood supply to the myocardium. Besides, plaque may rupture, which causes obstruction of the blood flow due to blood clot formation (thrombus). Figure 1.3 gives an illustration of the progression of atherosclerosis in the vessel wall.

1.3 Diagnosis of Coronary Artery Disease

The first symptoms of coronary artery disease occur at moments when the heart is working harder and needs more oxygen, such as during exercise, in periods of emotional stress or after large meals. Corresponding symptoms are chest pain, referred to as angina pectoris, and shortness of breath. When CAD progresses these symptoms may become predictable and always occur when, for example, a certain amount of exercise is performed. These predictable chest pain is called stable angina. A more extreme, but often first symptom of CAD is a heart attack (Davies, 2001).

The diagnosis of CAD is based on medical and family history, risk factors and the results of a physical exam and diagnostic tests and procedures. The physician can, for example, make an electrocardiogram to measure the electrical activity of the heart, perform a stress test to see how the heart performs during physical activity, or test blood to check enzymes, cholesterol level, and other risk factors. When there is a reasonable assumption that the coronary arteries are severely narrowed, imaging techniques may be



Figure 1.4: Typical set-up of (a) a normal angiography room, with a Siemens Artis zee biplane X-ray system and (b) a angiography room enabled for magnetic navigation. In (b) the two magnets left and right of the table generating the magnetic field are clearly visible (images copyright Siemens AG).

applied to determine if significant lesions (narrowing larger than 50%) are present, and whether treatment of the lesions is necessary.

1.3.1 Conventional coronary angiography

Conventional coronary angiography (CCA) is a procedure to visualize the coronary arteries by contrast injection and X-ray imaging. A catheter (long thin flexible tube) is inserted into a blood vessel in the upper thigh via an incision in the groin and transported through the vascular system to the ostium (beginning) of the coronary arteries (Grech, 2011). Subsequently, through this catheter contrast material is injected into the coronary artery to visualize the vessel lumen by X-ray imaging. Sometimes a biplane X-ray system with two X-ray sources and two detectors is used (Figure 1.4(a)), resulting in two X-ray images, (quasi-)simultaneously acquired from different orientations. Examples of coronary angiograms of a left and right coronary artery can be found in Figure 1.5.

1.3.2 Computed tomography angiography

Computed tomography is an imaging modality in which an X-ray source and detector are deployed to measure the attenuation of the tissue at different orientations around the patient. A 3D image is derived from these measurements by computational techniques. Computed tomography angiography (CTA) combines computed tomography with contrast injection, enabling the visualization of the vessel lumen. The temporal and spatial resolution of modern computed tomography make it possible to image the fast moving anatomy of the heart with good image quality and minimal motion artifacts. For this reason, CTA is increasingly used for the diagnosis of CAD (Weustink et al., 2010). Moreover, CTA is less invasive than CCA and provides, next to information about vessel narrow-

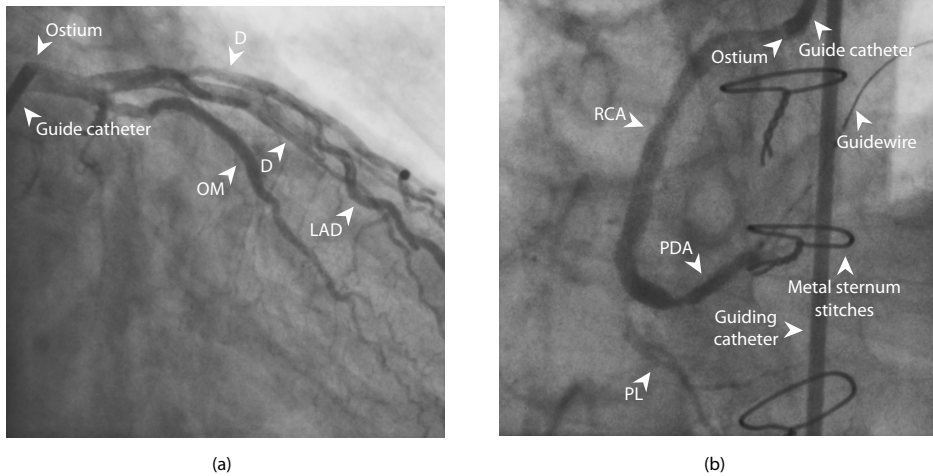


Figure 1.5: Examples of X-ray coronary angiograms of a (a) left and (b) right coronary tree visualizing the lumen of the coronary arteries by contrast injection and X-ray imaging. Clearly visible are the catheter, the guidewire and some metal sternum stitches. The remaining arrows indicate some of the branches of the coronary tree: RCA = right coronary artery, PDA = posterior descending artery, PL = posterolateral branch, LAD = left anterior descending artery, OM = obtuse marginal branch and D = diagonal branch.

ing, information about the composition of the plaque, such as the presence of calcium (Hoffmann et al., 2006; Lehman et al., 2009).

1.4 Treatment of Coronary Artery Disease

Three main therapies for the treatment of coronary artery disease can be distinguished (Kasper et al., 2005):

- (i) **Medication:** patients diagnosed with coronary artery disease often receive medication to reduce heart rate and blood pressure (beta-blockers), prevent blood clots (aspirin), lower cholesterol (statins, calcium channel blockers), relieve symptoms (nitrates), etc.
- (ii) **Minimally invasive coronary interventions:** if a vessel is severely narrowed, minimally invasive procedures to widen the vessel can be applied. Angioplasty is a procedure in which vessels are widened by inflation of a balloon at the site of the lesion, often combined with stent implantation. It was initially described by interventional radiologist Charles Dotter and is often also referred to as percutaneous coronary intervention (PCI, Section 1.5).
- (iii) **Coronary artery bypass surgery:** certain cases are in general less suited for PCI treatment, such as long, heavily calcified stenoses in tortuous vessels or at bifurcations (Grech, 2011). In these cases, coronary artery bypass surgery needs to be performed. In this procedure, blood flow to parts of the myocardium behind the lesion

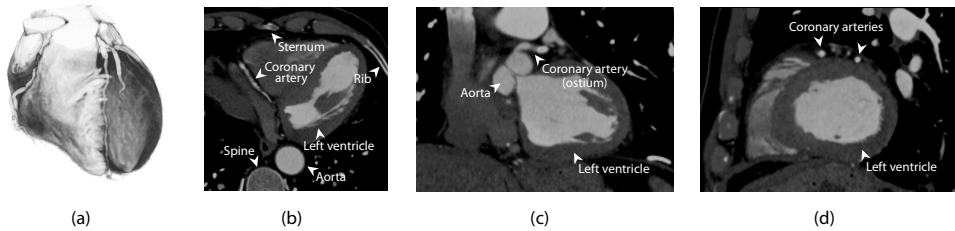


Figure 1.6: A computed tomography angiography scan of the coronary arteries. (a) Volume rendering, (b) Transversal view, (c) Coronal view, (d) Sagittal view.

is restored by grafting arteries or veins from other parts of the body to these areas. It is therefore often also called coronary artery bypass grafting (CABG). CABG is far more invasive than coronary angioplasty, as the chest needs to be opened by the surgeon to be able to reach the heart.

1.5 Percutaneous Coronary Intervention

The target application for our work is PCI. Figure 1.7 gives an overview of this procedure. Similar to CCA, a guide catheter, i.e. a thin long, flexible plastic tube, is inserted into a blood vessel in the upper thigh¹ and moved towards the ostium of the coronary artery. This guide catheter is used to inject contrast fluid into the coronary arteries for visualization purposes and serves as a transport canal for the guidewire that is moved through the coronary artery to the site of the lesion. Once the guidewire is in place, a hollow balloon catheter is positioned over the guidewire and transported to the site of the lesion. At its target location, the vessel can be widened by inflation of the balloon. Often an expandable wire mesh tube (stent), which keeps the vessel open, is initially positioned over the balloon and employed during balloon inflation. During the procedure the cardiologist controls the guidewire and catheters with his finger tips at the end of the wire near the leg. As the whole procedure takes place percutaneously, X-ray imaging is applied to visualize the vessels and equipment. Due to the projective nature of X-ray imaging, the cardiologist needs to make a mental picture of the actual 3-dimensional (3D) situation inside the patient. The use of a biplane X-ray system facilitates this, as two images acquired from different orientations are available.

Even though procedural success rates of over 98% have been reported for PCI, certain lesions remain challenging to treat. Increasing success rate for these cases might increase the number of patients eligible for PCI treatment over the more invasive revascularisation procedure by CABG. Lower procedural success and higher complication rates have, for example, been reported for complex vascular anatomies, bifurcating lesions and chronically totally occluded vessels (Tsuchida et al., 2007; Hoyer et al., 2005).

¹Or less usual in the radial or brachial artery in the arm.

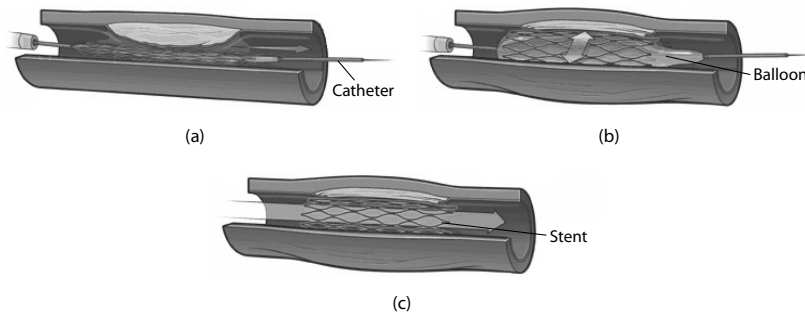


Figure 1.7: Percutaneous coronary intervention with stent placement: (a) a balloon catheter is transported to the lesion site, (b) the vessel is widened and a stent is deployed by inflation of the balloon and (c) bloodflow is increased due to artery widening (images made available by the National Institutes of Health, adapted).

Magnetic navigation in which the tip of the guidewire is magnetically steered through difficult branching points or highly tortuous vessel segments is a promising technique to increase the success rate in these cases (Ramcharitar et al., 2007, 2008, in press, Figure 1.4(b)). Such a system relies on a 3D coronary roadmap, which can be derived intraoperatively from biplane coronary angiography or preoperatively from coronary CTA. A dynamic roadmap is preferred and accurate alignment of the roadmap with the intraoperative situation is essential (Haase et al., 2008, Chapter 42).

Being able to cross the lesion with a wire is an essential requirement for PCI to be successful. In the chronically occluded case, crossing the lesion is difficult, especially in the presence of calcium (Serruys, 2006). Knowing the composition of the plaque at the location of the guidewire is expected to help the surgeon in finding his way through the occlusion. Moreover, when for example, radiofrequency or laser ablation is needed to reopen the total occlusion, knowledge of the location and orientation of the guidewire is essential to prevent dissection or perforation of the vessel wall. Information about the composition of the lesion could potentially be derived from CTA. To this end, accurate alignment of the CTA image with the intraoperative situation and accurate tracking of the guidewire is required.

1.6 Integration of Diagnostic and Interventional Information

From the previous section it is clear that a dynamic roadmap and information about plaque composition from CTA may increase procedural success rate in challenging cases. Additionally, this information could potentially reduce intervention time and thus the amount of contrast dye used and radiation dose delivered to the patient.

A popular approach for aligning preoperatively acquired 3D or 4D images to the intraoperative situation is by 2D/3D registration of the preoperative data to the intraoperative X-ray images. Those methods could be either extrinsic, based on, for example, a stereotactic frame or bone implanted markers, or intrinsic, based on image information (Markelj et al., in press). For successful integration of the preoperatively acquired

information, the position of the instruments should be derived as well, but in this thesis we only address the alignment of the preoperative imaging data with the intraoperative situation.

1.6.1 Previous work on the alignment of 3D preoperative coronary CTA data with intraoperative 2D X-ray angiography images

A limited amount of work on the alignment of coronary CTA with 2D X-ray sequences has been presented previously. Turgeon et al. (2005) proposed a static registration technique to align rotational angiography data to intraoperative X-ray angiography. Their approach is based on segmentation of the coronary arteries from the preoperative imaging data and comparison of the intraoperative angiography images with projections of the resulting coronary model. The method was evaluated in a simulation study using both mono- and biplane X-ray data.

Alignment based on coronary segmentation is a reasonable approach, due to differences in contrast fluid injection between CTA and X-ray acquisitions. In the former, contrast fluid is injected intravenously in the arm, whereas for the latter, it is injected directly in the coronary artery. Therefore, in a CTA scan, all blood cavities, such as the cardiac chambers, coronary arteries and aorta are enhanced, in contrary to the X-ray images, in which only the coronary arteries are enhanced. Projection of both chambers and arteries will result in low contrast projection images, not very well suitable for an intensity based registration approach.

Another approach based on segmentation of the 3D data was proposed by Ruijters et al. (2009). This method additionally employs vessel enhancement filtering on the 2D X-ray images to generate a fuzzy segmentation of the coronary arteries. They show that this approach, together with stochastic optimization, leads to more robust registration results. Again, only static registration at a predefined time point in the cardiac cycle was considered.

The disadvantage of these static approaches is that information from the CTA data can only be used at the time point in the cardiac cycle at which the registration was performed, whereas one would preferable have access to this information for the complete cardiac cycle.

1.6.2 This thesis

The goal of the work described in this thesis is to develop and evaluate techniques that permit the integration of preoperative CTA in the interventional setting. To this end, we create coronary motion models from CTA and register these to intraoperative X-ray angiography sequences. This strategy consists of the following steps:

- (i) **Derivation of a 3D coronary lumen segmentation from the CTA images.** This step is based on first locating the coronary centerlines in the CTA data. In Chapter 2 a minimum cost path approach is developed for this purpose and evaluated based on manually annotated centerlines. In Chapter 3 a publicly available framework for the objective evaluation of coronary centerline extraction techniques is proposed.



After centerline extraction, the lumen is automatically detected by application of an existing segmentation technique (Schaap, 2010, Chapter 5).

- (ii) **Derivation of a motion prior describing the dynamics of the coronary arteries over the cardiac cycle.** In Chapter 4 we propose a registration technique for motion estimation from dynamic medical imaging data, which can, among others, be used for coronary motion estimation from 4D CTA images. For cases in which only 3D CTA is available, a method to estimate a patient-specific motion model based on shape models and regression is proposed in Chapter 5.
- (iii) **Alignment of the CTA data with the X-ray images by 2D+t/3D+t registration.** In Chapter 6 all components are put together for the dynamic alignment of preoperative CTA with the intraoperative situation. The performance of the here outlined strategy is then evaluated on clinical data.

The thesis concludes with a discussion on the results and future research directions (Chapter 7).

2

Coronary Centerline Extraction From CT Coronary Angiography Images Using a Minimum Cost Path Approach

This chapter is based on the manuscript: Coronary Centerline Extraction From CT Coronary Angiography Images Using a Minimum Cost Path Approach, **C.T. Metz**, M. Schaap, A.C. Weustink, N.R.A. Mollet, T. van Walsum and W.J. Niessen, *Medical Physics*, 2009, vol. 36, pp 5568–5579.

Abstract

This chapter describes the application and large-scale evaluation of minimum cost path approaches for coronary centerline extraction from computed tomography coronary angiography (CTCA) data. Two different cost functions are applied. The first is based on a frequently used vesselness measure and intensity information, and the second is an existing cost function based on region statistics. User interaction is minimized to one or two mouse clicks distally in the coronary artery. The starting point for the minimum cost path search is automatically determined using a newly developed method that finds a point in the center of the aorta in one of the axial slices. This step ensures that all computationally expensive parts of the algorithm can be precomputed. The performance of the aorta localization procedure was demonstrated by a success rate of 100% in 75 images. The success rate and accuracy of centerline extraction was quantitatively evaluated on 48 coronary arteries in twelve images by comparing extracted centerlines with a manually annotated reference standard. The method was able to extract 88% and 47% of the vessel centerlines correctly using the vesselness/intensity and region statistics cost function respectively. For only the proximal part of the vessels these values were 97% and 86% respectively. Accuracy of centerline extraction, defined as the average distance from correctly automatically extracted parts of the centerline to the reference standard, was 0.64 mm for the vesselness/intensity and 0.51 mm for the region statistics cost function. The interobserver variability was 99% for the success rate measure and 0.42 mm for the accuracy measure. Qualitative evaluation using the best performing cost function resulted in successful centerline extraction for 233 out of the 252 coronary arteries (92%) in 63 additional CTCA images. The presented results, in combination with minimal user interaction and low computation time show that minimum cost path approaches can effectively be applied as a preprocessing step for subsequent analysis in clinical practice and biomedical research.



2.1 Introduction

Coronary artery disease (CAD) is currently one of the main causes of death in the world (World Health Organization, 2007). To date, conventional coronary angiography (CCA) is the gold standard method for the diagnosis of CAD. However, CCA is an invasive technique with a low, but not negligible, risk of procedure related complications and only provides information about the coronary lumen. Computed tomography coronary angiography (CTCA) is a non-invasive technique that allows both the evaluation of the coronary lumen and vessel wall (Cademartiri et al., 2007). It provides information regarding the presence, extent, and type (non-calcified or calcified) of coronary plaques. Such non-invasive, comprehensive plaque assessment may be relevant to improve risk stratification as compared to current approaches where only the severity of stenosis and the amount of calcium is measured (Leber et al., 2006).

Different visualization techniques for the evaluation of CTCA images are used in clinical practice, among which are multi-planar reformatting and curved planar reformatting (CPR), both depending on the centerline of the vessel of interest (Cademartiri et al., 2007). The manual definition of these centerlines is a laborious task and therefore reliable (semi-)automatic coronary artery centerline extraction is relevant in clinical practice. Furthermore, vessel centerlines can serve as a starting point for automatic quantitative vascular image analysis such as stenosis grading and measuring calcium volume.

Although much work has been done on vessel segmentation and centerline extraction, the centerline extraction of coronary arteries remains a challenging problem, owing to the small size of the vessels, reconstruction artifacts caused by irregular heartbeats of the patient and the presence of pathology.

For segmentation and centerline extraction of vessels from 3D medical image data region growing (Boskamp et al., 2004; Lavi et al., 2004; Eiho et al., 2004; Bartz and Lakare, 2005; Hennemuth et al., 2005; Metz et al., 2007) and tracking methods (Wink et al., 2000a; Aylward and Bullit, 2002; Wesarg and Firlle, 2004; Wong and Chunga, 2007) are quite popular. Some of them take, next to intensity information, directional (Aylward and Bullit, 2002; Wong and Chunga, 2007) or shape information (Boskamp et al., 2004; Lavi et al., 2004; Hennemuth et al., 2005) into account to guide or restrict the growing or tracking process. Next to seeding the algorithm, additional user interaction may be required in some of these methods to remove unwanted structures from the segmentation. Nain et al. (2004) and Yang et al. (2007) applied deformable models for segmentation of the coronary arteries.

A disadvantage of above methods is that they are likely to have problems in the presence of imaging artifacts such as irregular heart beat artifacts or severe pathology, e.g. calcifications or occlusions. In these areas local image information is not sufficient to extract the vessel of interest, and as a consequence these algorithms may terminate prematurely.

Other approaches were presented by Szymczak et al. (2006), who applied tree building to predetermined centerline candidate points and by Bülow et al. (2004), who combined region growing and tree building.

Minimum cost path approaches need at least the start and end point of the vessel, but are able to cross pathological regions and regions suffering from bad image quality (Wink

et al., 2000b, 2001, 2002; Olabarriaga et al., 2003; Wink et al., 2004; Li and Yezzi, 2007). Wink et al. (2002) demonstrated the application of minimum cost path approaches to coronary artery centerline extraction in 3D MRA data. Furthermore, they proposed a method in which scale is included as an additional dimension in the cost image (Wink et al., 2004). Olabarriaga et al. (2003) applied a minimum cost path technique for the extraction of coronary artery centerlines from CTCA data, but in their work the method was only evaluated on small vessel segments, using a limited number of images and with a reference standard based on annotations of only one observer. Deschamps and Cohen (2001) proposed to solve the minimum cost path problem by application of fast marching methods and Li and Yezzi (2007) extended this method to 4D, where the fourth dimension is related to the local radius of the vessel.

A method based on fuzzy connectedness was presented by Wang and Smedby (2007), which is comparable to minimum cost path approaches, but uses the weakest link to determine the costs of a certain path.

Finally, some authors presented probabilistic methods to extract vessel centerlines from medical image data (Florin et al., 2005; Schaap et al., 2007; Lesage et al., 2008; Friman et al., 2008a). Instead of choosing the best configuration after every iteration of the tracking process, the best vessel configuration is chosen retrospectively, thus taking into account multiple configurations during tracking. Next to be able to cross low quality or high pathological regions more easily, these methods can easily take into account geometric information or changing intensity distributions along the path. The major drawback of these methods is their computational complexity, which makes them currently less practical in a clinical setting.

The focus of this work is on finding as much of the coronary artery centerline within the vessel of interest as possible. To this end, centerlines are extracted using a minimum cost path approach. Two cost functions are evaluated. The first one is an extension of the cost function of Wink et al. (2002) and Olabarriaga et al. (2003). In their work only second order image information is used, but we add intensity information as a second feature. The second cost function evaluated is the one proposed by Li and Yezzi (2007), which is based on region statistics.

The contribution of this work is threefold. First, to minimize user-interaction and facilitate real-time centerline extraction, a method is proposed and evaluated to automatically find a starting point for the extraction algorithm in the center of the aorta. Saur et al. (2008) presented a method to find such a point based on a ray propagation approach. Their method was developed simultaneously with the method presented here. Second, the parameters for computation of the cost images are optimized using leave-one-image-out cross validation. Third, a thorough evaluation of the extraction results is performed quantitatively on 48 vessels in twelve images and qualitatively on another 252 vessels in 63 images. The reference standard used in the quantitative evaluation is derived from vessel centerlines manually annotated by two observers, which makes a comparison of the results with the interobserver variability possible.

Information about the data, the methods applied, parameter optimization and the conducted evaluation experiments can be found in Section 2.2. Results are reported in Section 2.3 and the discussion and conclusions are presented in the last section.

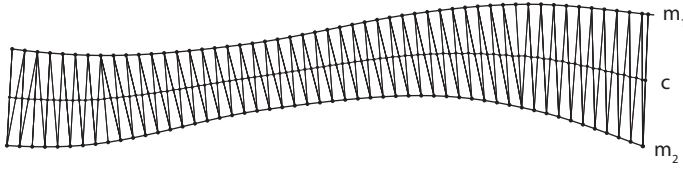


Figure 2.1: The reference standard centerline (c) is derived from centerlines manually annotated by two observers (m_1 and m_2) using a triangularization approach.

2.2 Materials and Methods

2.2.1 Imaging data and reference standard

CTCA images of 75 patients who were referred for CT coronary angiography at Erasmus MC, Rotterdam, The Netherlands, were selected. CTCA scans were acquired between December 2004 and January 2007 using a 64 slice (47 cases) and dual-source (28 cases) computed tomography scanner (Somatom Sensation 64 and Definition, Siemens Medical Solutions, Forchheim, Germany). Images were reconstructed using retrospective ECG gating with a B20f (1 case), B26f (8 cases), B30f (63 cases) or B46f (3 cases) kernel. Mean voxel size of the reconstructed images is $0.32 \times 0.32 \times 0.40 \text{ mm}^3$.

From the 62 images in which no severe breathing artifacts ($n = 6$) were present and which were not of patients who underwent coronary artery bypass surgery (CABG, $n = 7$), twelve images were randomly selected. In these images manual centerline delineation of the left anterior descending coronary artery (LAD), left circumflex artery (LCX), right coronary artery (RCA) and a randomly selected fourth coronary artery was performed by two observers. Next to the spatial locations of the centerline points the radius of the vessel at three or four points along the centerline was defined. The centerlines were annotated between the start and end point of the vessel, beforehand defined and approved by both observers. The start point was placed in the coronary ostium of the corresponding arterial tree and the end point was placed at the most distal point inside the vessel. The remaining 63 images (including the images with artifacts and the images of CABG patients) were used to perform an additional qualitative evaluation of the method.

The manually annotated centerlines of both observers were resampled equidistantly (0.1 mm) using a third degree polynomial for interpolation between consecutive annotated points. The radius at every point on the centerlines was linearly interpolated along the polynomial between the manually defined radii. Correspondence between points on both centerlines was determined using a triangularization of the area between the two centerlines and the average centerline was defined as the path through the mid-points of the triangle edges between the manually annotated centerlines (Figure 2.1). The radius for every point on the reference standard was defined as the average radius of the corresponding points on both centerlines.

Lengths of the resulting paths (mean \pm standard deviation) are $136 \text{ mm} \pm 29 \text{ mm}$ for the LAD, $116 \text{ mm} \pm 30 \text{ mm}$ for the LCX, $170 \text{ mm} \pm 40 \text{ mm}$ for the RCA and 93 mm

± 30 mm for the fourth vessel. The number of points annotated by the observers was on average 29 for the LAD, 26 for the LCX, 33 for the RCA and 23 for the fourth vessel.

To demonstrate the variability of image quality and the presence of calcium in the twelve images used for the quantitative evaluation, each image was visually assessed by a radiologist with three years experience in cardiac CT. Image quality was classified as good in five images, as adequate (presence of artifacts but evaluation possible with moderate confidence) in three images and as poor (presence of image-degrading artifacts and evaluation possible with low confidence) in four images. Presence of calcium was scored as absent in two images, modest (presence of calcified spots) in eight images and severe (presence of extensive calcifications) in two images.

2.2.2 Minimum cost path approach

Coronary artery centerlines are extracted using a minimum cost path approach. This has the advantage that given an appropriate cost function, the resulting path is guaranteed to be the globally optimal solution and that additional user interaction can be incorporated easily by subdividing the path into different sub paths. As the cumulative costs for a certain path depend on both the length of the path and the costs along the path, it is important that the costs are sufficiently large outside the vessel of interest and relatively low on the vessel centerline. Better adherence to these requirements enables more successful and accurate centerline detection. The centerlines are determined using Dijkstra's algorithm (Dijkstra, 1959) and subsequently smoothed using a Gaussian kernel ($\sigma=1$ mm).

Start point detection

Automatic start point detection decreases the amount of user-interaction needed and facilitates pre-computation of cumulative cost images. In a cumulative cost image, voxel values represent the minimum cumulative costs to travel from the starting point to the location of the voxel concerned. Once the end point is provided by the user, the final centerline is determined by following the path of steepest descent to the starting point of the vessel, which can be determined real-time. Only when centerline extraction fails and the user thus has to provide extra points along the centerline, additional computations are required as parts of the centerline need to be determined using a conventional minimum cost path search.

A point in the center of the aorta in the neighborhood of the coronary ostia is used as the start point for centerline extraction. Near this location, the descending aorta appears as a bright, round structure in the top left quarter of the axial slices of the CTCA image and its direction is orthogonal to the axial slices of the image. A slice based voxel classification method is proposed that incorporates this a priori information for finding an appropriate start point. Hereto, an image A is constructed which assigns to every voxel \mathbf{x} a measure which is related to the likeliness that it corresponds to the aorta center. This measure $A(\mathbf{x})$ is the product of three terms: $S(\mathbf{x})$ related to the size of the object, $L(\mathbf{x})$ related to the location of the object and $R(\mathbf{x})$ related to the shape (i.e. roundness) of the object (see Figure 2.3).



To determine $S(\mathbf{x})$, the input image is divided into two classes: contrast filled (foreground) regions, which are defined by a lower (I_{min}) and upperbound (I_{max}) on intensity, and other (background) structures. The shortest Euclidian distance to the background class $D(\mathbf{x})$ is calculated for every foreground voxel and $S(\mathbf{x})$ is subsequently modeled with the following Gaussian function:

$$S(\mathbf{x}) = \exp \left(-\frac{(D(\mathbf{x}) - \mu_s)^2}{2\sigma_s^2} \right) \quad (2.1)$$

with μ_s a parameter which should be set to a typical value of the aorta radius and σ_s a parameter which controls the range of radii taken into account.

The location term $L(\mathbf{x})$ is modeled as a Gaussian function on the clockwise rotation angle $\Theta(\mathbf{x})$ between the positive x-axis and the vector from the center of the heart $c(z)$ to the voxel concerned:

$$L(\mathbf{x}) = \exp \left(-\frac{(\Theta(\mathbf{x}) - \mu_l)^2}{2\sigma_l^2} \right) \quad (2.2)$$

with μ_l a parameter which should be set to a rotation angle corresponding to a typical location of the aorta and σ_l a parameter which controls the range of rotation angles taken into account. The center of the heart $c(z)$ in slice z is approximated by searching for the center of the biggest disc surrounded by the lungs. Resulting center points in the axial slices are smoothed in the z -direction using a Gaussian kernel with standard deviation σ_z to ensure continuity between adjacent slices.

The shape term $R(\mathbf{x})$ relates to the roundness of objects in the image, and is derived from the standard deviation of $D(\mathbf{y})$ for all voxels with $|\mathbf{x} - \mathbf{y}| = r$, with r smaller than or equal to the minimal expected aorta radius. When x is in the center of a round structure the distance values of the voxels lying on this circle are expected to be equal and the standard deviation of these values, defined as $\text{stdc}(\mathbf{x})$, is therefore expected to be low. The roundness term $R(\mathbf{x})$ is defined as follows:

$$R(\mathbf{x}) = 1 - \frac{1}{2} \left(\text{erf} (a_r (\text{stdc}(\mathbf{x}) - b_r)) + 1 \right) \quad (2.3)$$

with a_r and b_r parameters to control the steepness and location of the center of the error function (Figure 2.2).

High values of $A(\mathbf{x})$ should appear at approximately the same location in several consecutive slices. Therefore, these values are smoothed along the z -direction using a Gaussian kernel with standard deviation σ_b . To keep computation time low, voxel classification is performed on a downsampled version of the original image (max. 128^3 voxels). The extracted aorta point, used as the start point for the extraction algorithm, is the center of the voxel having the maximum value in $A(\mathbf{x})$.

Cost functions

Two different cost functions for the minimum cost path approach are considered: a vesselness/intensity cost function and a cost function based on region statistics.

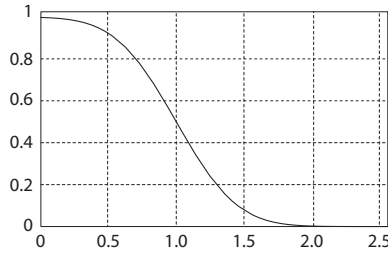


Figure 2.2: An example of the roundness term $R(x)$ of $A(x)$ with $a_r = 2.0$ and $b_r = 1.0$, as used in the experiments.

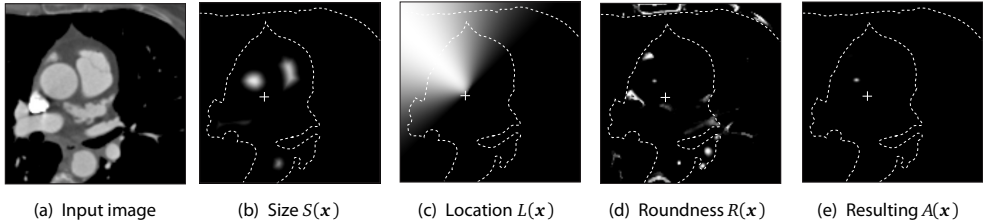


Figure 2.3: Example of $A(x)$ values in a slice of one of the CTCA images. For illustrational purposes, manually drawn outlines are overlaid. The cross corresponds to $c(z)$ for the current slice.

The **vesselness/intensity** cost function is defined as:

$$C(x) = \frac{1}{V(x)T(x) + \epsilon}, \quad (2.4)$$

with $V(x)$ the multi-scale vesselness measure proposed by Frangi et al. (1998), $T(x)$ an intensity measure and ϵ a small positive value to avoid singularity of the function when $V(x)T(x)$ approaches zero. The vesselness measure $V(x)$ is based on the eigenvalues λ_i of the Hessian matrix of the image computed at each voxel position x using Gaussian derivative operators. Frangi et al. use the theory developed by Lindeberg (1996) to normalize the Hessian matrix with σ^2 . It is not clear if this normalization will yield optimal centerline extraction results, because there is additional smoothing of the data intrinsically induced by the CT acquisition process and the response of the Gaussian derivatives can be distorted by neighboring structures. Moreover, even though the normalization would be optimal to give locally the best response, it still does not imply that this normalization is optimal for finding the globally best coronary centerline. We therefore compute the Hessian matrix using unnormalized Gaussian derivative operators and subsequently weigh the eigenvalues: $\lambda'_i = w_j \lambda_i$, with w_j the weighting factor for scale $j \in \{1, 2, \dots, J\}$ and J the number of scales applied. The intensity measure $T(x)$ is added to the cost function to ensure the bronchi will have high cost values and to improve the

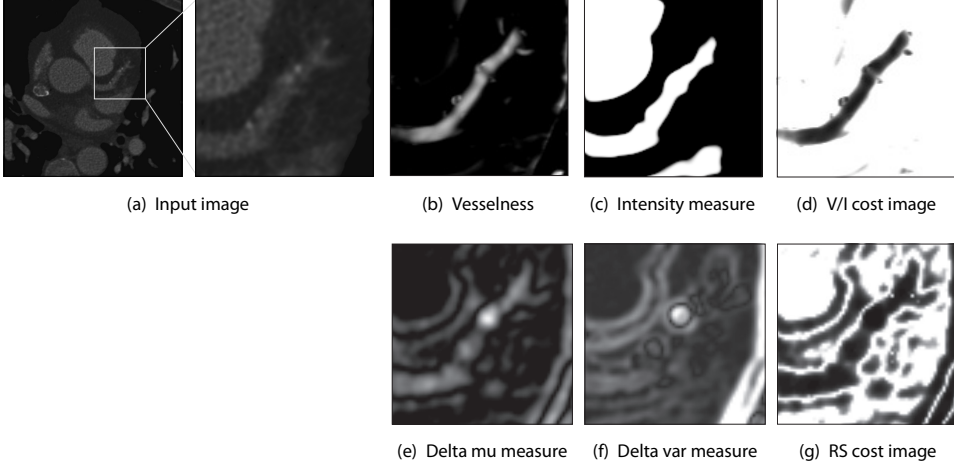


Figure 2.4: Example showing the different terms and the resulting cost image derived from these terms for both the vesselness/intensity (VI, top row) and the region statistics (RS, bottom row) cost function for a slice in one of the CTCA images.

contrast of the cost image. It is defined as a Sigmoid function:

$$T(\mathbf{x}) = \frac{1}{1 + \exp(-a_s(I(\mathbf{x}) - b_s))} \quad (2.5)$$

with $I(\mathbf{x})$ the intensity of the input image and a_s and b_s parameters to control the steepness and center of the transformation function respectively.

The **region statistics** cost function $P(\mathbf{x}, r)$ is defined as (Li and Yezzi, 2007)

$$P(\mathbf{x}, r) = \omega + \frac{l_1}{1 + \delta_{\mu(\mathbf{x}, r)}^2} + \frac{l_2}{1 + \delta_{\sigma^2(\mathbf{x}, r)}^2}, \quad (2.6)$$

with

$$\delta_{\mu} = |\mu(\mathbf{x}, r) - \mu(\mathbf{x}, r - 1)| \quad (2.7)$$

and

$$\delta_{\sigma^2}(\mathbf{x}, r) = |\sigma^2(\mathbf{x}, r) - \sigma^2(\mathbf{x}, r - 1)| \quad (2.8)$$

where $\mu(\mathbf{x}, r)$ and $\sigma^2(\mathbf{x}, r)$ are the average intensity and variance of intensity values on the surface of the sphere positioned at \mathbf{x} with radius r . The parameters l_1 and l_2 control the way in which both terms are weighted and ω is a non-negative constant.

Examples of the different terms and the resulting cost images derived from these terms for a slice in one of the images can be found in Figure 2.4.

Dimensionality reduction

To reduce memory and computational demands in the interactive part of the method, the 4D cumulative cost image resulting from the region statistics cost function is reduced to a 3D image. To this end we assume that for each 3D voxel the radius having minimal cumulative costs is the most plausible radius at that 3D position. Moreover, we assume that it is not possible that two vessels with different diameters are crossing the same voxel in the image. The dimensionality reduction of the cumulative cost image is subsequently achieved by taking for every voxel in the 3D image the minimum over all radii of the cumulative cost values.

2.2.3 Experiments

Start point detection

The start point for centerline extraction was determined in all 75 images using the algorithm described in Section 2.2.2. Parameter settings were determined experimentally using the twelve images for which a manually annotated reference standard was created. Settings for I_{min} , I_{max} , μ_s , μ_l were determined based on inspection of the intensity values of the contrast material, the variation in aorta sizes and the variation in aorta locations in the twelve images. All other parameters were empirically determined in order to obtain visually reasonable results for the twelve selected images. It was observed that the results are very robust against small changes in these parameter settings. The following settings were used: $I_{min} = 176HU$, $I_{max} = 776HU$, $\mu_s = 15.0mm$, $\sigma_s = 5.0mm$, $\mu_l = 1.25\pi$, $\sigma_l = 0.3\pi$, $\sigma_z = 0.8mm$, $a_r = 2.0$, $b_r = 1.0$, $r = 8.0mm$ and $\sigma_b = 0.8mm$.

Centerline extraction: quantitative evaluation

Parameter training and quantitative evaluation were performed using a leave-one-image-out cross validation on the twelve images (48 coronary arteries) for which a manual reference standard was available. In every step the method was trained on eleven images (44 vessels) and tested on one image (four vessels). The parameter settings used for the testing part of the cross validation were in every step determined on the training data in a two-step coarse-to-fine approach. Parameter ranges and sampling step sizes used are presented in Table 2.1. Parameter ϵ of Equation 2.4 was set to 10^{-4} for all experiments. For the vesselness filter used in the vesselness/intensity cost function, three (exponentially distributed) scales were chosen: 0.8 mm, 1.26 mm and 2.0 mm, corresponding to the size of the coronary arteries as reported by Dodge et al. (1992). Furthermore, in the training process, different combinations of values for the eigenvalue weighting factors w_j were used. These weighting factors were uniformly sampled on the surface of a unit sphere, because the result of the minimum cost path algorithm is not affected by multiplication of the cost function with a constant. Therefore, the ratios of the different weight combinations are important and not their absolute values. The corresponding x-, y- and z-coordinates of the sampled points determine the weighting factors for scale one, two and three respectively. This sphere sampling approach was also used to determine different combinations of parameter values for ω , l_1 and l_2 in Equation



Table 2.1: Ranges and step sizes used for parameter optimization in the leave-one-image-out cross validation experiments.

	Min	Max	Coarse steps	Fine steps
α	0.1	1.0	0.3	0.1
β	0.1	1.0	0.3	0.1
c	30	360	30	10
w_j	-	-	22 comb.	31 comb.
a_s	-224 HU	276 HU	100 HU	50 HU
b_s	5 HU	20 HU	5 HU	1 HU
ω, l_1, l_2	-	-	126 comb.	979 comb.

2.6. The minimum radius, maximum radius and radius step-size for the computation of Equation 2.7 and 2.8 was set to 1 mm, 7 mm and 0.5 mm respectively.

Centerline extraction was performed between the automatically found aorta point and the manually defined end point of the vessel. For the region statistics cost function, the start and end points were placed at all possible radius positions, eliminating the need to define the radius of the vessel at its start and end point.

Additionally, centerline extraction was quantitatively evaluated for only the clinically most relevant part of the vessels by extracting the first 7 cm of the vessels using the parameter settings following from the leave-one-image-out experiments on the complete vessels (Hong et al., 2005).

Centerline extraction: qualitative evaluation

To further demonstrate the robustness of the method, a qualitative evaluation was performed on the remaining 63 images using the cost function that performed best in the quantitative evaluation. Centerline extraction was performed between the automatically found aorta point and a manually defined end point, which was placed as distally as possible inside the vessel of interest. Parameters were set to the combination of values which were most frequently optimal in the quantitative evaluation (see Table 2.2). For all images the centerlines of four vessels (LAD, LCX, RCA and fourth) were extracted. Visual inspection of the resulting centerlines was performed and a second point was manually added when the path did not seem to follow the vessel of interest for more than 50%. In those cases where the native coronary artery was replaced by bypass surgery, the second point was placed at the start of the coronary artery bypass. Resulting new paths were again inspected and centerline extraction was marked as failed when the new path still did not follow more than 50% of the vessel of interest.

Evaluation measures

The part of the extracted centerlines from the aorta point to the ostium was disregarded in the evaluation, because the aorta is not included in the clinical evaluation of the coronary arteries.

Two evaluation measures were implemented: one to determine the success rate of the method and one to determine its accuracy. Both were determined using equidistantly resampled centerlines with a sampling distance of 0.1 mm. Correspondence between points on the automatically extracted centerline and the reference standard was determined using a triangularization approach. The set containing all points of the automatically extracted centerline and the set containing the points of the reference standard centerline are denoted with N_a and N_r respectively. Let $C_a \subseteq N_a$ be the set of points for which the distance to the corresponding point in N_r is smaller than or equal to the radius defined at that corresponding point and let $C_r \subseteq N_r$ be the set of points having correspondence with points in C_a . The success rate M_s of the method was defined as:

$$M_s = \frac{|C_a|}{|N_a|}, \quad (2.9)$$

with $|X|$ the cardinality of set X .

The accuracy M_a of the method was only determined for those parts of the centerline lying within the radius of the reference standard. The rationale behind this approach is that the magnitude of the distance to the reference centerline is no longer relevant when the tracking simply failed. Let T be the set of triangles resulting from the triangularization procedure for which the points from N_a are an element of C_a . The accuracy measure M_a was subsequently defined as:

$$M_a = \frac{\sum_{t \in T} \text{area}(t)}{d |C_r|}, \quad (2.10)$$

in which $\text{area}(t)$ stands for the area of triangle t and d is the sampling distance of the centerlines. Intuitively, M_a measures the average distance of the automatically extracted centerline to the reference standard in successfully extracted parts of the vessel and is therefore zero in cases of a perfect extraction, and larger otherwise. Success rate and accuracy is averaged over multiple vessels using measures $\overline{M_s}$ and $\overline{M_a}$ respectively:

$$\overline{M_s} = \frac{\sum_i |C_{a,i}|}{\sum_i |N_{a,i}|} \quad \overline{M_a} = \frac{\sum_i \sum_{t \in T_i} \text{area}(t)}{d \sum_i |C_{r,i}|} \quad (2.11)$$

Since the focus of this work is finding as much of the coronary artery centerlines within the vessel of interest as possible, optimization was performed using the success rate measure M_s .

Implementation

Computation of the cost images, parameter training and centerline extraction was implemented using C++ and ITK (Yoo et al., 2002a) and carried out using a grid of eight computing nodes running the Linux operating system and each equipped with two dual-core AMD Opteron 2216 2400 MHz processors and 16 GB memory. Aorta detection is implemented using C++ and MeVisLab (MeVisLab, Software for Medical Image Processing and Visualization) and carried out on a PC running the Windows XP operating

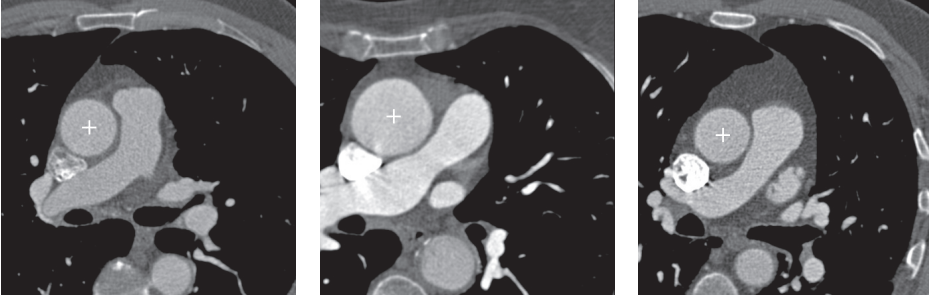


Figure 2.5: Examples of correctly found aorta points.

system and equipped with a Pentium 4 3.6 GHz processor and 4 GB memory. In the optimization part of the leave-one-image-out experiments for the region statistics cost function the images were downsampled with a factor two to keep computation time and memory usage manageable. We assume that the optimization results are not affected by this downsampling, as the intrinsic resolution of the CTCA data is approximately 1 mm (Rollano-Hijarrubia et al., 2006). The evaluation part of the leave-one-image-out experiments was performed on the full resolution data, to prevent potential degradation of the accuracy caused by downsampling, and to allow a fair comparison with the results of the vesselness/intensity cost function.

2.3 Results

2.3.1 Start point detection

The automatic detection of a start point in the aorta worked successfully in all 75 images. Examples of the results are shown in Figure 2.5.

2.3.2 Centerline extraction: quantitative evaluation

Illustrations of the optimization landscape for both cost functions can be found in Figure 2.6. This figure shows the success rate \overline{M}_s for varying α and β , or ω and l_1 while keeping the other parameters fixed at their optimal values. Training results can be found in Table 2.2 and 2.3, which list the most frequent optimal combination of parameter settings for the eleven training images. Centerline extraction results for the leave-one-image-out experiments can be found in Table 2.4 and 2.5. Results on only the proximal part of the vessels are presented in Table 2.6. A histogram showing the distribution of the success rate measure \overline{M}_s for both cost functions can be found in Figure 2.7.

It can be seen from Table 2.4 that the vesselness/intensity cost function results in a much larger success rate (88%) than the region statistics cost function (47%). The reason becomes clear when looking at Figure 2.7, where it can be seen that around half of the centerline extractions failed using the region statistics cost function. For the vesselness/intensity cost function, only three of the 48 extractions failed completely.

Table 2.2: Most frequent best combination of parameter settings for the leave-one-image-out experiments using the vesselness/intensity cost function.

α	β	c	w_1	w_2	w_3	a_s	b_s
0.5	0.4	230	0.99	0.10	0.10	4 HU	-59 HU

Table 2.3: Most frequent best combination of parameter settings for the leave-one-image-out experiments using the region statistics cost function.

ω	l_1	l_2
0	0.23	0.97

Table 2.4: Average overlap results ($\overline{M_s}$) in % for automatic centerline extraction compared to the interobserver variability.

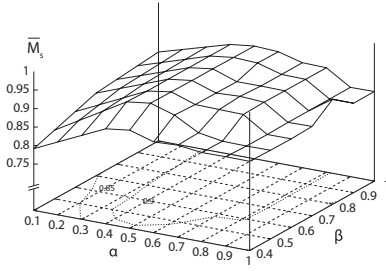
	LAD	LCX	RCA	4th	All
Vesselness/intensity	96	78	84	96	88
Region statistics	70	28	37	62	47
Interobserver	99	98	100	100	99

Table 2.5: Average accuracy results ($\overline{M_a}$) in mm for automatic centerline extraction compared to the interobserver variability.

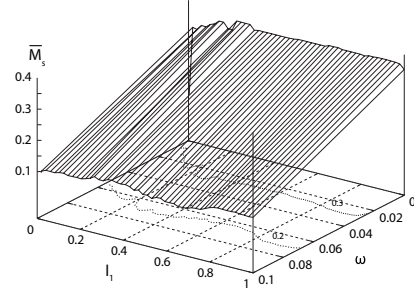
	LAD	LCX	RCA	4th	All
Vesselness/intensity	0.61	0.53	0.77	0.61	0.64
Region statistics	0.49	0.40	0.50	0.62	0.51
Interobserver	0.42	0.43	0.43	0.39	0.42

Table 2.6: Average overlap ($\overline{M_s}$) and accuracy results ($\overline{M_a}$) for automatic centerline extraction for the proximal part (first 7 cm) of the vessels.

	Overlap (%)	Accuracy (mm.)
Vesselness/intensity	97	0.79
Region statistics	86	0.50

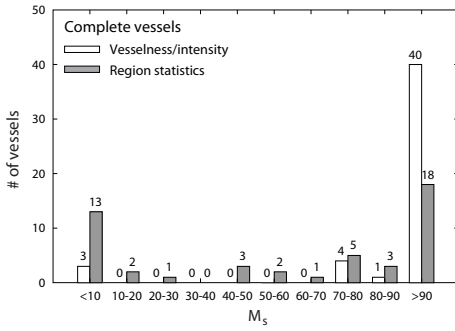


(a) Vesselness/intensity cost function: varying α and β while keeping the other parameters fixed at their optimal values.

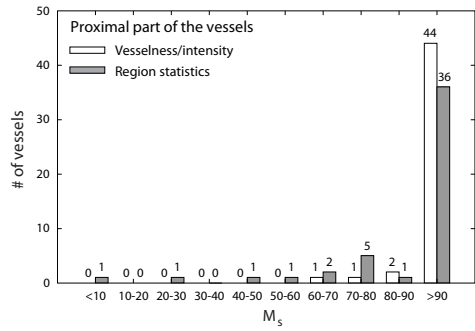


(b) Region statistics cost function: varying ω and l_1 . For this part of the optimization ω was set to 0.0 or 0.1 and l_1 and l_2 were sampled on a circle segment.

Figure 2.6: Illustrations of the optimization landscape for both the vesselness/intensity and region statistics cost function.



(a)



(b)

Figure 2.7: Histogram showing the distribution of success rate (\overline{M}_s) values for centerline extraction using both cost functions for (a) the complete coronary arteries and (b) only the proximal part of the vessels.

With respect to the accuracy, it can be noticed from Table 2.5 that the region statistics cost function performs better (0.51 mm) when compared to the vesselness intensity cost function (0.64 mm). By looking at the results for the proximal parts of the vessels in Table 2.6 it can be seen that the region statistics cost function is performing much better on these parts than on the complete coronary arteries. From Table 2.6 it is also apparent that especially in these parts of the vessels where the diameter is relatively large, the region statistics cost function performs better with respect to accuracy.

Examples of correctly extracted coronary artery centerlines using the vesselness/intensity cost function, the reference standard as created by the three observers and corresponding curved multi-planar reformatted images can be found in Figure 2.8. Examples of (partly) incorrectly extracted coronary artery centerlines for both cost functions can be found in Figure 2.9.

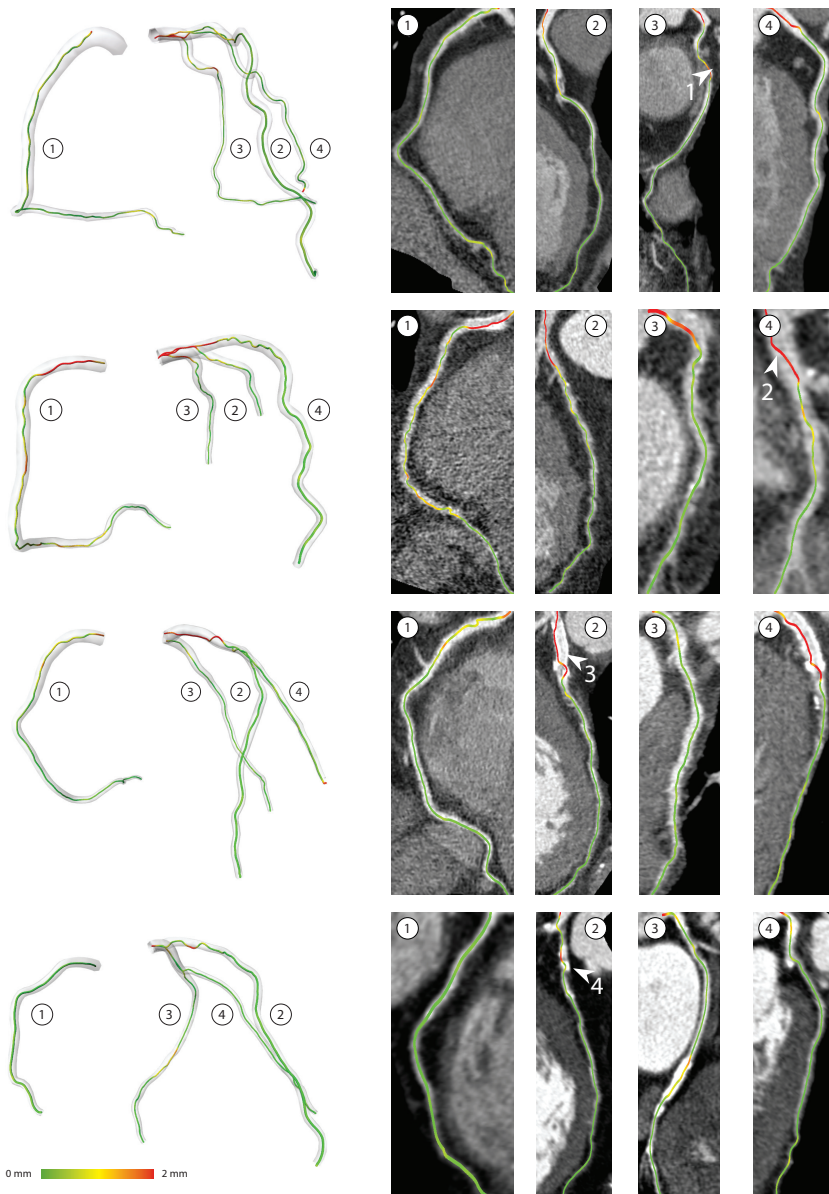


Figure 2.8: Examples of successfully extracted coronary artery centerlines using the vesselness/intensity cost function. The first column shows the reference standard (light gray tubes) and the automatically extracted centerlines. The other columns show the automatically extracted centerlines projected onto CPR images based on the reference standard centerline. The color coding of the extracted centerline indicates the distance from the automatically extracted centerline to the reference standard. Arrows in the CPR images indicate: 1) successfully crossed low contrast region caused by extreme pathology, 2) decreased extraction accuracy at location where the radius of the vessel is relatively large, and 3) and 4) centerline traversing a stent and a calcified region, due to false positive responses of the vesselness filter.



Figure 2.9: Some examples where centerline extraction was (partly) incorrect. Renderings are similar to those in Figure 2.8. The two leftmost images show results for the vesselness/intensity cost function. The other two images show results for the region statistics cost function.

Table 2.7: Number and percentage of successful and number of failed centerline extractions for the different categories in the qualitative evaluation.

	1 pt.	2 pt.	Failed	Total	Success
Breathing artifacts	16	19	5	24	79%
Bypasses	18	25	3	28	89%
Other cases	172	189	11	200	95%
Total	206	233	19	252	92%

2.3.3 Qualitative evaluation

Qualitative evaluation was performed using the vesselness/intensity cost function, which was the cost function yielding highest success rate values in the quantitative evaluation. Parameters were set to the values listed in Table 2.2. Centerlines were successfully extracted for 233 out of the 252 vessels (92%). For 206 vessels the user-defined end point was sufficient to extract the centerline successfully. For another 27 images, the method succeeded after providing a second point inside the vessel. For the remaining 19 vessels, centerline extraction failed. For the images with coronary artery bypasses, three one-click centerlines were marked as failed because the path followed the native coronary artery and not the bypass. After definition of the second point at the start of the bypass, all bypass centerlines were successfully extracted. An overview of the results can be found in Table 2.7. Overlap and accuracy for the 233 correctly extracted centerlines was visually comparable to the results of the quantitative evaluation.

2.3.4 Computation times

The running time of the proposed aorta detection method was on average 45 seconds. Pre-computation of the 3D vesselness/intensity cost image and the 4D region statistics cost image took on average 10 and 200 minutes respectively. Pre-computation of the cumulative cost image takes an additional computation time of 5 and 50 minutes respectively. All these steps can be done as a fully automated preprocessing step, after which centerlines can be presented real-time when the end point is provided by the user.

All computation times reported correspond to single-threaded implementations of the method. Moreover, computation times reported for the vesselness/intensity cost function are based on computation on the full resolution images, while computation times reported for the region statistics cost function are based on the downsampled versions of the volumes. Only our implementation for the region statistics cost function was optimized for speed. Parallelization of the cost image computation may further increase the computation time.

2.4 Discussion and Conclusions

The application of minimum cost path approaches for coronary centerline extraction from CT coronary angiography was evaluated. Two different cost functions were considered. The first cost function was based on a vesselness measure and intensity information, and the second cost function, based on region statistics, was recently proposed by Li and Yezzi (2007).

User interaction is limited to one mouse click per coronary artery. The start point for the extraction algorithm was determined using a method to automatically find a point in the center of the aorta in one of the axial slices. This method found a suitable start point in all 75 evaluated images.

Quantitative evaluation of centerline extraction using the minimum cost path approach and both cost functions was performed using leave-one-image-out cross validation in which also parameter optimization took place. For the vesselness/intensity cost function, this optimization procedure confirmed the settings proposed by Frangi et al. (1998) for the vesselness filter. Furthermore, it was found that the vesselness measure computed at the smallest scale ($\sigma = 0.8\text{mm}$) resulted in the highest success rate of the method, which was reflected in a large value for weighting factor w_1 . Further inspection of the extraction results revealed that using higher weighting factors for the larger scales resulted in incorrect extractions due to false positive responses of the vesselness filter, e.g. at the borders of the heart. For the region statistics cost function it turned out that setting ω to zero yielded highest success rate values for the complete coronary arteries.

The leave-one-image-out cross validation showed that 88% of the vessel centerlines was extracted correctly using one user-defined point and the vesselness/intensity cost function. For three cases centerline extraction failed, because the wrong vessel was followed. High cost values for a part of the vessel of interest and a substantial difference in vessel lengths caused the integrated costs along the path through the wrong vessel to be smaller than the integrated costs along the vessel centerline of interest. Retrospectively clicking one additional point in the vessel of interest would resolve this problem, but leads to additional computations, as the precomputed cumulative cost image can not be used for the extraction of the complete coronary centerline. Using the region statistics cost function the method was able to extract 47% of the centerlines correctly. As can be seen in Figure 2.4, the region statistics cost function results in a large number of low costs regions inside the heart, often resulting in paths with smaller cumulative costs through these regions. The interobserver variability for the success rate measure was 99%. Considering the proximal parts of the vessels only, the region statistics cost



function performed better with respect to the success rate measure (86%) compared to extraction of the complete coronary arteries.

It can be noticed that the vesselness/intensity cost function, which yields high success rate measures, is performing worse on the accuracy measure. On the other hand, the region statistics cost function results in a higher accuracy, but is less successful in extracting large coronary arteries. This difference can, for example, be noticed in Figure 2.9, where the correctly extracted centerlines by the region statistics cost function are better aligned with the center of the vessels than the centerlines extracted by the vesselness/intensity cost function. The accuracy difference between centerline extraction with the two cost functions was especially large in the parts of the vessel with relatively larger diameters. This is probably owing to the incorporation of the radius of the vessel in the 4th dimension of the cost image. For the vesselness/intensity measure, on the other hand, the influence of the large scales is minimized by the optimization procedure, and the path will therefore follow high vesselness responses of the small scales, which can make the path twist through the vessel or easily traverse tubular calcified plaques. The latter also causes a decrease in the success rate of the method. Other causes for small errors are jumps to nearby vessels or adjacent structures in the image having low cost values.

Qualitative evaluation on 63 images confirmed the robustness of the minimum cost path approach in combination with the vesselness/intensity cost function. For 233 out of the 252 vessels (92%) centerlines were extracted successfully. In the other nineteen cases the method failed, which was mainly caused by severe pathology such as chronic total occlusions and irregular heart beat artifacts. The proposed method performed slightly worse for coronary artery bypasses when compared to native coronary arteries (89% instead of 95%), which may be caused by the fact that often more pathology is present in these images. In images with severe breathing artifacts the method was still able to extract 79% of the vessel centerlines correctly.

There are a number of ways to potentially improve the success rate and accuracy of centerline extraction. With respect to the vesselness/intensity cost function, adding a gradient term may allow to differentiate true and false positives of the vesselness filter at larger scales, potentially improving the accuracy in the vessel sections with larger diameter. Additionally, increasing cost values in calcified regions utilizing calcium detection as preprocessing step, may improve the results as well. Recently proposed methods, for example based on oriented flux computations (Law and Chung, 2009) could potentially be used as well to address these problems. The success rate for the region statistics cost function may improve considerably by adapting the cost function to make the costs larger for large contrast filled regions, forcing the extracted centerlines to follow the surface of the heart instead of taking a Euclidian shorter path through the heart chambers. Combination of both cost functions can potentially fully exploit their advantages, yielding high success rates and accurate centerline extractions. Additionally, it is possible to improve the accuracy of the extracted centerlines by segmentation of the coronary lumen using the initial extracted centerline and a subsequent derivation of the central axis of this segmentation. Note that in this work Dijkstra's algorithm (Dijkstra, 1959) is used to solve the minimum cost path problem. Using fast marching methods as was used, for example, in the work of Li and Yezzi (2007) may potentially improve the accuracy of both methods

slightly and eliminate the need to smooth the paths after centerline extraction.

The method is evaluated on data from two different scanner types of the same vendor and acquired at the same institution. Although this is a limitation of the study, it is expected that similar performance can be achieved in unseen images of similar resolution as CT values are calibrated. Minor tuning of parameter settings may be required, e.g. as a consequence of different contrast injection protocols, scan parameter settings, and the use of different reconstruction kernels.

In this work, a distinction was made between interaction time and pre-computation time, the former considered more important in clinical practice than the latter. The conventional minimum cost path approach in which the path is computed after manual definition of the start and end point of the vessel by the user can take up to 30 seconds per vessel for a 3D cost function and three minutes for a 4D cost function, depending on the image quality and the amount of pathology present. The presented aorta detection method is easy to implement and facilitates pre-computation of all expensive parts of the extraction algorithm, making it possible to extract coronary artery centerlines real-time after user interaction. Furthermore, the presented dimensionality reduction method makes it possible to follow the same approach for 4D cost images. Although the time needed for pre-computation of the cumulative cost image is relatively large, in the majority of the clinical and research situations this does not cause a problem, because there is sufficient time between reconstruction of the CTCA data and evaluation of the data. Note that computation of the 4D region statistics cost function, which we optimized for speed, is computationally much more expensive than computation of the 3D vesselness/intensity cost function. Multi-threaded implementation of this software can on the other hand still speed up the cost image computation. With respect to the vesselness/intensity cost function, pre-computation of the cost image was performed using software that was not optimized for speed and it can therefore still be sped up considerably, e.g. by computation of the cost image on a region of interest or by using GPU accelerated software.

In conclusion, a minimum cost path approach using intensity and second order image information is very well able to extract coronary artery centerlines from CTCA data and can be a helpful tool in a wide range of research and clinical situations, especially when user-interaction and computation time are minimized using the methods presented in this work.

Acknowledgments

The authors would like to thank R. Manniesing for providing the Gaussian filtering and vesselness software used in this chapter.

3

Standardized Evaluation Methodology and Reference Database for Evaluating Coronary Artery Centerline Extraction Algorithms

This chapter is based on the manuscript: Standardized Evaluation Methodology and Reference Database for Evaluating Coronary Artery Centerline Extraction Algorithms, M. Schaap, **C.T. Metz**, T. van Walsum, A.G. van der Giessen, A.C. Weustink, N.R.A. Mollet, C. Bauer, H. Bogunović, C. Castro, X. Deng, E. Dikici, T. O'Donnell, M. Frenay, O. Friman, M. Hernández Hoyos, P.H. Kitslaar, K. Krissian, C. Kühnel, M.A. Luengo-Oroz, M. Orkisz, Ö. Smedby, M. Styner, A. Szymczak, H. Tek, C. Wang, S.K. Warfield, S. Zambal, Y. Zhang, G.P. Krestin and W.J. Niessen, *Medical Image Analysis*, 2009, vol. 13/5, pp 701–714.

Abstract

Efficiently obtaining a reliable coronary artery centerline from computed tomography angiography data is relevant in clinical practice. Whereas numerous methods have been presented for this purpose, up to now no standardized evaluation methodology has been published to reliably evaluate and compare the performance of the existing or newly developed coronary artery centerline extraction algorithms. This chapter describes a standardized evaluation methodology and reference database for the quantitative evaluation of coronary artery centerline extraction algorithms. The contribution of this work is fourfold: 1) a method is described to create a consensus centerline with multiple observers, 2) well-defined measures are presented for the evaluation of coronary artery centerline extraction algorithms, 3) a database containing thirty-two cardiac CTA datasets with corresponding reference standard is described and made available, and 4) thirteen coronary artery centerline extraction algorithms, implemented by different research groups, are quantitatively evaluated and compared. The presented evaluation framework is made available to the medical imaging community for benchmarking existing or newly developed coronary centerline extraction algorithms.



3.1 Introduction

Coronary artery disease (CAD) is currently the primary cause of death among American males and females (Rosamond et al., 2008) and one of the main causes of death in the world (World Health Organization, 2009). The gold standard for the assessment of CAD is conventional coronary angiography (CCA) (Cademartiri et al., 2007). However, because of its invasive nature, CCA has a low, but non-negligible, risk of procedure related complications (Zanzonico et al., 2006). Moreover, it only provides information on the coronary lumen.

Computed Tomography Angiography (CTA) is a potential alternative for CCA (Mowatt et al., 2008). CTA is a non-invasive technique that allows, next to the assessment of the coronary lumen, the evaluation of the presence, extent, and type (non-calcified or calcified) of coronary plaque (Leber et al., 2006). Such non-invasive, comprehensive plaque assessment may be relevant for improving risk stratification when combined with current risk measures: the severity of stenosis and the amount of calcium (Cademartiri et al., 2007). A disadvantage of CTA is that the current imaging protocols are associated with a higher radiation dose exposure than CCA (Einstein et al., 2007).

Several techniques to visualize CTA data are used in clinical practice for the diagnosis of CAD. Besides evaluating the axial slices, other visualization techniques such as maximum intensity projections (MIP), volume rendering techniques, multi-planar reformatting (MPR), and curved planar reformatting (CPR) are used to review CTA data (Cademartiri et al., 2007). CPR and MPR images of coronary arteries are based on the CTA image and a central lumen line (for convenience referred to as centerline) through the vessel of interest (Kanitsar et al., 2002). These reformatted images can also be used during procedure planning for, among other things, planning the type of intervention and size of stents (Hecht, 2008). Efficiently obtaining a reliable centerline is therefore relevant in clinical practice. Furthermore, centerlines can serve as a starting point for lumen segmentation, stenosis grading, and plaque quantification (Marquering et al., 2005; Wesarg et al., 2006; Khan et al., 2006).

This chapter introduces a framework for the evaluation of coronary artery centerline extraction methods. The framework encompasses a publicly available database of coronary CTA data with corresponding reference standard centerlines derived from manually annotated centerlines, a set of well-defined evaluation measures, and an on-line tool for the comparison of coronary CTA centerline extraction techniques. We demonstrate the potential of the proposed framework by comparing thirteen coronary artery centerline extraction methods, implemented by different authors as part of a segmentation challenge workshop at the Medical Image Computing and Computer-Assisted Intervention (MICCAI) conference (Metz et al., 2008b).

In the next two sections we will respectively describe our motivation of the study presented in this chapter and discuss previous work on the evaluation of coronary segmentation and centerline extraction techniques. The evaluation framework will then be outlined by discussing the data, reference standard, evaluation measures, evaluation categories, and web-based framework. The chapter will be concluded by presenting the comparative results of the thirteen centerline extraction techniques, a discussion of these results, and a conclusion about the work presented.

3.2 Motivation

The value of a standardized evaluation methodology and a publicly available image repository has been shown in a number of medical image analysis and general computer vision applications, for example in the Retrospective Image Registration Evaluation Project (West et al., 1997), the Digital Retinal Images for Vessel Extraction database (Staal et al., 2004), the Lung Image Database project (Armato et al., 2004), the Middlebury Stereo Vision evaluation (Scharstein and Szeliski, 2002), the Range Image Segmentation Comparison (Hoover et al., 1996), the Berkeley Segmentation Dataset and Benchmark (Martin et al., 2001), and a workshop and on-line evaluation framework for liver and caudate segmentation (van Ginneken et al., 2007).

Similarly, standardized evaluation and comparison of coronary artery centerline extraction algorithms has scientific and practical benefits. A benchmark of state-of-the-art techniques is a prerequisite for continued progress in this field: it shows which of the popular methods are successful and researchers can quickly apprehend where methods can be improved.

It is also advantageous for the comparison of new methods with the state-of-the-art. Without a publicly available evaluation framework, such comparisons are difficult to perform: the software or source code of existing techniques is often not available, articles may not give enough information for re-implementation, and if enough information is provided, re-implementation of multiple algorithms is a laborious task.

The understanding of algorithm performance that results from the standardized evaluation also has practical benefits. It may, for example, steer the clinical implementation and utilization, as a system architect can use objective measures to choose the best algorithm for a specific task.

Furthermore, the evaluation could show under which conditions a particular technique is likely to succeed or fail, it may therefore be used to improve the acquisition methodology to better match the post-processing techniques.

It is therefore our goal to design and implement a standardized methodology for the evaluation and comparison of coronary artery centerline extraction algorithms and publish a cardiac CTA image repository with associated reference standard. To this end, we will discuss the following tasks below:

- Collection of a representative set of cardiac CTA datasets, with a manually annotated reference standard, available for the entire medical imaging community;
- Development of an appropriate set of evaluation measures for the evaluation of coronary artery centerline extraction methods;
- Development of an accessible framework for easy comparison of different algorithms;
- Application of this framework to compare several coronary CTA centerline extraction techniques;
- Public dissemination of the results of the evaluation.



3.3 Previous work

Approximately thirty papers have appeared that present and/or evaluate (semi-)automatic techniques for the segmentation or centerline extraction of human coronary arteries in cardiac CTA datasets. The proposed algorithms have been evaluated by a wide variety of evaluation methodologies.

A large number of methods have been evaluated qualitatively (Bartz and Lakare, 2005; Bouraoui et al., 2008; Carrillo et al., 2007; Florin et al., 2004, 2006; Hennemuth et al., 2005; Lavi et al., 2004; Lorenz et al., 2003; Luengo-Oroz et al., 2007; Nain et al., 2004; Renard and Yang, 2008; Schaap et al., 2007; Szymczak et al., 2006; Wang and Smedby, 2007; Wesarg and Firle, 2004; Yang et al., 2005, 2006). In these articles detection, extraction, or segmentation correctness have been visually determined. An overview of these methods is given in Table 3.1. Other articles include a quantitative evaluation of the performance of the proposed methods (Bülow et al., 2004; Busch et al., 2007; Dewey et al., 2004; Larralde et al., 2003; Lesage et al., 2008; Li and Yezzi, 2007; Khan et al., 2006; Marquering et al., 2005; Metz et al., 2007; Olabarriaga et al., 2003; Wesarg et al., 2006; Yang et al., 2007). See Table 3.2 for an overview of these methods.

None of the abovementioned algorithms has been compared to another and only three methods were quantitatively evaluated on both the extraction ability (i.e. how much of the real centerline can be extracted by the method?) and the accuracy (i.e. how accurately can the method locate the centerline or wall of the vessel?). Moreover, only one method was evaluated using annotations from more than one observer (Metz et al., 2007).

Four methods were assessed on their ability to quantify clinically relevant measures, such as the degree of stenosis and the number of calcium spots in a vessel (Yang et al., 2005; Dewey et al., 2004; Khan et al., 2006; Wesarg et al., 2006). These clinically oriented evaluation approaches are very appropriate for assessing the performance of a method for a possible clinical application, but the performance of these methods for other applications, such as describing the geometry of coronary arteries (Lorenz and von Berg, 2006; Zhu et al., 2009), can not easily be judged.

Two of the articles (Dewey et al. (2004) and Busch et al. (2007)) evaluate a commercially available system (respectively Vitrea 2, Version 3.3, Vital Images and Syngo Circulation, Siemens). Several other commercial centerline extraction and stenosis grading packages have been introduced in the past years, but we are not aware of any scientific publication containing a clinical evaluation of these packages.

3.4 Evaluation framework

In this section we will describe our framework for the evaluation of coronary CTA centerline extraction techniques.

3.4.1 Cardiac CTA data

The CTA data was acquired in the Erasmus MC, University Medical Center Rotterdam, The Netherlands. Thirty-two datasets were randomly selected from a series of patients

Table 3.1: An overview of CTA coronary artery segmentation and centerline extraction algorithms that were qualitatively evaluated. The column 'Time' indicates if information is provided about the computational time of the algorithm.

Article	Pat. / obs.	Vessels	Evaluation details	Time
Bartz and Lakare (2005)	1/1	Complete tree	Extraction was judged to be satisfactory.	✓
Bouraoui et al. (2008)	40/1	Complete tree	Extraction was scored satisfactory or not.	
Carillo et al. (2007)	12/1	Complete tree	Extraction was scored with the number of extracted small branches.	✓
Florin et al. (2004)	1/1	Complete tree	Extraction was judged to be satisfactory.	✓
Florin et al. (2006)	34/1	6 vessels	Scored with the number of correct extractions.	
Hennemuth et al. (2005)	61/1	RCA, LAD	Scored with the number of extracted vessels and categorized on the dataset difficulty.	✓
Lavi et al. (2004)	34/1	3 vessels	Scored qualitatively with scores from 1 to 5 and categorized on the image quality.	✓
Lorenz et al. (2003)	3/1	Complete tree	Results were visually analyzed and criticized.	✓
Luengo-Oroz et al. (2007)	9/1	LAD & LCX	Scored with the number of correct vessel extractions. The results are categorized on the image quality and amount of disease.	✓
Nain et al. (2004)	2/1	Left tree	Results were visually analyzed and criticized.	
Renard and Yang (2008)	2/1	Left tree	Extraction was judged to be satisfactory.	
Schaap et al. (2007)	2/1	RCA	Extraction was judged to be satisfactory.	
Szymczak et al. (2006)	5/1	Complete tree	Results were visually analyzed and criticized.	✓
Wang and Smedby (2007)	33/1	Complete tree	Scored with the number of correct extractions.	✓
Wesarg and Firlie (2004)	12/1	Complete tree	Scored with the number of correct extractions.	✓
Yang et al. (2005)	2/1	Left tree	Extraction was judged to be satisfactory.	✓
Yang et al. (2006)	2/1	4 vessels	Scored satisfactory or not. Evaluated in ten ECG gated reconstructions per patient.	✓



Table 3.2: An overview of the quantitatively evaluated CTA coronary artery segmentation and centerline extraction algorithms. With ‘centerline’ and ‘reference’ we respectively denote the (semi-)automatically extracted centerline and the manually annotated centerline. The column ‘Pat./obs.’ shows the number of patient datasets used and the number of observer annotations used to derive the reference standard. The column ‘Time’ indicates if information is provided about the computational time of the algorithm. ‘Eval.’ indicates that the article evaluates an existing technique and that no new technique has been proposed.

Article	Pat. / obs.	Vessels	Used evaluation measures and details	Time	Eval.
Bülow et al. (2004)	9/1	3-5 vessels	Overlap: Percentage reference points having a centerline point within 2 mm.		
Busch et al. (2007)	23/2	Complete tree	Stenoses grading: Compared to human performance with CCA as ground truth.		✓
Dewey et al. (2004)	35/1	3 vessels	Length difference: Difference between reference length and centerline length. Stenoses grading: Compared to human performance with CCA as ground truth.	✓	✓
Khan et al. (2006)	50/1	3 vessels	Stenoses grading: Compared to human performance with CCA as ground truth.		✓
Larralde et al. (2003)	6/1	Complete tree	Stenoses grading and calcium detection: Compared to human performance.	✓	
Lesage et al. (2008)	19/1	3 vessels	Same as Metz et al. (2007)	✓	
Li and Yezzi (2007)	5/1	Complete tree	Segmentation: Voxel-wise similarity indices.		
Marquering et al. (2005)	1/1	LAD	Accuracy: Distance from centerline to reference standard.	✓	
Metz et al. (2007)	6/3	3 vessels	Overlap: Segments on the reference standard and centerline are marked as true positives, false positives or false negatives. This scoring was used to construct similarity indices. Accuracy: Average distance to the reference standard for true positive sections.		
Olabariaga et al. (2003)	5/1	3 vessels	Accuracy: Mean distance from the centerline to the reference.		
Wesarg et al. (2006)	10/1	3 vessels	Calcium detection: Performance compared to human performance.		✓
Yang et al. (2007)	2/1	3 vessels	Overlap: Percentage of the reference standard detected. Segmentation: Average distance to contours.		

Table 3.3: Image quality of the training and test datasets.

	Poor	Moderate	Good	Total
Training	2	3	3	8
Testing	4	8	12	24

who underwent a cardiac CTA examination between June 2005 and June 2006. Twenty datasets were acquired with a 64-slice CT scanner and twelve datasets with a dual-source CT scanner (Sensation 64 and Somatom Definition, Siemens Medical Solutions, Forchheim, Germany).

A tube voltage of 120 kV was used for both scanners. All datasets were acquired with ECG-pulsing (Weustink et al., 2008). The maximum current (625 mA for the dual-source scanner and 900 mA for the 64-slice scanner) was used in the window from 25% to 70% of the R-R-interval and outside this window the tube current was reduced to 20% of the maximum current.

Both scanners operated with a detector width of 0.6 mm. The image data was acquired with a table feed of 3.8 mm per rotation (64-slice datasets) or 3.8 mm to 10 mm, individually adapted to the patient's heart rate (dual-source datasets).

Diastolic reconstructions were used, with reconstruction intervals varying from 250 ms to 400 ms before the R-peak. Three datasets were reconstructed using a sharp (B46f) kernel, all others were reconstructed using a medium-to-smooth (B30f) kernel. The mean voxel size of the datasets is $0.32 \times 0.32 \times 0.4\text{mm}^3$.

Training and test datasets

To ensure representative training and test sets, the image quality of and presence of calcium in each dataset was visually assessed by a radiologist with three years experience in cardiac CT.

Image quality was scored as poor (defined as presence of image-degrading artifacts and evaluation only possible with low confidence), moderate (presence of artifacts but evaluation possible with moderate confidence) or good (absence of any image-degrading artifacts related to motion and noise). Presence of calcium was scored as absent, modest or severe. Based on these scorings the data was distributed equally over a group of 8 and a group of 24 datasets. The patient and scan parameters were assessed by the radiologist to be representative for clinical practice. Table 3.3 and 3.4 describe the distribution of respectively the image quality and calcium scores in the datasets.

The first group of 8 datasets can be used for training and the other 24 datasets are used for performance assessment of the algorithms. All the thirty-two cardiac CTA datasets and the corresponding reference standard centerlines for the training data are made publicly available.

**Table 3.4:** Presence of calcium in the training and test datasets.

	Low	Moderate	Severe	Total
Training	3	4	1	8
Testing	9	12	3	24

3.4.2 Reference standard

In this work we define the centerline of a coronary artery in a CTA scan as the curve that passes through the center of gravity of the lumen in each cross-section. We define the start point of a centerline as the center of the coronary ostium (i.e. the point where the coronary artery originates from the aorta), and the end point as the most distal point where the artery is still distinguishable from the background. The centerline is smoothly interpolated if the artery is partly indistinguishable from the background, e.g. in case of a total occlusion or imaging artifacts.

This definition was used by three trained observers to annotate centerlines in the selected cardiac CTA datasets. Four vessels were selected for annotation by one of the observers in all 32 datasets, yielding $32 \times 4 = 128$ selected vessels. The first three vessels were always the right coronary artery (RCA), left anterior descending artery (LAD), and left circumflex artery (LCX). The fourth vessel was selected from the large side branches of these main coronary arteries and the selection was as follows: first diagonal branch (14x), second diagonal branch (6x), optional diagonal coronary artery (6x), first obtuse marginal branch (2x), posterior descending artery (2x), and acute marginal artery (2x). This observer annotated for all the four selected vessels points close to the selected vessels. These points (denoted with 'point A') unambiguously define the vessels, i.e. the vessel of interest is the vessel closest to the point and no side-branches can be observed after this point.

After the annotation of these 128 points, the three observers used these points to independently annotate the centerlines of the same four vessels in the 32 datasets. The observers also specified the radius of the lumen at least every 5 mm, where the radius was chosen such that the enclosed area of the annotated circle matched the area of the lumen. The radius was specified after the complete central lumen line was annotated (see Figure 3.3).

The paths of the three observers were combined to one centerline per vessel using a mean shift algorithm for open curves: The centerlines are averaged while taking into account the possibly spatially varying accuracy of the observers by iteratively estimating the reference standard and the accuracy of the observers. Each point of the resulting reference standard is a weighted average of the neighboring observer centerline points, with weights corresponding to the locally estimated accuracy of the observers (van Walsum et al., 2008).

After creating this first weighted average, a consensus centerline was created with the following procedure: The observers compared their centerlines with the average centerline to detect and subsequently correct any possible annotation errors. This comparison was performed utilizing curved planar reformatted images displaying the annotated cen-

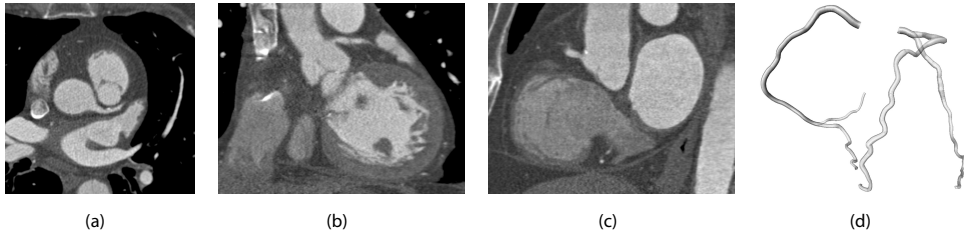


Figure 3.1: An example of the data with corresponding reference standard. (a) axial view of data (b) coronal view (c) sagittal view and (d) a 3D rendering of the reference standard.

terline color-coded with the distance to the reference standard and vice-versa. The three observers needed in total approximately 300 hours for the complete annotation and correction process.

After the correction step the centerlines were used to create the reference standard, using the same mean shift algorithm. Note that the uncorrected centerlines were used to calculate the inter-observer variability and agreement measures (see Section 3.4.5).

The points where for the first time the centerlines of two observers lie within the radius of the reference standard when traversing over this centerline from respectively the start to the end or vice versa were selected as the start- and end point of the reference standard. Because the observers used the abovementioned centerline definition it is assumed that the resulting start points of the reference standard centerlines lie within the coronary ostium.

The corrected centerlines contained on average 44 points and the average distance between two successive annotated points was 3.1 mm. The 128 resulting reference standard centerlines were on average 138 mm (std. dev. 41 mm, min. 34 mm, max. 249 mm) long.

The radius of the reference standard was based on the radii annotated by the observers and a point-to-point correspondence between the reference standard and the three annotated centerlines. The reference standard centerline and the corrected observer centerlines were first resampled equidistantly using a sampling distance of 0.03 mm. Dijkstra's graph searching algorithm was then used to associate each point on the reference standard with one or more points on each annotated centerline and vice versa. Using this correspondence, the radius at each point of the reference standard was determined by averaging the radius of all the connected points on the three annotated centerlines (see also Figure 3.2 and Figure 3.3). An example of annotated data with corresponding reference standard is shown in Figure 3.1. Details about the connectivity algorithm are given in Section 3.4.3.

3.4.3 Correspondence between centerlines

All the evaluation measures are based on a point-to-point correspondence between the reference standard and the evaluated centerline. This section explains the mechanism for determining this correspondence.

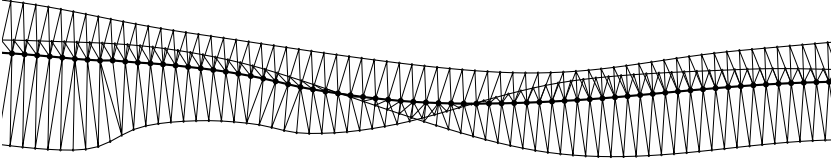


Figure 3.2: An illustrative example of the mean shift algorithm showing the annotations of the three observers as a thin black line, the resulting average as a thick black line, and the correspondences that are used during the last mean shift iteration in light-gray.

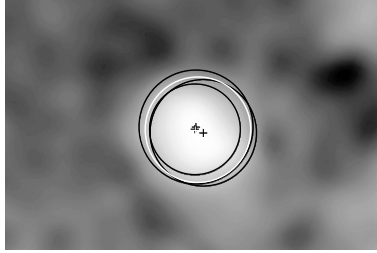


Figure 3.3: An example of the annotations of the three observers in black and the resulting reference standard in white. The crosses indicate the centers and the circles indicate the radii.

Before the correspondence is determined the centerlines are first sampled equidistantly using a sampling distance of 0.03 mm, enabling an accurate comparison. The evaluated centerline is then clipped with a disc that is positioned at the start of the reference standard centerline (i.e. in or very close to the coronary ostium). The centerlines are clipped because we define the start point of a coronary centerline at the coronary ostium and because for a variety of applications the centerline can start somewhere in the aorta. The radius of the disc is twice the annotated vessel radius and the disc normal is the tangential direction at the beginning of the reference standard centerline. Every point before the first intersection of a centerline and this disc is not taken into account during evaluation.

The correspondence is then determined by finding the minimum of the sum of the Euclidean lengths of all point-point connections that are connecting the two centerlines over all valid correspondences. A valid correspondence for centerline I, consisting of an ordered set of points p_i ($0 \leq i < n$, p_0 is the most proximal point of the centerline), and centerline II, consisting of an ordered set of points q_j ($0 \leq j < m$, q_0 is the most proximal point of the centerline), is defined as the ordered set of connections $C = \{c_0, \dots, c_{n+m-1}\}$, where c_k is a tuple $[p_a, q_b]$ that represents a connection from p_a to q_b , which satisfies the following conditions:

- The first connection c_0 connects the start points: $c_0 = [p_0, q_0]$.
- The last connection c_{n+m-1} connects the end points: $c_{n+m-1} = [p_{n-1}, q_{m-1}]$.

- If connection $c_k = [p_a, q_b]$ then connection c_{k+1} equals either $[p_{a+1}, q_b]$ or $[p_a, q_{b+1}]$.

These conditions guarantee that each point of centerline I is connected to at least one point of centerline II and vice versa.

Dijkstra's graph search algorithm is used on a matrix with connection lengths to determine the minimum Euclidean length correspondence. See Figure 3.2 for an example of a resulting correspondence.

3.4.4 Evaluation measures

Coronary artery centerline extraction may be used for different applications, and thus different evaluation measures may apply. We account for this by employing a number of evaluation measures. With these measures we discern between extraction capability and extraction accuracy. Accuracy can only be evaluated when extraction succeeded; in case of a tracking failure the magnitude of the distance to the reference centerline is no longer relevant and should not be included in the accuracy measure.

Definition of true positive, false positive and false negative points

All the evaluation measures are based on a labeling of points on the centerlines as true positive, false negative or false positive. This labeling, in its turn, is based on a correspondence between the points of the reference standard centerline and the points of the centerline to be evaluated. The correspondence is determined with the algorithm explained in Section 3.4.3.

A point of the reference standard is marked as true positive TPR_{ov} if the distance to at least one of the connected points on the evaluated centerline is less than the annotated radius and false negative FN_{ov} otherwise.

A point on the centerline to be evaluated is marked as true positive TPM_{ov} if there is at least one connected point on the reference standard at a distance less than the radius defined at that reference point, and it is marked as false positive FP_{ov} otherwise. With $\|\cdot\|$ we denote the cardinality of a set of points, e.g. $\|\text{TPR}_{\text{ov}}\|$ denotes the number of reference points marked true positive. See also Figure 3.4 for a schematic explanation of these terms and the terms mentioned in the next section.

Overlap measures

Three different overlap measures are used in our evaluation framework.

Overlap (OV) represents the ability to track the complete vessel annotated by the human observers and this measure is similar to the well-known Dice coefficient. It is defined as:

$$\text{OV} = \frac{\|\text{TPM}_{\text{ov}}\| + \|\text{TPR}_{\text{ov}}\|}{\|\text{TPM}_{\text{ov}}\| + \|\text{TPR}_{\text{ov}}\| + \|\text{FN}_{\text{ov}}\| + \|\text{FP}_{\text{ov}}\|}. \quad (3.1)$$

Overlap until first error (OF) determines how much of a coronary artery has been extracted before making an error. This measure can for example be of interest for image



guided intra-vascular interventions in which guide wires are advanced based on preoperatively extracted coronary geometry (Ramcharitar et al., 2009). The measure is defined as the ratio of the number of true positive points on the reference before the first error (TPR_{of}) and the total number of reference points ($TPR_{of} + FN_{of}$):

$$OF = \frac{\|TPR_{of}\|}{\|TPR_{of}\| + \|FN_{of}\|}. \quad (3.2)$$

The first error is defined as the first FN_{ov} point when traversing from the start of the reference standard to its end while ignoring false negative points in the first 5 mm of the reference standard. Errors in the first 5 mm are not taken into account because of the strictness of this measure and the fact that the beginning of a coronary artery centerline is sometimes difficult to define and for some applications not of critical importance. The threshold of five millimeters is equal to the average diameter annotated at the beginning of all the reference standard centerlines.

Overlap with the clinically relevant part of the vessel (OT) gives an indication of how well the method is able to track the section of the vessel that is assumed to be clinically relevant. Vessel segments with a diameter of 1.5 mm or larger, or vessel segments that are distally from segments with a diameter of 1.5 mm or larger are assumed to be clinically relevant (Leschka et al., 2005; Ropers et al., 2006). The point closest to the end of the reference standard with a radius larger than or equal to 0.75 mm is determined. Only points on the reference standard between this point and the start of the reference standard and points on the (semi-)automatic centerline connected to these reference points are used when defining the true positives (TPM_{ot} and TPR_{ot}), false negatives (FN_{ot}) and false positives (FP_{ot}). The OT measure is calculated as follows:

$$OT = \frac{\|TPM_{ot}\| + \|TPR_{ot}\|}{\|TPM_{ot}\| + \|TPR_{ot}\| + \|FN_{ot}\| + \|FP_{ot}\|}. \quad (3.3)$$

Accuracy measure

In order to discern between tracking ability and tracking accuracy we only evaluate the accuracy within sections where tracking succeeded.

Average inside (AI) is the average distance of all the connections between the reference standard and the automatic centerline given that the connections have a length smaller than the annotated radius at the connected reference point. The measure represents the accuracy of centerline extraction, provided that the evaluated centerline is inside the vessel.

3.4.5 Observer performance and scores

Each of the evaluation measures is related to the performance of the observers by a relative score. A score of 100 points implies that the result of the method is perfect, 50 points implies that the performance of the method is similar to the performance of

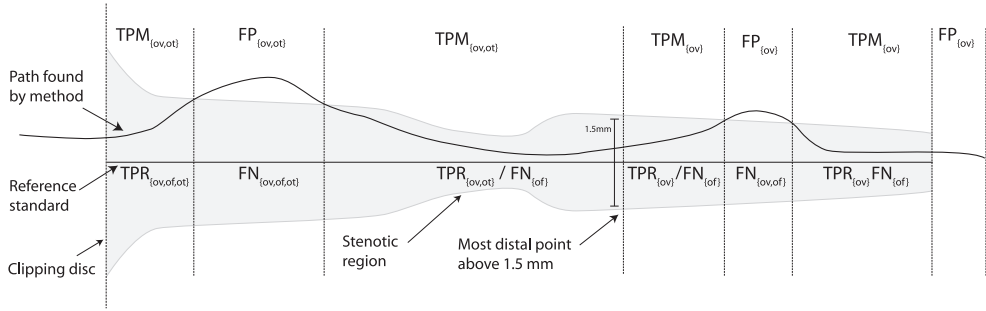


Figure 3.4: An illustration of the terms used in the evaluation measures (see Section 3.4.4). The reference standard with annotated radius is depicted in gray. The terms on top of the figure are assigned to points on the centerline found by the evaluated method. The terms below the reference standard line are assigned to points on the reference standard.

the observers, and 0 points implies a complete failure. This section explains how the observer performance is quantified for each of the four evaluation measures and how scores are created from the evaluation measures by relating the measures to the observer performance.

Overlap measures

The inter-observer agreement for the overlap measures is calculated by comparing the uncorrected paths with the reference standard. The three overlap measures (OV, OF, OT) were calculated for each uncorrected path and the true positives, false positives and false negatives for each observer were combined into inter-observer agreement measures per centerline as follows:

$$OV_{ag} = \frac{\sum (\|TPR_{ov}^i\| + \|TPM_{ov}^i\|)}{\sum (\|TPR_{ov}^i\| + \|TPM_{ov}^i\| + \|FP_{ov}^i\| + \|FN_{ov}^i\|)}$$

$$OF_{ag} = \frac{\sum \|TPR_{of}^i\|}{\sum (\|TPR_{of}^i\| + \|FN_{of}^i\|)}$$

$$OT_{ag} = \frac{\sum (\|TPR_{ot}^i\| + \|TPM_{ot}^i\|)}{\sum (\|TPR_{ot}^i\| + \|TPM_{ot}^i\| + \|FP_{ot}^i\| + \|FN_{ot}^i\|)},$$

where $i = \{0, 1, 2\}$ indicates the observer.

After calculating the inter-observer agreement measures, the performance of the method is scored. For methods that perform better than the observers the OV, OF, and OT measures are converted to scores by linearly interpolating between 100 and 50 points, respectively corresponding to an overlap of 1.0 and an overlap similar to the inter-observer agreement value. If the method performs worse than the inter-observer agreement the score is obtained by linearly interpolating between 50 and 0 points, with 0 points corre-

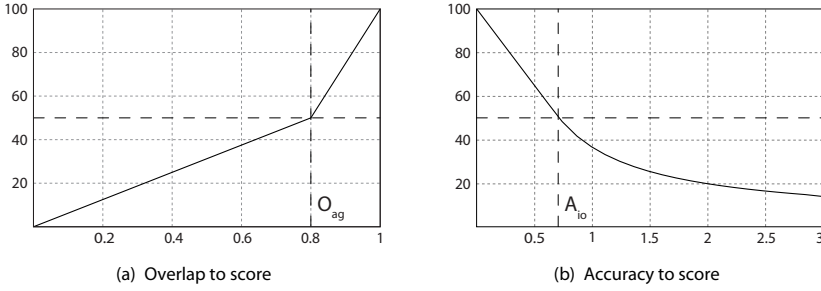


Figure 3.5: Illustration of how the measures are converted to scores for (a) an overlap measures and (b) the accuracy measure.

sponding to an overlap of 0.0:

$$\text{Score}_O = \begin{cases} (O_m/O_{ag}) * 50 & O_m \leq O_{ag} \\ 50 + 50 * \frac{O_m - O_{ag}}{1 - O_{ag}} & O_m > O_{ag}, \end{cases}$$

where O_m and O_{ag} define the OV, OF, or OT performance of respectively the method and the observer. An example of this conversion is shown in Figure 3.5(a).

Accuracy measure

The inter-observer variability for the accuracy measure AI is defined at every point of the reference standard as the expected error that an observer locally makes while annotating the centerline. It is determined at each point as the root mean squared distance between the uncorrected annotated centerline and the reference standard:

$$A_{io}(x) = \sqrt{1/n \sum (d(p(x), p_i))^2},$$

where $n = 3$ (three observers), and $d(p(x), p_i)$ is the average distance from point $p(x)$ on the reference standard to the connected points on the centerline annotated by observer i .

The extraction accuracy of the method is related per connection to the inter-observer variability. A connection is worth 100 points if the distance to the reference standard is 0 mm and it is worth 50 points if the distance is equal to the inter-observer variability at that point. Methods that perform worse than the inter-observer variability get a decreasing amount of points if the distance increases. They are rewarded per connection 50 points times the fraction of the inter-observer variability and the method accuracy:

$$\text{Score}_A(x) = \begin{cases} 100 - 50(A_m(x)/A_{io}(x)) & A_m(x) \leq A_{io}(x) \\ (A_{io}(x)/A_m(x)) * 50 & A_m(x) > A_{io}(x), \end{cases}$$

where $A_m(x)$ and $A_{io}(x)$ define the distance from the method centerline to the reference centerline and the inter-observer accuracy variability at point x . An example of this conversion is shown in Figure 3.5(b).

The average score over all connections that connect TPR and TPM points yields the AI observer performance score. Because the average accuracy score is a non-linear combination of all the distances, it can happen that a method has a lower average accuracy in millimeters and a higher score in points than another method, or vice versa.

Note that because the reference standard is constructed from the observer centerlines, the reference standard is slightly biased towards the observer centerlines, and thus a method that performs similar as an observer according to the scores probably performs slightly better. Although more sophisticated methods for calculating the observer performance and scores would have been possible, we decided because of simplicity and understandability for the approach explained above.

3.4.6 Ranking the algorithms

In order to rank the different coronary artery centerline extraction algorithms the evaluation measures have to be combined. We do this by ranking the resulting scores of all the methods for each measure and vessel. Each method receives for each vessel and measure a rank ranging from 1 (best) to the number of participating methods (worst). A user of the evaluation framework can manually mark a vessel as failed. In that case the method will be ranked last for the flagged vessel and the absolute measures and scores for this vessel will not be taken into account in any of the statistics.

The tracking capability of a method is defined as the average of all the $3(\text{overlap measures}) \times 96 (\text{vessels}) = 288$ related ranks. The average of all the 96 accuracy measure ranks defines the tracking accuracy of each method. The average overlap rank and the accuracy rank are averaged to obtain the overall quality of each of the methods and the method with the best (i.e. lowest) average rank is assumed to be the best.

3.5 Algorithm categories

We discern three different categories of coronary artery centerline extraction algorithms: automatic extraction methods, methods with minimal user interaction and interactive extraction methods.

3.5.1 Category 1: automatic extraction

Automatic extraction methods find the centerlines of coronary arteries without user interaction. In order to evaluate the performance of automatic coronary artery centerline extraction, two points per vessel are provided to extract the coronary artery of interest:

- Point A: a point inside the distal part of the vessel; this point unambiguously defines the vessel to be tracked;



- Point B: a point approximately 3 cm (measured along the centerline) distal of the start point of the centerline.

Point A should be used for selecting the appropriate centerline. If the automatic extraction result does not contain centerlines near point A, point B can be used. Point A and B are only meant for selecting the right centerline and it is not allowed to use them as input for the extraction algorithm.

3.5.2 Category 2: extraction with minimal user interaction

Extraction methods with minimal user interaction are allowed to use one point per vessel as input for the algorithm. This can be either one of the following points:

- Point A or B, as defined above;
- Point S: the start point of the centerline;
- Point E: the end point of the centerline;
- Point U: any manually defined point.

Points A, B, S and E are provided with the data. Furthermore, in case the method obtains a vessel tree from the initial point, point A or B may be used after the centerline determination to select the appropriate centerline.

3.5.3 Category 3: interactive extraction

All methods that require more user-interaction than one point per vessel as input are part of category 3. Methods can use e.g. both points S and E from category 2, a series of manually clicked positions, or one point and a user-defined threshold.

3.6 Web-based evaluation framework

The proposed framework for the evaluation of CTA coronary artery centerline extraction algorithms is made publicly available through a web-based interface at (<http://coronary.bigr.nl>). The thirty-two cardiac CTA datasets, and the corresponding reference standard centerlines for the training data, are available for download for anyone who wishes to validate their algorithm. Extracted centerlines can be submitted and the obtained results can be used in a publication. Furthermore, the website provides several tools to inspect the results and compare the algorithms.

3.7 MICCAI 2008 workshop

This study started with the workshop '3D Segmentation in the Clinic: A Grand Challenge II' at the 11th International Conference on Medical Image Computing and Computer Assisted Intervention (MICCAI) in September 2008 (Metz et al., 2008b). Approximately

100 authors of related publications, and the major medical imaging companies, were invited to submit their results on the 24 test datasets. Fifty-three groups showed their interest by registering for the challenge, 36 teams downloaded the training and test data, and 13 teams submitted results: five fully automatic methods, three minimally interactive methods, and five interactive methods. A brief description of the thirteen methods is given below.

During the workshop we used two additional measures: the average distance of all the connections (AD) and the average distance of all the connections to the clinical relevant part of the vessel (AT). In retrospect we found that these accuracy measures were too much biased towards methods with high overlap and therefore we do not use them anymore in the evaluation framework. This resulted in a slightly different ranking than the ranking published during the MICCAI workshop (Metz et al., 2008b). Please note that the two measures that were removed are still calculated for all the evaluated methods and they can be inspected using the web-based interface.

3.7.1 Fully automatic methods

- AutoCoronaryTree (Tek et al., 2008; Gulsun and Tek, 2008): The full centerline tree of the coronary arteries is extracted via a multi-scale medialness-based vessel tree extraction algorithm which starts a tracking process from the ostia locations until all coronary branches are reached.
- CocomoBeach (Kitslaar et al., 2008): This method starts by segmenting the ascending aorta and the heart. Candidate coronary regions are obtained using connected component analysis and the masking of large structures. Using these components a region growing scheme, starting in the aorta, segments the complete tree. Finally, centerlines within the pre-segmented tree are obtained using the WaveProp method (Marquering et al., 2005).
- DepthFirstModelFit (Zambal et al., 2008): Coronary centerline extraction is accomplished by fitting models of shape and appearance. A large-scale model of the complete heart in combination with symmetry features is used for detecting coronary artery seeds. To fully extract the coronary artery tree, two small-scale cylinder-like models are matched via depth-first search.
- GVFTube'n'Linkage (Bauer and Bischof, 2008b): This method uses a Gradient Vector Flow (Xu and Prince, 1998) based tube detection procedure for identification of vessels surrounded by arbitrary tissues (Bauer and Bischof, 2008c,a). Vessel centerlines are extracted using ridge-traversal and linked to form complete tree structures. For selection of coronary arteries gray value information and centerline length are used.
- VirtualContrast (Wang and Smedby, 2008): This method segments the coronary arteries based on the connectivity of the contrast agent in the vessel lumen, using a competing fuzzy connectedness tree algorithm (Wang and Smedby, 2007). Automatic rib cage removal and ascending aorta tracing are included to initialize



the segmentation. Centerline extraction is based on the skeletonization of the tree structure.

3.7.2 Semi automatic methods

- **AxialSymmetry** (Dikici et al., 2008): This method finds a minimum cost path connecting the aorta to a user supplied distal endpoint. Firstly, the aorta surface is extracted. Then, a two-stage Hough-like election scheme detects the high axial symmetry points in the image. Via these, a sparse graph is constructed. This graph is used to determine the optimal path connecting the user supplied seed point and the aorta.
- **CoronaryTreeMorphoRec** (Castro et al., 2008): This method generates the coronary tree iteratively from point S. Pre-processing steps are performed in order to segment the aorta, remove unwanted structures in the background and detect calcium. Centerline points are chosen in each iteration depending on the previous vessel direction and a local gray scale morphological 3D reconstruction.
- **KnowledgeBasedMinPath** (Krissian et al., 2008): For each voxel, the probability of belonging to a coronary vessel is estimated from a feature space and a vesselness measure is used to obtain a cost function. The vessel starting point is obtained automatically, while the end point is provided by the user. Finally, the centerline is obtained as the minimal cost path between both points.

3.7.3 Interactive methods

- **3DInteractiveTrack** (Zhang et al., 2008): This method calculates a local cost for each voxel based on eigenvalue analysis of the Hessian matrix. When a user selects a point, the method calculates the cost linking this point to all other voxels. If a user then moves to any voxel, the path with minimum overall cost is displayed. The user is able to inspect and modify the tracking to improve performance.
- **ElasticModel** (Hernández Hoyos et al., 2008). After manual selection of a background-intensity threshold and one point per vessel, centerline points are added by prediction and refinement. Prediction uses the local vessel orientation, estimated by eigen-analysis of the inertia matrix. Refinement uses centroid information and is restricted by continuity and smoothness constraints of the model (Hernández Hoyos et al., 2005).
- **MHT** (Friman et al., 2008b): Vessel branches are in this method found using a Multiple Hypothesis Tracking (MHT) framework. A feature of the MHT framework is that it can traverse difficult passages by evaluating several hypothetical paths. A minimal path algorithm based on Fast Marching is used to bridge gaps where the MHT terminates prematurely.
- **Tracer** (Szymczak, 2008): This method finds the set of core points (centers of intensity plateaus in 2D slices) that concentrate near vessel centerlines. A weighted

graph is formed by connecting nearby core points. Low weights are given to edges of the graph that are likely to follow a vessel. The output is the shortest path connecting point S and point E.

- **TwoPointMinCost** (Metz et al., 2008a): This method finds a minimum cost path between point S and point E using Dijkstra's algorithm. The cost to travel through a voxel is based on Gaussian error functions of the image intensity and a Hessian-based vesselness measure (Frangi et al., 1998), calculated on a single scale.

3.8 Results

The results of the thirteen methods are shown in Table 3.5, 3.6, and 3.7. Table 3.6 shows the results for the three overlap measures, Table 3.7 shows the accuracy measures, and Table 3.5 shows the final ranking, the approximate processing time, and amount of user-interaction that is required to extract the four vessels. In total 10 extractions ($< 1\%$) where marked as failed (see Section 3.4.6).

We believe that the final ranking in Table 3.5 gives a good indication of the relative performance of the different methods, but one should be careful to judge the methods on their final rank. A method ranked first does not have to be the method of choice for a specific application. For example, if a completely automatic approximate extraction of the arteries is needed one could choose GVFTube'n'Linkage (Bauer and Bischof, 2008b) because it has the highest overlap with the reference standard (best OV result). But if one wishes to have a more accurate automatic extraction of the proximal part of the coronary arteries the results point you toward DepthFirstModelFit (Zambal et al., 2008) because this method is highly ranked in the OF measure and is ranked first in the automatic methods category with the AI measure.

The results show that on average the interactive methods perform better on the overlap measures than the automatic methods (average rank of 6.30 vs. 7.09) and vice versa for the accuracy measures (8.00 vs. 6.25). The better overlap performance of the interactive methods can possibly be explained by the fact that the interactive methods use the start- and/or end point of the vessel. Moreover, in two cases (MHT (Friman et al., 2008b) and 3DInteractiveTrack (Zhang et al., 2008)) additional manually annotated points are used, which can help the method to bridge difficult regions.

When vessels are correctly extracted, the majority of the methods are accurate to within the image voxel size ($AI < 0.4\text{mm}$). The two methods that use a tubular shape model (MHT (Friman et al., 2008b) and DepthFirstModelFit (Zambal et al., 2008)) have the highest accuracy, followed by the multi-scale medialness-based AutoCoronaryTree (Tek et al., 2008; Gulsun and Tek, 2008) method and the CocomoBeach (Kitslaar et al., 2008) method.

Overall it can be observed that some of the methods are highly accurate and some have great extraction capability (i.e. high overlap). Combining a fully automatic method with high overlap (e.g. GVFTube'n'Linkage (Bauer and Bischof, 2008b)) and a, not necessarily fully automatic, method with high accuracy (e.g. MHT (Friman et al., 2008b)) may result in an fully automatic method with high overlap and high accuracy.



3.8.1 Results categorized

Separate rankings are made for each group of datasets with corresponding image quality and calcium rating to determine if the image quality or the amount of calcium has influence on the rankings.

Separate rankings are also made for each of the four vessel types. These rankings are presented in Table 3.8. It can be seen that some of the methods perform relatively worse when the image quality is poor or an extensive amount of calcium is present (e.g. CocomoBeach (Kitslaar et al., 2008) and DepthFirstModelFit (Zambal et al., 2008)) and vice versa (e.g. KnowledgeBasedMinPath (Krissian et al., 2008) and VirtualContrast (Wang and Smedby, 2008)).

Table 3.8 also shows that on average the automatic methods perform relatively worse for datasets with poor image quality (i.e. the ranks of the automatic methods in the P-column are on average higher compared to the ranks in the M- and G-column). This is also true for the extraction of the LCX centerlines. Both effects can possibly be explained by the fact that centerline extraction from poor image quality datasets and centerline extraction of the (on average relatively thinner) LCX is more difficult to automate.

3.8.2 Algorithm performance with respect to ostium distance

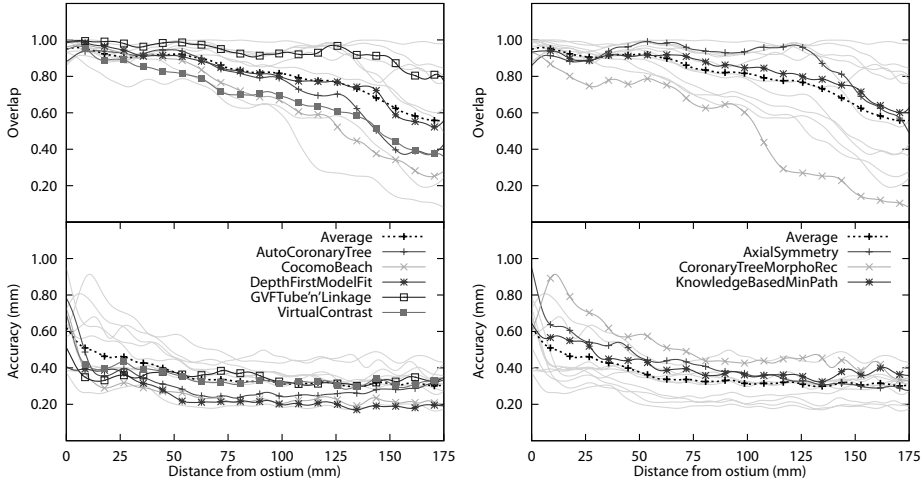
For a number of coronary artery centerline extraction applications it is not important to extract the whole coronary artery; only extraction up to a certain distance from the coronary ostium is required (see e.g. (Wang et al., 2004; Hong et al., 2005)).

In order to evaluate the performance of the methods with respect to the distance from the ostium, charts are generated that demonstrate the average performance over all 96 evaluated centerlines for each of the methods at a specific distance from the ostium (measured along the reference standard). Figure 3.6(a) shows these results for the automatic methods, Figure 3.6(b) shows the results for the methods with minimal user-interaction, and Figure 3.6(c) shows the results for the semi automatic methods.

The graphs show that all the evaluated methods are better able to extract the proximal part of the coronary arteries than the more distal part of the vessels. Moreover, they show that after approximately 5 cm the accuracy of almost all the methods is relatively constant. Furthermore, the graphs again demonstrate the fact that the automatic methods are on average more accurate than the semi automatic or interactive methods.

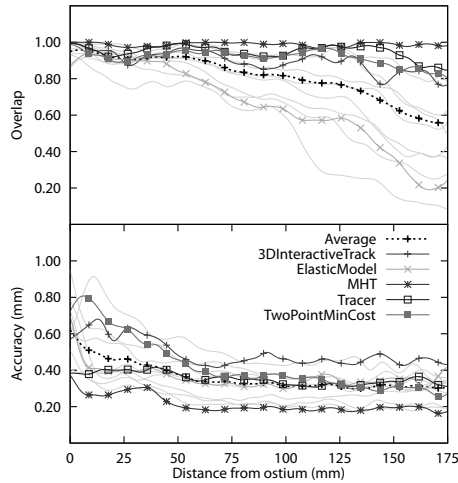
3.8.3 More statistics available online

Space limitations prevent us to incorporate more statistics here, but the on-line evaluation framework (<http://coronary.bigr.nl>) provides the possibilities to rank the methods based on different measures or scores, create statistics on a subset of the data and create overview tables for specific measures, categorized on image quality or score. It is for example possible to create Table 3.5, 3.6, and 3.7 for a specific subset of the data or to create Table 3.8 with a measure or score of choice, instead of the overall ranks. The website also contains the most recent version of the results. The on-line results



(a) Fully automatic centerline extraction methods.

(b) Semi automatic centerline extraction methods.



(c) Interactive centerline extraction methods.

Figure 3.6: The algorithm performance of each method with respect to the distance from the ostium averaged over all 96 evaluated vessels over the first 175mm. Overlap: the fraction of points on the reference standard marked as true positive. Accuracy: the average distance to the centerline if the point is marked true positive. Each of the three graphs shows in light-gray the results of all the thirteen evaluated methods and with the other lines the results of the respective algorithm category. The graphs also show in black (dotted) the average accuracy and overlap for all thirteen evaluated methods.



are different from the results reported in this chapter because of recent submissions and improvements in implementation of the different methods.

3.9 Discussion

A framework for the evaluation of CTA coronary artery centerline extraction techniques has been developed and made available through a web-based interface at: (<http://coronary.bigr.nl>). Currently thirty-two cardiac CTA datasets with corresponding reference standard centerlines are available for anyone how wants to benchmark a coronary artery centerline extraction algorithm.

Although the benefits of a large-scale quantitative evaluation and comparison of coronary artery centerline extraction algorithms are clear, no previous initiatives have been taken towards such an evaluation. This is probably because creating a reference standard for many datasets is a laborious task. Moreover, in order to get a good reference standard, annotations are needed from multiple observers and combining annotations from multiple observers is known to be difficult (Warfield et al., 2004) and until recently unexplored for three-dimensional curves (van Walsum et al., 2008). Furthermore, an appropriate set of evaluation measures has to be developed and a representative set of clinical datasets have to be made available. By addressing these issues we were able to present and use the proposed framework.

A limitation of the current study is the point-based vessel selection step for fully automatic methods. Because the coronary artery tree contains more vessels than the four annotated vessels this selection step had to be included, but it introduced the problem that fully automatic methods can extract many false-positives but still obtain a good ranking. This fact combined with the presented results of the fully automatic methods for the four evaluated vessels makes us believe that a future evaluation framework for coronary artery extraction methods should focus on the complete coronary tree. An obvious approach for such an evaluation would be to annotate the complete coronary artery tree in all the 32 datasets, but this is very labor intensive. An alternative approach would be to use the proposed framework for the quantitative evaluation of the four vessels and to qualitatively evaluate the complete tree. In this qualitative evaluation an observer should score if any vessels are falsely extracted and if all vessels of interest are extracted.

A further limitation of this study is that all the data have been acquired on two CT scanners of the same manufacturer in one medical center. We aim to extend the collection of datasets with datasets from different manufacturers and different medical centers. Further studies based on this framework could extend the framework with the evaluation of coronary lumen segmentation methods, coronary CTA calcium quantification methods or methods that quantify the degree of stenosis.

3.10 Conclusion

A publicly available standardized methodology for the evaluation and comparison of coronary centerline extraction algorithms is presented in this chapter. The potential of

Table 3.5: The overall ranking of the thirteen evaluated methods. The average overlap rank, accuracy rank and the average of these two are shown together with an indication of the computation time and the required user-interaction. The column ‘Cat.’ indicated the method category.

	Cat.	Avg. Ov. rank	Avg. Acc. rank	Avg. rank	Computation time	User- interaction
MHT (Friman et al., 2008b)	3	2.07	1.58	1.83	6 min.	2 to 5 pts.
Tracer (Szymczak, 2008)	3	4.21	2.52	3.37	30 min.	
DepthFirstModelFit (Zambal et al., 2008)	1	6.17	3.33	4.75	4-8 min.	
KnowledgebasedMinPath (Krissian et al., 2008)	2	4.31	8.36	6.34	7 hours	Pt. E
AutoCoronaryTree (Tek et al., 2008)	1	7.69	5.18	6.44	< 30 seconds	
GVFTube'n'Linkage (Bauer and Bischof, 2008b)	1	5.39	8.02	6.71	10 min.	70 seconds
CocomoBeach (Kislaar et al., 2008)	1	8.56	5.04	6.80	70 seconds	
TwoPointMinCost (Metz et al., 2008a)	3	5.30	8.80	7.05	12 min.	
VirtualContrast (Wang and Smedby, 2008)	1	8.71	7.74	8.23	5 min.	Point E
AxialSymmetry (Dikici et al., 2008)	2	6.95	9.60	8.28	5 min.	
ElasticModel (Hernández Hoyos et al., 2008)	3	9.05	8.29	8.67	2-6 min.	Global thresh. + 1 pt. per axis
3DInteractiveTrack (Zhang et al., 2008)	3	7.52	10.91	9.22	3-6 min.	
CoronaryTreeMorphoRec (Castro et al., 2008)	2	10.42	11.59	11.01	30 min.	Pt. S



Table 3.6: The resulting overlap measures for the thirteen evaluated methods. The average overlap, score and rank are shown for each of the three overlap measures. The column 'Cat.' indicated the method category.

	Cat	OV			OF			OT		
		%	score	rank	%	score	rank	%	score	rank
MHT (Friman et al., 2008b)	3	98.5	84.0	1.74	83.1	72.8	2.64	98.7	84.5	1.83
Tracer (Szymczak, 2008)	3	95.1	71.0	3.60	63.5	52.0	5.22	95.5	70.2	3.81
DepthFirstModelFit (Zambal et al., 2008)	1	84.7	48.6	7.29	65.3	49.2	5.32	87.0	60.1	5.90
KnowledgeBasedMinPath(Krissian et al., 2008)	2	88.0	67.4	4.46	74.2	61.1	4.27	88.5	70.0	4.21
AutoCoronaryTree (Tek et al., 2008)	1	84.7	46.5	8.13	59.5	36.1	7.26	86.2	50.3	7.69
GVFTube'n'Linkage (Bauer and Bischof, 2008b)	1	92.7	52.3	6.20	71.9	51.4	5.32	95.3	67.0	4.66
CocomoBeach (Kitslaar et al., 2008)	1	78.8	42.5	9.34	64.4	40.0	7.39	81.2	46.9	8.96
TwoPointMinCost (Metz et al., 2008a)	3	91.9	64.5	4.70	56.4	45.6	6.22	92.5	64.5	4.97
VirtualContrast (Wang and Smedby, 2008)	1	75.6	39.2	9.74	56.1	34.5	7.74	78.7	45.6	8.64
AxialSymmetry (Dikici et al., 2008)	2	90.8	56.8	6.17	48.9	35.6	7.96	91.7	55.9	6.71
ElasticModel (Hernández Hoyos et al., 2008)	3	77.0	40.5	9.60	52.1	31.5	8.46	79.0	45.3	9.09
3DInteractiveTrack (Zhang et al., 2008)	3	89.6	51.1	7.04	49.9	30.5	8.36	90.6	52.4	7.15
CoronaryTreeMorphoRec (Castro et al., 2008)	2	67.0	34.5	11.00	36.3	20.5	9.53	69.1	36.7	10.74

Table 3.7: The accuracy of the thirteen evaluated methods. The average distance, score and rank of each method are shown for the accuracy when inside (AI) measure. The column 'Cat.' indicated the method category.

	Cat.	AI		
		mm	score	rank
MHT (Friman et al., 2008b)	3	0.23	47.9	1.58
Tracer (Szymczak, 2008)	3	0.26	44.4	2.52
DepthFirstModelFit (Zambal et al., 2008)	1	0.28	41.9	3.33
KnowledgeBasedMinPath (Krissian et al., 2008)	2	0.39	29.2	8.36
AutoCoronaryTree (Tek et al., 2008)	1	0.34	35.3	5.18
GVFTube'n'Linkage (Bauer and Bischof, 2008b)	1	0.37	29.8	8.02
CocomoBeach (Kitslaar et al., 2008)	1	0.29	37.7	5.04
TwoPointMinCost (Metz et al., 2008a)	3	0.46	28.0	8.80
VirtualContrast (Wang and Smedby, 2008)	1	0.39	30.6	7.74
AxialSymmetry (Dikici et al., 2008)	2	0.46	26.4	9.60
ElasticModel (Hernández Hoyos et al., 2008)	3	0.40	29.3	8.29
3DInteractiveTrack (Zhang et al., 2008)	3	0.51	24.2	10.91
CoronaryTreeMorphoRec (Castro et al., 2008)	2	0.59	20.7	11.59

this framework has successfully been demonstrated by thoroughly comparing thirteen different coronary CTA centerline extraction techniques.

4

Nonrigid Registration of Dynamic Medical Imaging Data Using nD+t B-Splines and a Groupwise Optimization Approach

This chapter is based on the manuscript: Nonrigid Registration of Dynamic Medical Imaging Data Using nD+t B-Splines and a Groupwise Optimization Approach, **C.T. Metz**, S. Klein, M. Schaap, T. van Walsum, W.J. Niessen, *Medical Image Analysis*, 2011, vol. 15/2, pp 238–249.

Abstract

A registration method for motion estimation in dynamic medical imaging data is proposed. Registration is performed directly on the dynamic image, thus avoiding a bias towards a specifically chosen reference time point. Both spatial and temporal smoothness of the transformations are taken into account. Optionally, cyclic motion can be imposed, which can be useful for visualization (viewing the segmentation sequentially) or model building purposes. The method is based on a 3D (2D+time) or 4D (3D+time) free-form B-spline deformation model, a similarity metric that minimizes the intensity variances over time and constrained optimization using a stochastic gradient descent method with adaptive step size estimation. The method was quantitatively compared with existing registration techniques on synthetic data and 3D+t computed tomography data of the lungs. This showed subvoxel accuracy while delivering smooth transformations, and high consistency of the registration results. Furthermore, the accuracy of semi-automatic derivation of left ventricular volume curves from 3D+t computed tomography angiography data of the heart was evaluated. On average, the deviation from the curves derived from the manual annotations was approximately 3%. The potential of the method for other imaging modalities was shown on 2D+t ultrasound and 2D+t magnetic resonance images. The software is publicly available as an extension to the registration package `elastix`.



4.1 Introduction

4.1.1 Background

Dynamic imaging data are increasingly available due to ongoing advancements in medical imaging techniques (Li et al., 2008a). Motion estimation of the anatomy of interest from these images is often desirable, e.g. to quantify motion-related markers of disease, to construct motion and deformation models for therapeutic or surgical planning and guidance, or to remove motion to allow the analysis of intensity features at corresponding anatomical locations over time. Examples of motion quantification are the measurement of the distensibility of blood vessels or aneurysms (e.g. Li et al., 2008b; Ganten et al., 2008), the quantification of lung function (e.g. Reinhardt et al., 2008; Boldea et al., 2008) and the quantification of left ventricular function of the heart (e.g. Mahnken et al., 2009). The application of motion and deformation models in image-guided interventions was, for example, discussed by Hawkes et al. (2005). Motion removal has been applied, for example, in the analysis of perfusion CT or perfusion MRI images (e.g. Xue et al., 2008; Milles et al., 2008).

Manual motion estimation from a time series of images is a tedious task. Corresponding landmark positions in time need to be determined and depending on the application of interest the number of required landmarks may be very large. Image registration methods are often applied to automate this process. In these methods, the correspondence between the anatomy at different time points is found by minimizing a landmark based, segmentation based or intensity based similarity measure (Maintz and Viergever, 1998; Hill et al., 2001). These registration procedures must be sufficiently robust to handle the challenges inherent to dynamic imaging, such as fast moving anatomy, motion artifacts (Li et al., 2008a), and varying contrast to noise ratio over time, e.g. due to the application of dose reduction techniques such as ECG-derived pulsing windows in CT coronary angiography (Weustink et al., 2009).

4.1.2 Previous work on motion estimation

In this work we focus on intensity based registration approaches, which work directly on the input images without the need for preprocessing techniques to extract features from the images. There is a vast amount of work on the application of intensity-based image registration techniques for motion estimation. Next to these approaches, groupwise registration techniques have been proposed for the simultaneous alignment of multiple images from different patients (e.g. for atlas building), which is closely related to the alignment of different time point images without taking the temporal continuity of the data into account. We distinguish the existing techniques by the basic components of a registration approach: the transformation model, cost function and optimization strategy. Details about these categorizations are outlined below. An overview is given in Table 4.1. Besides these three categories, the table also reports the support for constraints on cyclic motion.

Several models can be used to describe the transformation that aligns the images. We discriminate between methods using an Eulerian approach, in which all deformations are

described with respect to the neighboring time point, and methods using a Lagrangian approach, in which deformations are described with respect to a chosen reference frame. In the latter approach the reference frame is often chosen to be directly related to one of the time points of the input image, but sometimes also defined implicitly, e.g. as the mean of the population. Most existing methods use a Lagrangian transformation model which can either take or not take into account the temporal smoothness of the deformations (respectively denoted with $nD+t$ and nD in Table 4.1; see also Figure 4.1 for an illustration). However, the majority of these methods only force the deformations to be smooth, viz. continuous and differentiable, in the spatial domain. Note that $nD+t$ transformation models have not only been applied in motion estimation methods presented in Table 4.1, but also in inter-patient and intra-patient alignment of dynamic imaging sequences (Perperidis et al., 2005; Lopez et al., 2008; Schreibmann et al., 2008; Peyrat et al., 2010).

The cost function, or dissimilarity metric, computes the dissimilarity between the images to measure the quality of the current transformation estimate. We distinguish three different approaches, often related to the chosen transformation model. The first is a consecutive approach in which the similarity is determined between the images of consecutive time points. The second is a reference approach in which the similarity is determined between the image to be registered and a chosen reference image. The last one is a global approach, in which the imaging data of all time points are taken into account in the computation of the cost function. A disadvantage of the first two approaches is that a limited amount of available image information is used during the registration procedure. The individual registrations only exploit the information present in the reference image and the image to be registered, whereas the other images may also contain valuable information. Moreover, by choosing a single reference time point, the registration result can be biased towards this image. In the global cost functions all image information is taken into account simultaneously, potentially leading to more robust and consistent registration results, without a bias towards a certain reference image.

Finally, we distinguish two kinds of optimization approaches for finding the optimal transformation. While the first approach optimizes the cost function for every time point separately, the second approach performs this optimization for all time points simultaneously, which we call a global approach. The optimization approach used is often related to the chosen cost function and transformation model. For global cost functions, a global optimization approach is needed. The same holds for the Lagrangian $nD+t$ transformation model that takes temporal smoothness into account. When a consecutive or reference cost function is applied, the optimization is most often performed in a pairwise manner.

In certain cases it is known a priori that the anatomical motion has a cyclic nature. When this knowledge is taken into account during the acquisition procedure, e.g. by ECG-gating or respiratory gating, one might want to incorporate this into the registration procedure. Two different approaches can be distinguished. In the first approach, a term is added to the cost function to penalize non cyclic transformations. In the other approach, cyclic motion is enforced by adapting the transformation model. To the best of our knowledge, only the first approach has been used in previous work.

Table 4.1: Existing dynamic and groupwise registration approaches. For every method, the transformation model, cost function, optimization strategy and inclusion of constraints on cyclic motion are listed. More than one check mark for a certain method in a certain category means that both approaches are applied in the same work. The different categories are explained in the introduction (Section 4.1.2). Methods are sorted on transformation model, cost function and optimization strategy subsequently. Cyclic motion can either be implemented in the cost function (c) or in the transformation model (t). The last three methods are used to compare the proposed method with (Section 4.3.1).

	Transformation model			Cost function			Optimization		
	Eul.	Lagr. (nD)	Lagr. (nD+t)	Consec.	Ref.	Global	Pairwise	Global	Cyclic
Boldea et al. (2008)	✓	✓		✓	✓		✓		
Reinhardt et al. (2008)	✓	✓		✓	✓		✓		
De Craene et al. (2009)	✓					✓		✓	
Bidaud and Vallée (2001)		✓			✓		✓		
Kaus et al. (2004)		✓			✓		✓		
Lorenzo-Valdés et al. (2002)		✓			✓		✓		
Marsland et al. (2003)		✓			✓		✓		
Marsland et al. (2008)		✓			✓		✓		
Rao et al. (2002)		✓			✓		✓		
Rietzel and Chen (2006)		✓			✓		✓		
Wierzbicki et al. (2004)		✓			✓		✓		
Joshi et al. (2004)		✓				✓	✓		
Balci et al. (2007a,b)		✓				✓		✓	
Bhatia et al. (2004)		✓				✓		✓	
Miller et al. (2000)		✓				✓		✓	
Zollei et al. (2005)		✓				✓		✓	
Sundar et al. (2009)			✓		✓			✓	✓(c)
Castillo et al. (2010)			✓		✓			✓	
Proposed method			✓			✓		✓	✓(t)
Reference time point		✓			✓		✓		
Consecutive time points	✓			✓			✓		
Groupwise method		✓				✓		✓	

4.1.3 Proposed method

In this work, we focus on the estimation of anatomical motion from dynamic medical imaging data. For this, we assume that physiologically motion is smooth (continuously differentiable) over time. Finding this smooth motion is, for example, useful for the construction of statistical motion models (Chapter 5, Metz et al., 2010) or motion visualization. The amount of smoothness depends on the expected motion of the anatomy of interest and the expected distortion of the motion due to pathology. Whereas the motion of the anatomy is expected to be smooth, the *appearance* of the moving anatomy in the reconstructed image may be non-smooth because of imaging artifacts. In our registration approach, we use a Lagrangian $nD+t$ transformation model parametrized by B-splines. The search space for the transformation that minimizes the dissimilarity metric is thereby reduced to those transformations that are both spatially and temporally smooth.

With respect to the cost function, we choose the global approach to eliminate a bias towards a chosen reference frame and use as much image information as possible. The use of a global cost function automatically leads to the choice for a global optimization routine.

A Lagrangian $nD+t$ transformation model, a global cost function, and a global optimization routine have previously been addressed in literature for motion estimation in 4D medical imaging data (see Table 4.1), but never jointly in one framework. We additionally propose a cyclic version of the B-spline transformation model and investigate its influence on the registration results.

The method is evaluated quantitatively on a 2D+t synthetic image, 3D+t computed tomography (CT) images of the lungs and 3D+t computed tomography angiography (CTA) images of the heart. Further examples are presented on 2D+t ultrasound (US) images of the carotid artery and 2D+t magnetic resonance (MR) images of the lungs.

To summarize, the main contributions of this work are:

- The development and evaluation of a registration method for motion estimation combining a Lagrangian $nD+t$ B-spline transformation model, a global cost function and global optimization strategy.
- The possibility to include a cyclic motion constraint that is strictly enforced by the transformation model.
- The quantitative comparison of the proposed technique with three well-known techniques.

Furthermore, the software developed for this publication is publicly available.

4.2 Method

The proposed method is based on a 3D (2D+time) or 4D (3D+time) free form B-spline deformation model, incorporating both the spatial and time dimensions. It aims to minimize the image intensity changes over time. An implicit reference frame is used to eliminate the need to choose a reference time point image. The following subsections describe the different components of the approach.



4.2.1 Transformation

A B-spline transformation model is used (Rueckert et al., 1999) because the compact support of B-splines keeps the running time reasonably low for higher dimensional imaging data. We restrict the deformations to only take place in the spatial domain and thereby search for those deformations that spatially align the different time point images. The deformation is regularized by assuming smoothness of the deformation in both the spatial and temporal direction of the data.

The D -dimensional input image is denoted with $I(\mathbf{y})$ where $\mathbf{y} = (\mathbf{x}^T, t)^T \in \mathbb{R}^s \times \mathbb{R}$ denotes a coordinate in I which consists of a spatial location $\mathbf{x} \in \mathbb{R}^s$ and temporal location $t \in \mathbb{R}$. $D = s + 1$ equals the dimension of the spatiotemporal image data.

The B-spline based coordinate transformation T_μ is defined as follows:

$$T_\mu(\mathbf{y}) = \mathbf{y} + \sum_{\mathbf{y}_k \in \mathcal{N}_y} \mathbf{p}_k \beta^r(\mathbf{y} - \mathbf{y}_k) \quad (4.1)$$

with \mathbf{y}_k the control points, $\beta^r(\mathbf{y})$ the r -th order multidimensional B-spline polynomial (Unser, 1999), \mathbf{p}_k the B-spline coefficient vectors, and \mathcal{N}_y the set of all control points within the compact support of the B-spline at \mathbf{y} . The control points \mathbf{y}_k are defined on a D -dimensional regular grid, overlaid on the image. The parameter vector μ consists of the collection of the first $D - 1$ elements of each \mathbf{p}_k . The last element of every \mathbf{p}_k is fixed to zero making sure that only deformations in the spatial domain are allowed. This is in contrast to the work of Perperidis et al. (2005) and Peyrat et al. (2010), where deformations in the temporal directions are allowed.

Optionally, cyclic motion can be enforced by letting the B-spline polynomials wrap around in the temporal direction (see Figure 4.1(a) and 4.1(b)). This is achieved by adapting the definition of the control point neighbourhood \mathcal{N}_y . A prerequisite for cyclic motion is that the number of time points of the image should be a multiple of the temporal B-spline control point spacing.

In the remainder of the chapter the notation $T_\mu(\mathbf{y})$ is interchanged with $T_\mu(\mathbf{x}, t)$ for convenience of notation.

4.2.2 Dissimilarity metric

Because we are working with monomodal dynamic imaging data, our method is based on the assumption that after correct registration the intensity values at corresponding spatial locations over time are equal. This can effectively be measured by computing the variance of intensity values at corresponding spatial locations over time (Bhatia et al., 2007). The dissimilarity metric, or cost function, is therefore defined as:

$$C(\mu) = \frac{1}{|S||\mathcal{T}|} \sum_{\mathbf{x} \in S} \sum_{t \in \mathcal{T}} (I(T_\mu(\mathbf{x}, t)) - \bar{I}_\mu(\mathbf{x}))^2 \quad (4.2)$$

with $\bar{I}_\mu(\mathbf{x})$ the average intensity value over time after applying transformation T_μ :

$$\bar{I}_\mu(\mathbf{x}) = \frac{1}{|\mathcal{T}|} \sum_{t \in \mathcal{T}} I(T_\mu(\mathbf{x}, t)) \quad (4.3)$$

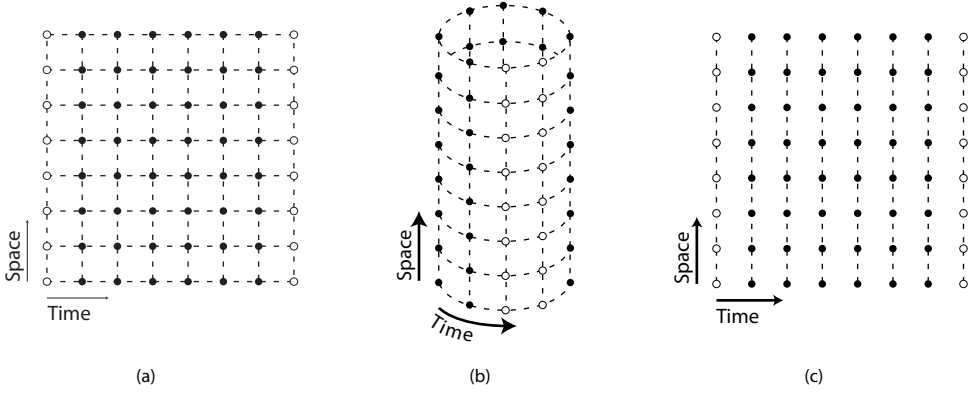


Figure 4.1: (a) nD+t B-spline grid, (b) cyclic nD+t B-spline grid and (c) nD B-spline grid used in reference time point, consecutive time point and groupwise registration approaches (see section 4.3.1). In the cyclic version (b), the grid points at the temporal border (open nodes) are direct neighbors.

and \mathcal{S} and \mathcal{T} the set of spatial and temporal voxel coordinates respectively.

4.2.3 Zero average displacement constraint

The registration is performed directly on the D -dimensional input image, and does not require a reference image. This results in an underconstrained optimization problem, because multiple solutions exist for the minimization of the dissimilarity metric (Equation 4.2). A translation of the image volume will, for example, not change the metric value. We therefore constrain the average deformation in time to be the identity transform, like Bhatia et al. (2004) and Balci et al. (2007a) did for groupwise registration:

$$\frac{1}{|\mathcal{T}|} \sum_{t \in \mathcal{T}} T_{\mu}(\mathbf{x}, t) = \mathbf{x}. \quad (4.4)$$

The next subsection explains how this constraint is enforced in the optimization procedure.

4.2.4 Optimization

For the final solution we need to determine those transform parameters that minimize the dissimilarity metric:

$$\hat{\mu} = \arg \min_{\mu} C(\mu) \text{ subject to (4.4)}. \quad (4.5)$$

Hereto, we use an adaptive stochastic gradient descent optimizer (ASGD) (Klein et al., 2009). The main advantage of this optimizer compared with conventional gradient-based optimizers is that it applies random sampling of the data in the computation of



the derivatives, which causes a significant reduction in computation time. This sampling strategy is applied to select the voxel locations in \mathcal{S} and the temporal indices in \mathcal{T} . Note that new samples are drawn at each iteration of the optimization.

The ASGD optimizer requires that the derivative of the cost function with respect to μ is known, which follows from differentiating Equation (4.2):

$$\frac{\partial C}{\partial \mu} = \frac{2}{|\mathcal{S}||\mathcal{T}|} \sum_{\mathbf{x} \in \mathcal{S}} \sum_{t \in \mathcal{T}} (I(T_\mu(\mathbf{x}, t)) - \bar{I}_\mu(\mathbf{x})) \cdot \left(\frac{\partial I(T_\mu(\mathbf{x}, t))}{\partial \mu} - \frac{\partial \bar{I}_\mu(\mathbf{x})}{\partial \mu} \right) \quad (4.6)$$

$$= \frac{2}{|\mathcal{S}||\mathcal{T}|} \sum_{\mathbf{x} \in \mathcal{S}} \left[\sum_{t \in \mathcal{T}} (I(T_\mu(\mathbf{x}, t)) - \bar{I}_\mu(\mathbf{x})) \frac{\partial I(T_\mu(\mathbf{x}, t))}{\partial \mu} - \frac{\partial \bar{I}_\mu(\mathbf{x})}{\partial \mu} \sum_{t \in \mathcal{T}} (I(T_\mu(\mathbf{x}, t)) - \bar{I}_\mu(\mathbf{x})) \right] \quad (4.7)$$

Substituting Equation 4.3 in the last term of 4.7 results in:

$$\frac{\partial C}{\partial \mu} = \frac{2}{|\mathcal{S}||\mathcal{T}|} \sum_{\mathbf{x} \in \mathcal{S}} \sum_{t \in \mathcal{T}} (I(T_\mu(\mathbf{x}, t)) - \bar{I}_\mu(\mathbf{x})) \frac{\partial I(T_\mu(\mathbf{x}, t))}{\partial \mu} \quad (4.8)$$

To apply the constraint that the average deformation over the time series is zero (see Section 4.2.3), we follow the approach of Balci et al. (2007a): we subtract the mean from each derivative vector, causing the sum of B-spline coefficients to be zero. We therefore use for every element i of $\partial C / \partial \mu$ the following equation to determine the constrained update:

$$\frac{\partial C'}{\partial \mu_i} = \frac{\partial C}{\partial \mu_i} - \frac{1}{|Q_i|} \sum_{q \in Q_i} \frac{\partial C}{\partial \mu_q} \quad (4.9)$$

where Q_i denotes the collection of all elements of μ over time that correspond to the same spatial grid point location and direction as element i .

4.2.5 Inverse transformation

The zero average displacement constraint described in Section 4.2.3 implicitly defines a reference frame that lies in the center of the dynamics described by the image. After registration all time point images are aligned in this reference frame. Depending on the type of application the registration procedure is used for, it might be useful to know transformation T_μ^{ij} which maps coordinates from time point i to time point j . To be able to define this transformation, the inverse mapping T_μ^{-1} , which maps coordinates from the input image coordinate frame to the reference frame, needs to be known.

Because the inverse of a B-spline transformation cannot be derived in closed-form, an additional subsequent optimization procedure is applied, formulated in a way similar to the registration procedure. The inverse transformation $T_{\hat{\mu}}^{-1}$ is derived by searching for a B-spline transformation $T_{\mathbf{v}}$ that cancels $T_{\hat{\mu}}$ by minimizing the following cost function:

$$F(\mathbf{v}) = \frac{1}{|Y|} \sum_{y \in Y} \|T_{\mathbf{v}}(T_{\hat{\mu}}(y)) - y\|^2. \quad (4.10)$$

with Y the set of voxel locations. The result $T_{\hat{\mathbf{v}}}$ of this minimization is used as an estimate of $T_{\hat{\mu}}^{-1}$. To make sure an accurate inverse can be estimated one should prevent foldings in the transformations resulting from the forward registration procedure. In this work we do this by choosing appropriate grid spacings, but one could also consider adding a penalty term which incorporates constraints on the Jacobian of the transformations (Chun et al., 2010; Sdika, 2008). As the inverse of a B-spline transformation cannot be modelled exactly with another B-spline transformation, we choose a smaller grid spacing for the inverse transform than was used for the forward transform that aligns all time point images to yield more accurate results.

The $(D-1)$ -dimensional transformation T^{ij} that aligns time point image i with time point image j can now be derived by combining the forward transform at time point j and the inverse transformation at time point i :

$$T_{\hat{\mu}}^{ij}(\mathbf{x}) = \left[T_{\hat{\mu}} \left(\left[T_{\hat{\mu}}^{-1}(\mathbf{x}, t_i) \right]_x, t_j \right) \right]_x \quad (4.11)$$

where $[\cdot]_x$ selects the $(D-1)$ -dimensional part of the D -dimensional transformation T .

4.2.6 Implementation details

Linear interpolation in the spatial domain is used for the derivation of intensity values at non grid-point positions in the images.

A multi-resolution strategy is employed to improve the capture range and robustness of the registration. In the lower resolutions the image is convolved with a Gaussian kernel. The standard deviation of this kernel and the spacing of the B-spline grid in the spatial directions of the image are reduced with a factor two in the next resolution level. This multi-resolution approach is used for both the registration procedure to align the time point images and the optimization procedure to find the inverse B-spline transformation.

The method has been implemented as an extension to the open source registration package `elastix` (Klein et al., 2010) and is freely available for download¹.

4.3 Experiments and results

Three types of experiments were conducted to evaluate the proposed method. First, we applied our approach to a synthetic image to compare the results with existing registra-

¹<http://elastix.isi.uu.nl>



tion approaches (Section 4.3.3). Second, the performance of the method was quantitatively evaluated using publicly available 3D+t CT data of the lungs (Section 4.3.4) and 3D+t CTA data of the heart (Section 4.3.5). And third, further examples are presented on a 2D+t ultrasound image of the carotid artery and a pediatric 2D+t MR image of the lungs (Section 4.3.6).

For the experiments on the synthetic image, the cardiac CTA data and the examples on ultrasound and MRI images, parameter settings were empirically determined. For the experiments on the CT data of the lungs, parameter settings were tuned on the publicly available POPI-model (Vandemeulebroucke et al., 2007). Resulting parameter settings and image dimensions are listed in Table 4.2. Parameter files are online available in the parameter file database of the *elastix* website¹.

4.3.1 Registration approaches

In the experiments described in Section 4.3.3 and Section 4.3.4, the proposed registration method is compared with existing registration approaches. The details of these approaches are outlined in the following paragraphs. The B-spline control point spacing, number of resolution levels, and number of iterations were chosen to be the same as the settings used for the proposed method to make a fair comparison possible.

Reference time point registration method

In the reference time point registration method the individual time point images are independently registered to the image of a chosen reference time point. The method uses a Lagrangian (nD) transformation model, a reference cost function and a pairwise optimization strategy. Furthermore, a mean squared difference metric was used, which is strongly related to the proposed variance metric.

Consecutive time point registration method

The consecutive time point registration method registers all individual time point images to the image of the neighbouring time point. It uses a Eulerian transformation model, a consecutive cost function and a pairwise optimization strategy. When the time point at which the registration is started is not equal to zero, registration is performed in two directions, to minimize the propagation of registration errors. A mean squares metric was used as the cost function.

Groupwise registration method

The groupwise registration approach simultaneously aligns the individual time point images. The method uses a Lagrangian (nD) transformation model, a global cost function and a global optimization strategy. The variance metric (Equation 4.2) is used as a cost function and the zero average displacement constraint (Equation 4.4) is applied. This approach is most similar to the proposed method, but does not impose smoothness of the deformations in the temporal direction of the image nor cyclic motion.

Table 4.2: Image dimensions, average voxel sizes and parameter settings used in the experiments. The voxel size in the temporal direction was always set to 1.0 ‘mm’. The spatial grid spacing for the inverse transformation in the synthetic experiments was chosen to be 1.0 mm smaller than the grid spacing for the forward transformation. The spatial grid spacing for the inverse transformation in the other experiments was the listed grid spacing minus 3.0 mm.

	Dimensions	Voxel size (mm)	Grid spacing (mm)	r	$ S $	$ T $	Iterations	Res.	Cyclic
Synthetic tube example	64×64×64	0.5×0.5	4×4×4	3	500	5	2000	2	(✓)
2D+t US carotids	512×512×60	0.06×0.06	1×1×3	3	1000	5	2000	3	
2D+t MR lungs	256×256×60	1.5×1.5	30×30×2	3	1000	5	2000	3	
3D+t CT heart	256×256×160×20	0.7×0.7×0.8	15×15×1	2	2000	5	2000	4	(✓)
3D+t CT lungs (POPI)	347×274×141×10	0.98×0.98×2.0	13×13×1/2/3	2	2000	5	2000	4	(✓)
3D+t CT lungs (DIR-lab)	256×256×100×10	1.1×1.1×2.5	13×13×1/2/3	2	2000	5	2000	4	(✓)



4.3.2 Evaluation measures

We used two evaluation measures for the synthetic experiment and the experiment on the lung data: the primary measure is the accuracy of the registration results and the secondary measure is the temporal smoothness of the transformations. Whereas smoothness on its own does not reflect the quality of the registration, the relation between registration accuracy and smoothness is relevant, as it can be useful when deciding on the right registration strategy for the application of interest. With equal, or slightly worse accuracy, a smoother result is often preferred.

The accuracy for transformation parameters μ was defined as the mean target registration error (mTRE) (van de Kraats et al., 2005) between a set of landmark collections $P = \{P_1, P_2, \dots, P_T\}$ for time points $\{1 \dots T\}$ and landmarks transformed from a reference time point r to all time points for which the landmarks are available:

$$\text{mTRE}(\mu) = \frac{1}{T|P_1|} \sum_{t \neq r} \sum_{p_{t,i} \in P_t} \left\| T_{\mu}^{rt}(p_{r,i}) - p_{t,i} \right\|, \quad (4.12)$$

with $p_{t,i}$ landmark i in time point t and r the reference time point.

The smoothness of transformation T_{μ} was measured as the irregularity of the landmark trajectories:

$$\text{mIrr}(\mu) = \frac{1}{T|P_1|} \sum_t \sum_{p_{t,i} \in P_t} \left\| \frac{\partial^2 T_{\mu}^{rt}(p_{r,i})}{\partial t^2} \right\|^2, \quad (4.13)$$

with $p_{t,i}$ landmark i at time point t and r the reference time point. Higher values mean more irregular/less smooth trajectories. We computed the derivatives using finite differences to be able to compute the irregularity for all considered registration procedures.

The standard deviation of TRE and irregularity values were also derived.

4.3.3 Quantitative evaluation on synthetic data

The 2D+t synthetic example consists of a $64 \times 64 \times 64$ pixel image containing a circle with a Gaussian profile with a standard deviation of 3 voxels. The circle follows a cosine shaped trajectory over time in the Y-direction of the image, i.e. the center of the circle over time is $(x_c, y_c + \alpha \cos(2\pi t/w))$, with $\alpha = 3$, $x_c = y_c = 15.5$ mm and $w = 32$ mm. The cosine is positioned in such a way that the deformation over time is cyclic. The contrast between the tube and the background is 1000 and Gaussian noise was added with a standard deviation of 150 resulting in a contrast-to-noise ratio of $\frac{20}{6}$. A cross section of the resulting 2D+t image is shown in Fig. 4.2. Seven registration procedures were tested. The first four are the consecutive and reference approach (Section 4.3.1) using both time 0 and 31 (halfway the time dimension of the data) as reference time point. The fifth is the groupwise registration method (Section 4.3.1). The last two approaches are the non-cyclic and cyclic version of the proposed registration method. After registration both the accuracy (Equation 4.12) and irregularity (Equation 4.13) of the transformations were determined.

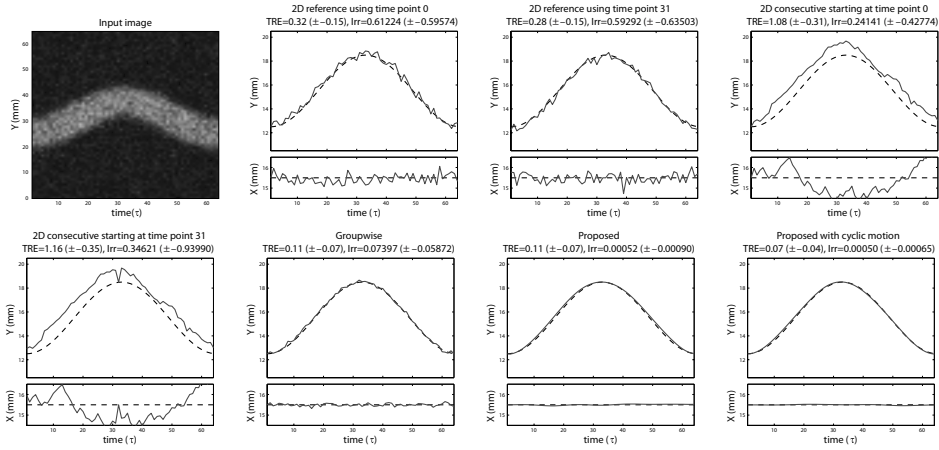


Figure 4.2: Registration results for the experiment on a synthetic image. A cross section of the input image is shown in the left top image. The other images show the trajectory resulting from the registration procedure as a solid line. The reference standard is plotted with a dashed line and the title of the plot lists the mean and standard deviation of the accuracy in mm and irregularity in mm/τ^2 of the registration results.

The X-displacements and Y-displacements found by the different registration procedures are plotted in Figure 4.2. The dashed line shows the reference curve. The titles of the plots show both the accuracy and irregularity. It can be noticed that the 2D reference method works reasonably well with respect to the accuracy, but the resulting trajectory is not smooth. The 2D consecutive method is distracted by the image noise and delivers inaccurate results. Among the non-temporally smooth methods the groupwise registration method performs best with respect to both accuracy and smoothness, which may be caused by the more robust global dissimilarity metric. The proposed temporally smooth method has the highest accuracy and delivers the most smooth trajectories of all methods. Accuracy is even slightly improved by imposing cyclic motion.

4.3.4 Quantitative evaluation on 3D+t CT data of the lungs

Four quantitative experiments were performed on clinical 3D+t CT data of the lungs. The first two experiments assess the accuracy, smoothness, and consistency of the registration results. In the third experiment, the influence of the spatial grid spacing used to obtain the inverse transformation was investigated. In the last experiment, the transitive consistency of the method is evaluated and compared with the reference registration method. The publicly available POPI-model (Vandemeulebroucke et al., 2007) and DIR-lab data were used (Castillo et al., 2009). Both consist of 3D+t CT scans of the lungs and corresponding landmarks in two or more time points of the image. For the DIR-lab data 300 landmarks in time point 0 (inspiration) and 5 (expiration) and 75 landmarks for each time point between time point 0 and 5 were available. For the POPI-model 37 landmarks for all ten time points were available. Parameter settings were tuned on the POPI image and subsequently used for all six images.



Accuracy

Registration accuracy was evaluated by computation of the TRE (Section 4.3.2) between the reference landmark positions and the landmark positions propagated from time point 0 (DIR-lab data) or time point 1 (POPI model) to all other time points. The reference time point for these propagations was chosen according to previously published work on this data. The results of the proposed method are compared with the reference time point, consecutive time point and groupwise registration methods described in Section 4.3.1. For the proposed method, registration was always performed on the complete 4D image and using a lung mask. For the POPI-model the provided mask was used. For the DIR-lab images the masks were created by thresholding, connected component analysis and morphological closing using a spherical structuring element with a diameter of 9 voxels. During the registration procedure the sample locations \mathbf{x} are drawn from a dilated version of these masks (kernel radius of 13 voxels). Moreover, $T_\mu(\mathbf{y})$ should lie within the non-dilated mask to be taken into account for the computation of the variance metric. Registration was performed for grid point spacings of one, two and three time points in the time-dimension and with and without applying the cyclic motion constraint to quantify the effect of the temporal and cyclic smoothness on the results.

Results for the 300 two-time-point landmarks of the DIR-lab data are presented in Table 4.3. Results for the 75 landmarks in six time points of the DIR-lab data and for the 37 landmarks in ten time points of the POPI-model are listed in Table 4.4. For comparison, the initial TRE and the best published results on the POPI-model (Kabus et al., 2009) using 3D B-spline registration and on the DIR-lab data (Castillo et al., 2010) using a four-dimensional optical flow method based on trajectory modeling are included in the tables. Both tables show that the proposed method can achieve subvoxel accuracy, yielding TRE values that are similar to the best published results on the same data. The results for the proposed method without the use of the cyclic motion constraint show that temporal smooth deformations can be achieved by compromising only slightly on registration accuracy. Enabling the cyclic motion constraint helps for DIR-lab case 1, but decreases the accuracy for the other cases.

The average running time on the DIR-lab data is around 40 minutes for the 3D reference, consecutive and groupwise registration approaches and around 1 hour, 1 hour and 15 minutes, and 1 hour and 30 minutes for the proposed method while using a temporal spacing of 3, 2 and 1 time points respectively (AMD Opteron[®] 2216 2400 MHz). The increase in computation time while using smaller temporal grid spacings is mainly due to the larger size of μ . A visualization of the imaging data before and after registration is shown in Figure 4.3.

Smoothness

The registration results of Section 4.3.4 were subsequently used to determine the smoothness of the landmark trajectories by computing their irregularity (Equation 4.13). The results are shown in a bar chart in Figure 4.4. Every bar represents one of the registration approaches and every group of bars represents a certain test image. The proposed method results in the most smooth trajectories. It can be seen that increasing the tem-

Table 4.3: Average and standard deviation of target registration errors in mm for the 300 landmarks in two time points of the DIR-lab images using the proposed method with three different temporal control point spacings and with and without the cyclic motion constraint. Results are compared with the reference time point, consecutive time point, and groupwise registration approaches. The best previously published results are listed in the last row of the table.

	DIR-lab				
	Case 1	Case 2	Case 3	Case 4	Case 5
Initial	3.89 (2.78)	4.34 (3.90)	6.94 (4.05)	9.83 (4.85)	7.48 (5.50)
Temp. spacing of 3 time points (non-cyclic)	1.09 (0.53)	1.12 (0.61)	1.29 (0.70)	1.86 (1.34)	2.06 (1.97)
Temp. spacing of 2 time points (non-cyclic)	1.05 (0.50)	1.09 (0.60)	1.28 (0.82)	1.73 (1.34)	1.82 (1.56)
Temp. spacing of 1 time point (non-cyclic)	1.02 (0.47)	1.06 (0.55)	1.21 (0.68)	1.57 (1.20)	1.70 (1.48)
Temp. spacing of 3 time points (cyclic)	1.05 (0.49)	1.30 (0.83)	1.57 (1.01)	2.52 (2.23)	2.49 (2.22)
Temp. spacing of 2 time points (cyclic)	1.04 (0.48)	1.16 (0.70)	1.35 (0.77)	1.86 (1.44)	2.12 (1.85)
Temp. spacing of 1 time point (cyclic)	1.02 (0.50)	1.06 (0.56)	1.19 (0.66)	1.57 (1.20)	1.73 (1.49)
Group-wise	1.02 (0.49)	1.07 (0.56)	1.22 (0.68)	1.56 (1.19)	1.74 (1.47)
3D reference time point	0.99 (0.48)	0.96 (0.49)	1.11 (0.62)	1.49 (1.08)	1.37 (1.21)
3D consecutive time points	1.15 (0.60)	1.06 (0.62)	1.27 (0.68)	1.55 (1.17)	1.82 (1.59)
Castillo et al. (2010)	0.97 (1.02)	0.86 (1.08)	1.01 (1.17)	1.40 (1.57)	1.67 (1.79)



Table 4.4: Average and standard deviation of target registration errors in mm for the 75 landmarks in six time points of the DIR-lab images and for the 37 landmarks in ten time points of the POPI-model using three different temporal control point spacings and with and without the cyclic motion constraint. Results are compared with the reference time point, consecutive time point, and groupwise registration approaches. The best previously published results are listed in the last row of the table.

	POPI	DIR-lab				
		Case 1	Case 2	Case 3	Case 4	Case 5
Initial	3.68 (2.97)	2.18 (2.54)	3.78 (3.69)	5.05 (3.81)	6.69 (4.72)	5.22 (4.61)
Temp. spacing of 3 time points (non-cyclic)	1.13 (0.59)	1.12 (0.75)	1.09 (0.73)	1.24 (0.69)	1.65 (1.12)	1.89 (1.74)
Temp. spacing of 2 time points (non-cyclic)	1.03 (0.56)	1.02 (0.70)	1.05 (0.70)	1.20 (0.68)	1.47 (1.03)	1.68 (1.49)
Temp. spacing of 1 time point (non-cyclic)	1.02 (0.58)	0.95 (0.66)	1.00 (0.62)	1.15 (0.61)	1.39 (1.02)	1.50 (1.32)
Temp. spacing of 3 time points (cyclic)	1.22 (0.79)	0.97 (0.71)	1.54 (1.30)	1.73 (1.28)	2.82 (2.29)	2.33 (1.99)
Temp. spacing of 2 time points (cyclic)	1.07 (0.58)	0.96 (0.71)	1.11 (0.77)	1.22 (0.71)	1.62 (1.15)	1.84 (1.64)
Temp. spacing of 1 time point (cyclic)	1.02 (0.58)	0.95 (0.66)	1.00 (0.62)	1.14 (0.61)	1.40 (1.02)	1.50 (1.31)
Groupwise	1.00 (0.56)	0.94 (0.65)	1.01 (0.61)	1.14 (0.63)	1.41 (1.04)	1.49 (1.30)
3D reference time point	0.95 (0.56)	0.93 (0.65)	0.89 (0.51)	1.05 (0.56)	1.40 (1.10)	1.27 (1.10)
3D consecutive time points	1.47 (1.08)	0.97 (0.71)	0.98 (0.61)	1.17 (0.66)	1.37 (0.97)	1.46 (1.40)
Kabus et al. (2009)	0.96 (0.56)	n.a.	n.a.	n.a.	n.a.	n.a.

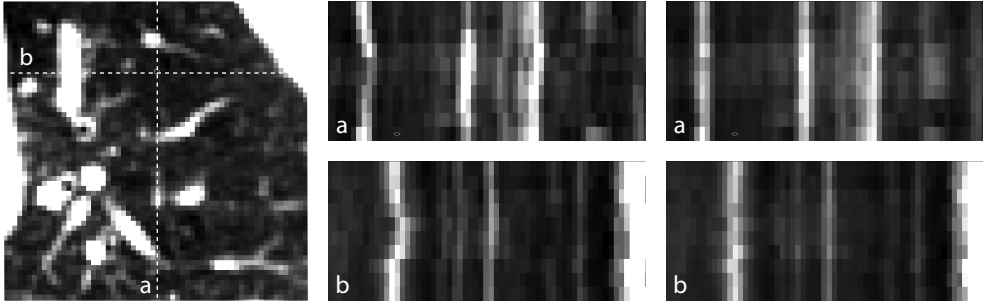


Figure 4.3: Registration result for a 3D+t CT image of the lungs. Left and middle: input image. Right: registration result. Image (a) and (b) show the dotted lines in the left image over time.

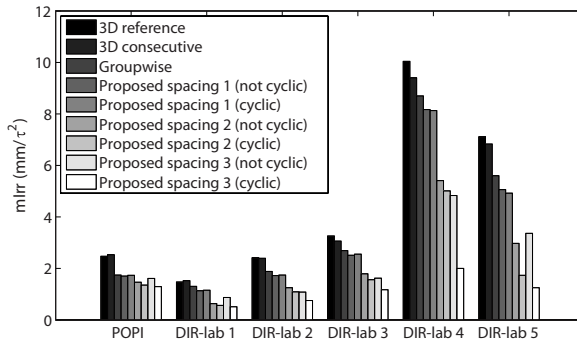


Figure 4.4: Irregularity of landmark trajectories using different registration approaches. Values are averaged over 75 landmarks for the DIR-lab images and over 37 landmarks for the POPI-model. Lower values mean smoother results.

poral spacing of the B-spline grid improves the temporal smoothness. The inclusion of the constraint on cyclic motion reduces the irregularity even further for larger temporal control point spacings. Furthermore, it can be noticed that the 3D reference registration method performs worst in this sense.

Inverse transformation

An experiment was conducted in which different spatial control point spacings for computation of the inverse transformation were tested. The result of the proposed method using a temporal control point spacing of 2.0 time points and the cyclic motion constraint from the previous sections was used as the forward transformation. Evaluation was performed on the POPI model. We tested spatial control point spacing for the inverse computation ranging from 13.0 mm (the spacing of the forward transform) to 7.0 mm. Subsequently, we computed the accuracy and irregularity of the results (Section 4.3.2), and the inverse errors. The multi-resolution strategy was the same as was used for the forward registration procedure. The inverse error was defined as the average magnitude

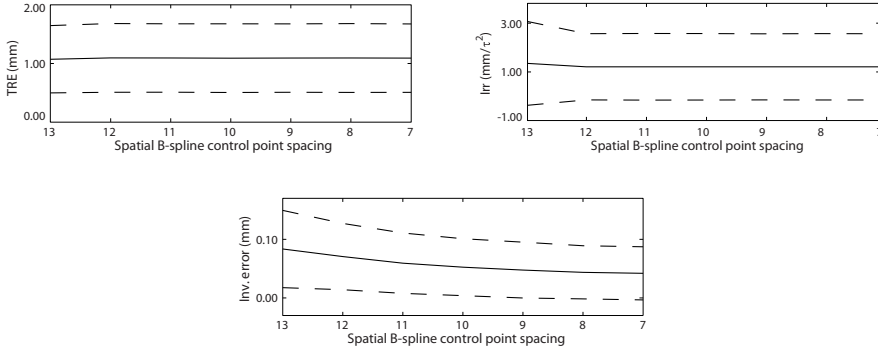


Figure 4.5: Results of the inverse experiment. The figures show the influence of the spatial control point spacing on the accuracy (TRE), irregularity (Irr) and inverse error. The solid lines represent the mean and the dashed lines show the mean \pm the standard deviation.

of the transformation vector after subsequent transformation with the forward and inverse transform. Errors were computed for all voxel positions within the mask used in the registration. Results are shown in Fig. 4.5. The dashed lines show the mean \pm the standard deviation of the TRE and irregularity values.

Transitive consistency

The registration results of the reference registration approach (Section 4.3.1) will depend on the chosen reference image. The choice of different reference images may thus lead to inconsistent results, where we define registrations transitive consistent when for all $i, j \in \mathcal{T}$ and all $\mathbf{x} \in \mathcal{S}$:

$$\mathbf{T}^{ij}(\mathbf{T}^{ki}(\mathbf{x})) = \mathbf{T}^{kj}(\mathbf{x}). \quad (4.14)$$

In the proposed method all time points are aligned simultaneously without the use of a reference time point, but there still remains an inconsistency, which is caused by errors in the approximation of the inverse transform.

To assess the inconsistency of both the reference time point and proposed cyclic approach, we performed an experiment on the POPI image. We computed the inconsistency errors as:

$$E^{ij}(\mathbf{x}) = \left\| \mathbf{T}^{ij}(\mathbf{T}^{ki}(\mathbf{x})) - \mathbf{T}^{kj}(\mathbf{x}) \right\| \quad (4.15)$$

for all $k \in \{1..T\}$, all voxel positions and all $i \neq j$. For the 3D reference approach, \mathbf{T}^{ij} were computed by pairwise 3D registration for all i, j . For the proposed method the \mathbf{T}^{ij} were computed according to Equation 4.11. Similar settings were used for both registration approaches. Results of these experiments are shown in a histogram in Fig. 4.6 with a solid line for the consecutive registration approach and a dashed line for the proposed registration method. The dotted vertical lines indicate the average inconsistency error for both approaches. The inconsistencies for the proposed registration approach are in

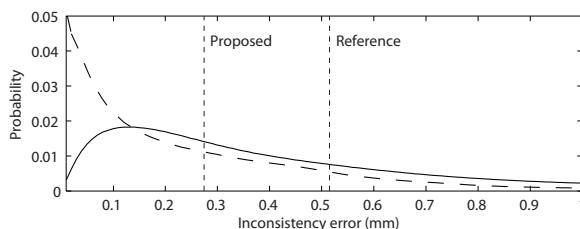


Figure 4.6: Histogram of the inconsistency results for the consecutive registration approach (solid line) and for the proposed registration method (dashed line). For visualization purposes the maximum value at the x-axis was set to 1.0 and the maximum value at the y-axis was set to 0.05. The dashed vertical lines indicate the average error for both approaches.

general smaller, which is apparent from the peak in the left of the histogram and the smaller average error value. The consistency errors for the 3D reference method could decrease with methods such as proposed by Christensen and Johnson (2001) and Geng et al. (2005).

4.3.5 Quantitative evaluation on 3D+t CTA data of the heart

An experiment was performed to assess the accuracy of semi-automatic derivation of left ventricular volume curves from 3D+t CTA data of the heart. To this end, the left ventricle was manually annotated for 5 patients at 10 time points in the cardiac cycle. The curves describing the left ventricular volume over the cardiac cycle were determined from these manual annotations. Subsequently, these curves were also generated by propagating the end-diastolic manual annotation to all other time points using the transformation resulting from the registration procedures. The proposed method was used both with and without imposing cyclic motion. Registration was performed in a two-step approach. First the registration was performed on the whole 4D image. Subsequently, an atlas based segmentation of the heart surface at end-diastole (Kirisli et al., 2010) was propagated to the whole sequence using the resulting transformation. In the second step the 4D registration was performed while using the 4D heart mask for computation of the dissimilarity metric, to be able to handle the non-smooth sliding motion of the heart along the lung surface.

The left ventricular volume curves derived from semi-automatically determined left ventricle surfaces and the manual measurements can be found in Figure 4.7. The average and standard deviation of the volume error was 3.02% ($\pm 2.46\%$) and 3.02% ($\pm 2.49\%$) for the cyclic and non cyclic registration approach respectively. An example of the imaging data before and after registration is shown in Figure 4.8.

4.3.6 Further examples on clinical data

To show the potential of the proposed registration method on other imaging modalities, registration was performed on a 2D+t ultrasound (US) image of the carotid artery and a pediatric 2D+t magnetic resonance (MR) image of the lungs.

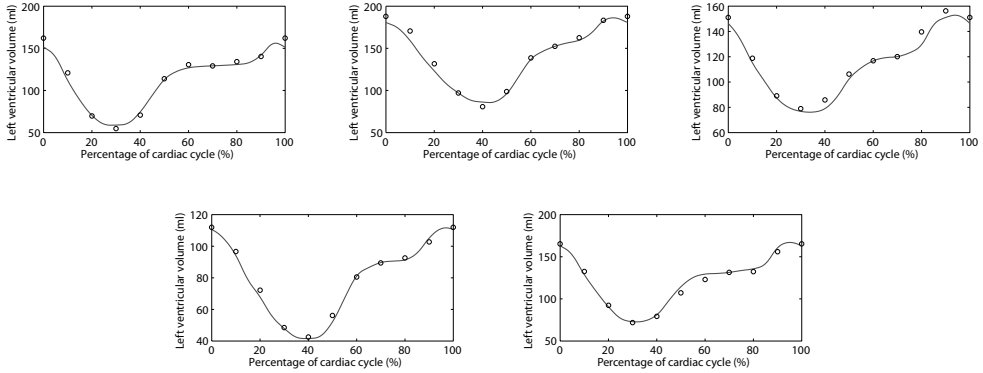


Figure 4.7: Left ventricular volume curves derived from 3D+t CTA data. Circles: manual measurements, solid line: proposed method with cyclic motion constraint.

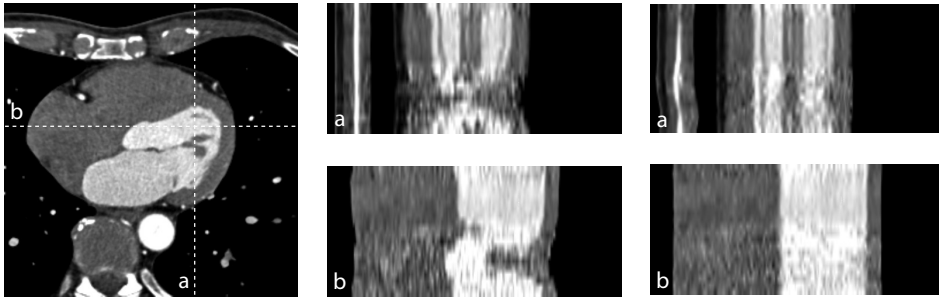


Figure 4.8: Registration result for a 3D+t CTA image of the heart. Left: input image, right: registration result. Image (a) and (b) show the dotted lines in the left image over time. The time varying noise levels, which are caused by variation of dose over the cardiac cycle (ECG-pulsing) (Weustink et al., 2009), are clearly visible and make the registration more challenging. Note that the left side of images (b) falls outside the heart mask used in the registration.

The US image of the carotid artery was acquired to measure the distensibility of the carotid artery (Gamble et al., 1994). This requires the accurate estimation of the vessel wall deformation. Images before and after registration are shown in Fig. 4.9.

The MR image of the lungs was acquired to analyze lung function in cystic fibrosis patients, which requires measuring the compression and decompression of the lungs over the respiratory cycle (Failo et al., 2009). The input image and the results after registration are shown in Fig. 4.10. The resulting images still show some misalignment, visible on the right side in image (a), caused by the anatomy moving in and out the field of view.

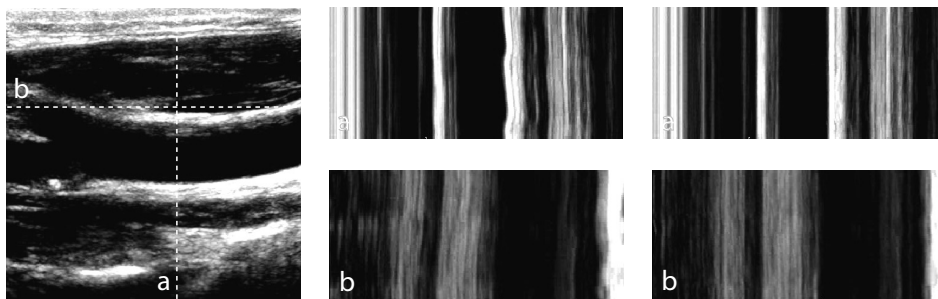


Figure 4.9: Registration result for a 2D+t ultrasound image of the carotid artery. Left and middle: input image, right: registration result. Image (a) and (b) show the dotted lines in the left image over time.

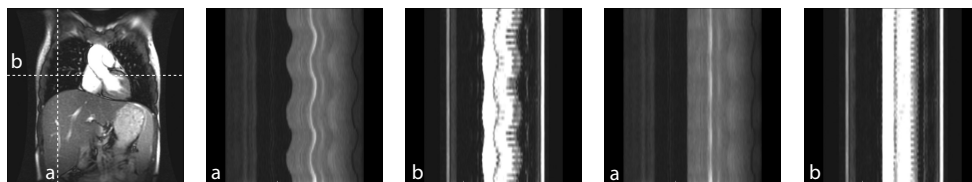


Figure 4.10: Registration result for a pediatric 2D+t MRI image of the lungs. From left to right: input image (first three), registration result (last two). Image (a) and (b) show the dotted lines in the left image over time.

4.4 Discussion

A registration method for motion estimation in dynamic medical imaging data combining a Lagrangian nD+t B-spline transformation model, a global cost function and global optimization strategy has been proposed and quantitatively evaluated.

In a synthetic experiment we compared the proposed approach with other existing registration approaches. It is demonstrated that the temporal smoothness and the constraint on cyclic motion help the registration when images are distorted by noise. Furthermore, the proposed method yields temporally smooth (continuously differentiable) transformations.

Quantitative experiments on 3D+t CT data of the lungs showed that the method was able to derive the dynamics from the images with subvoxel accuracy, which is comparable to previously published results of other state of the art image registration methods on the same data. Furthermore, it shows that temporally smooth results can be achieved by only compromising slightly on registration accuracy. The temporal smoothness of the results can be regulated by adapting the temporal control point spacing, which can be chosen in such a way that it takes into account the expected smoothness of the motion of the anatomy. This prevents the method to fit the transformation to errors in the imaging data, such as acquisition artefacts. Furthermore, cyclic motion can be enforced. We showed that this was only beneficial for one of the DIR-lab cases. A possible explanation for the decrease in accuracy for the other cases can be that the data is not as cyclic as expected, which is also suggested by the relatively low temporal smoothness for the non-



cyclic results of DIR-lab case 5 (see Figure 4.4). The use of cyclic motion constraints should therefore be considered carefully for the application of interest. It should be noted that previously published results on the DIR-lab data are not directly comparable to the values derived in this work, because only a subset of 300 from the approximately 1200 3D landmarks is publicly available. We do, however, expect these 300 landmarks to be a representative subset and the results therefore to be representative as well. Also, we computed all TRE values in world coordinates, while Castillo et al. (2010) round the transformed landmark coordinates to the closest voxel coordinate first. If we would follow their approach, the average values for our results would be the same and the standard deviations would be around 0.4 mm larger. In an experiment on the POPI model, we showed that the proposed method outperforms the often used reference time point method with respect to registration consistency. This is caused by the use of a global cost function, avoiding a bias towards a specifically chosen reference time point.

Further quantitative experiments on 3D+t CTA data of the heart showed the ability of the method to semi-automatically determine left ventricular volume curves with only a deviation from manually derived curves of approximately 3%. These deviations may be partly explained by errors in the manual annotations, because outlining the left ventricle is especially challenging at the location of the atrioventricular valves during fast moving phases of the cardiac cycle. Furthermore, contrary to the registration method, temporal continuity is not taken into account during manual annotation.

Examples on 2D+t ultrasound and MR images showed the potential of the method for other imaging modalities. Because the method is publicly available as an extension to `elastix`, it can readily be applied by other researchers to various types of dynamic medical imaging data.

We also described an approach to approximate an inverse B-spline transformation, which was used to find the relation between time points in the input image. Based on the application of interest one can choose to perform analyses on the registered image directly or relatively to a chosen reference time point. The errors of the inverse transformation were shown to be very small and even smaller when choosing a somewhat smaller spatial grid spacing for obtaining the inverse transformation than was used in the forward registration procedure. The accuracy was almost not affected by this smaller spacing, but a small effect on the smoothness of the results was noticed.

The method builds upon groupwise registration approaches, with the main difference that the smoothness in the temporal direction of the data is incorporated and that the transformations can be constrained to be cyclic. The advantage of this approach is that the alignment of the data does not depend on a chosen reference time point. Although the deformations between the time points and the used implicit reference frame might be larger than the deformations between consecutive time frames, this does not seem to affect registration robustness. This is most probably an effect of the temporal smoothness which helps to find these larger deformations. Additionally, these deformations are still relatively small compared with the inter-patient differences in group-wise registration. The error introduced when establishing the relation between time points in the input image through application of the inverse transformation was shown to be much smaller than the consistency errors made using the 3D reference registration approach.

Additional constraints on the transformation can be taken into account by adding ex-

tra penalty terms to the cost function (Bistoquet et al., 2008; Mansi et al., 2009; Sdika, 2008). These penalty terms could, for example, ensure inverse consistent transformations or impose biomechanical constraints on the transformations. This depends on the application, and is not pursued in our work.

It should be mentioned that the assumption of constant intensity over time does not hold in perfusion imaging, where contrast flow can cause the same anatomy to have a different appearance over time. The development of a similarity metric that accounts for contrast influx would therefore be an interesting future research direction as our groupwise $nD+t$ B-spline framework can accommodate different similarity measures, which may be selected based on different assumptions.

4.5 Conclusions

A registration method combining a Lagrangian $nD+t$ B-spline transformation model, a global cost function and global optimization strategy for motion analysis in dynamic medical imaging data was proposed. It takes smoothness into account in both the spatial and temporal direction of the data. Moreover, it can enforce the transformations to be cyclic. Registration accuracy and smoothness were assessed using a synthetic image, publicly available imaging data of the lungs and imaging data of the heart. On the synthetic image, the best results with respect to accuracy and smoothness were achieved using the proposed method while imposing cyclic motion. On the lung data, the accuracy was found to be comparable to previously reported results and the smoothness was found to be best when using the proposed approach. Furthermore, it was shown that the proposed method performs better than the reference time point registration method with respect to the consistency of the registration results. Regarding the cardiac CTA data, semi-automatically derived left ventricular volume curves showed a deviation of approximately 3% with respect to the curves derived from manual annotations. Further examples were shown on a $2D+t$ US image of the carotid artery and a $2D+t$ MR image of the lungs. The software is publicly available as an extension to the registration package *elastix*.

Acknowledgements

The authors would like to thank W.B. Vletter, J.G. Bosch, and K.Y. Leung, Thoraxcenter, Department of Cardiology, Erasmus MC, Rotterdam, The Netherlands, for providing the ultrasound images, R. Failo, H.A.W.M. Tiddens, Departments of Pediatric Radiology and Pulmonology, Erasmus MC, Rotterdam, The Netherlands and M. de Bruijne, Departments of Radiology and Medical Informatics for providing the MR images and L.A. Neefjes and N.R. Mollet, Departments of Radiology and Cardiology, Erasmus MC, Rotterdam, The Netherlands for providing the CTA images of the heart.

5

Cardiac Motion Prediction from Single-Phase CTA by Principle Component Regression

This chapter is based on the manuscript: Cardiac Motion Prediction from Single-Phase CTA by Principle Component Regression, **C.T. Metz**, N. Baka, H. Kirisli, M. Schaap, S. Klein, L.A. Neefjes, N.R. Mollet, B. Lelieveldt, M. de Bruijne, W.J. Niessen, T. van Walsum, *submitted*.

Abstract

State of the art cardiac CT enables the acquisition of imaging data of the heart over the entire cardiac cycle at high temporal resolution. However, due to the harmful effect of ionising radiation, these acquisitions are not always justifiable. Prospective electrocardiogram gating is therefore increasingly applied to reduce the patient dose, but this technique often limits reconstruction to a single 3D image. However, estimating the shape of the cardiac structures throughout the entire cardiac cycle is still useful for certain applications. We present a method to predict the motion of the cardiac structures for the entire cardiac cycle from shape information of a single phase. Motion prediction was performed by principle component regression via statistical shape and motion models. Our prior hypothesis in this approach is that the motion of the heart is at least partially explained by its shape. The second objective of this work is therefore to evaluate if shape-dependent motion prediction results in more accurate results than shape-independent motion prediction. Quantitative evaluation on 150 4D computed tomography angiography (CTA) images by leave-one-out experiments showed a significant increase in the accuracy of the estimated shape sequences compared to shape-independent motion prediction. The point-to-point and point-to-surface errors of the estimated shapes were 2.4 ± 0.6 mm and 1.4 ± 0.3 mm respectively.



5.1 Introduction

Statistical shape models have been widely applied for medical image segmentation (Heimann and Meinzer, 2009), since their introduction by Cootes et al. (1995). It is not surprising that these techniques have also been extensively applied for cardiac applications, most often for the delineation of the left ventricle. In this area, where artifact free image acquisition is challenging due to the fast moving anatomy, prior knowledge about plausible shapes may be beneficial for robust image segmentation. Examples are the delineation of the left ventricle in multi-slice computed tomography (MSCT) (van Assen et al., 2008; Fritz et al., 2005), magnetic resonance images (Shang and Dossel, 2004) and ultrasound images (Mitchell et al., 2002). Segmentation of more cardiac structures have also been addressed, for example, all four cardiac chambers in the work of Fritz et al. (2006), or the four chambers, myocardium and great vessels from 3D computed tomography (Ecabert et al., 2008). In the work Frangi et al. (2002), an automatic landmarking procedure for statistical modelling was presented and applied to the left and right ventricle in magnetic resonance images. These shape models are often point distribution models describing the statistics of the spatial distribution of anatomically corresponding landmarks from a set of training shapes.

State of the art image acquisition techniques make the acquisition of 4D images of the heart over the entire cardiac cycle possible at high temporal resolution (Li et al., 2008a). The application of statistical models for the segmentation of these sequences has therefore been investigated. Straightforward solutions are to create a separate model for every cardiac phase (Zhang et al., 2010d) or to train a single 3D model from shapes of all cardiac phases (Ordas et al., 2007). Although the latter approach is suited for segmentation, it does not allow to make the distinction between inter- and intra-patient shape variation, which is needed for the analysis or prediction of cardiac motion. Another approach is to perform statistical analysis on 4D landmark coordinates to derive a model of cardiac shape and motion. This approach was applied by Perperidis et al. (2005) for segmenting the left ventricle, right ventricle and myocardium. Zhang et al. (2010d) applied a two step approach to find both the left and right ventricle in MRI. In this method, first the whole sequence of shapes was segmented using a 4D shape model and subsequently, the segmentations for the individual time points were refined using per-phase 3D shape models.

4D statistical shape models have not only been used for cardiac application, but also for other anatomies, for example in respiratory motion modeling of the liver (Blackall et al., 2001) and motion modeling of the lungs (Ehrhardt et al., 2010).

Instead of modelling the coordinates of a set of landmarks, it is also possible to construct statistical models that describe the deformation with respect to a chosen reference image. This approach was used by Rueckert et al. (1999) to construct statistical deformation models describing the variability of 3D brain structures among a patient population. A similar approach was performed by Lapp et al. (2004) for 3D and 4D cardiac segmentation. Related to this work, Chandrashekar et al. (2003) performed statistical analysis on the registration parameters to substantially decrease the degrees of freedom in nonrigid registration of images at different cardiac phase.

Except for the method of Chandrashekar et al. (2003), the above mentioned meth-

ods have been used for image segmentation, hence the statistical models were fit to imaging data of the same dimensionality as the data from which the models were derived. However, in some situations only sparse information is available and the goal is then to reconstruct the full segmentation or motion from this information. For example, to minimize patient dose in computed tomography angiography (CTA), prospective gating techniques are increasingly applied, where data is solely acquired during a certain period of the cardiac cycle. In this case reconstruction is often limited to one 3D image. It is still useful to estimate the motion during the cardiac cycle from the available sparse data, for example, in the dynamic alignment of preoperative 3D CTA to intraoperative 2D+t X-ray in image guided interventions (Metz et al., 2009a). It is worth to mention that it is not obvious to use the predicted motion for direct diagnosis, rather for image analysis in which a motion prior is beneficial.

Some authors have investigated the prediction of cardiac motion or deformation from sparse temporal data. Ablitt et al. (2004) used partial least squares regression to predict breathing induced motion from navigator echoes. In the work of Hoogendoorn et al. (2009) and Figueras et al. (2010) cardiac shapes for the complete dynamic sequence were predicted from shape information available at a subset of phases throughout the cardiac cycle. In their work, shape variation between subjects and shape variation due to the cardiac cycle were explicitly decoupled by the application of bilinear models. Cardiac motion was therefore assumed to be independent of the shape of the heart. Motion prediction for non-cardiac applications was performed by Liu et al. (2010), using canonical correlation analysis to estimate dense motion fields of the lungs from sparsely sampled 4D shape information. Davatzikos et al. (2001) presented a general method to estimate anatomical deformation, in which principal component analysis is performed on vectors containing both the shape and deformation parameters. A least squares minimization approach was proposed to estimate the most likely deformation given the shape of the anatomical structure of interest. This method has been evaluated on synthetic images.

The combination of shape models and multi-variate regression has also been applied for non-motion related applications. For example, to estimate the shape of anatomical structures based on the shape of the neighboring structures. In the work of de Bruijne et al. (2007) a neighbor-conditional shape model based on ridge regression was used to quantify vertebral morphology. Yang et al. (2008) proposed to use partial least squares regression for the prediction of neighboring bone structures in the shoulder, which was also used in the work of Rao et al. (2008) for the prediction of brain structures. In Jeong et al. (2008) principal component regression was used to automatically outline the prostate based on known neighboring structures. In the work of Iglesias and de Bruijne (2007), principle component regression was used to determine vertebrae outlines in lateral X-ray images from small number of manually annotated landmarks.

In this chapter, we investigate cardiac motion prediction from 3D shape information extracted from a single phase CTA image. To this end, we build statistical shape and motion models of the heart and predict the motion from the shape by application of principal component regression. In contrast to the work of Hoogendoorn et al. (2009) and Figueras et al. (2010), we do not enforce independence between the shape and the motion of the heart. Instead, our method exploits any possible correlation between shape and motion of the heart and we evaluate the influence of this correlation on the accuracy



of the predicted surfaces.

The contribution of this work is three-fold:

- (i) We present a framework for cardiac motion prediction based on linear regression which takes into account the possible correlation between the shape and motion of the heart.
- (ii) To construct a training set, we present a fully automatic procedure to extract anatomically corresponding landmarks from ECG-gated 4D CTA.
- (iii) We investigate the value of taking into account shape-dependent motion by assessing the contribution of shape-related motion to the accuracy of the motion prediction.

The method is quantitatively evaluated by leave-one-out experiments on 150 4D CTA images by computing point-to-point and point-to-surface errors between the estimated 4D cardiac shapes and the reference standard. This work is an extension of a previously published MICCAI conference paper (Metz et al., 2010). Klinder et al. (2010) simultaneously developed a similar method for respiratory motion prediction, which was published concurrently.

5.2 Method

The proposed 4D motion prediction method builds upon the theory of statistical models and linear regression. In Section 5.2.1, we describe how we apply these techniques for cardiac motion prediction. In Section 5.2.2 and 5.2.3, we explain how to train the model on 4D CTA images. An overview of the method is given in Figure 5.1.

5.2.1 Shape-conditional motion prediction

The method consists of independent shape and motion models (Section 5.2.1), which are related using linear regression (Section 5.2.1).

Representation of shape and motion

Having P 4D segmentations of the individual structures of the heart, each segmentation S is represented by a sequence of T shapes \mathbf{s}_t :

$$S = \langle \mathbf{s}_1, \dots, \mathbf{s}_T \rangle, \quad (5.1)$$

one for each phase in the cardiac cycle. Each shape consists of a collection of K landmarks points, which are stored in a column vector:

$$\mathbf{s}_t = (x_1, y_1, z_1, \dots, x_K, y_K, z_K)^\tau. \quad (5.2)$$

The landmark points are located on the surfaces at anatomically corresponding locations both over time and between patients. To be able to model both shape and motion variation, we first define a reference phase r . This phase should correspond to the phase in

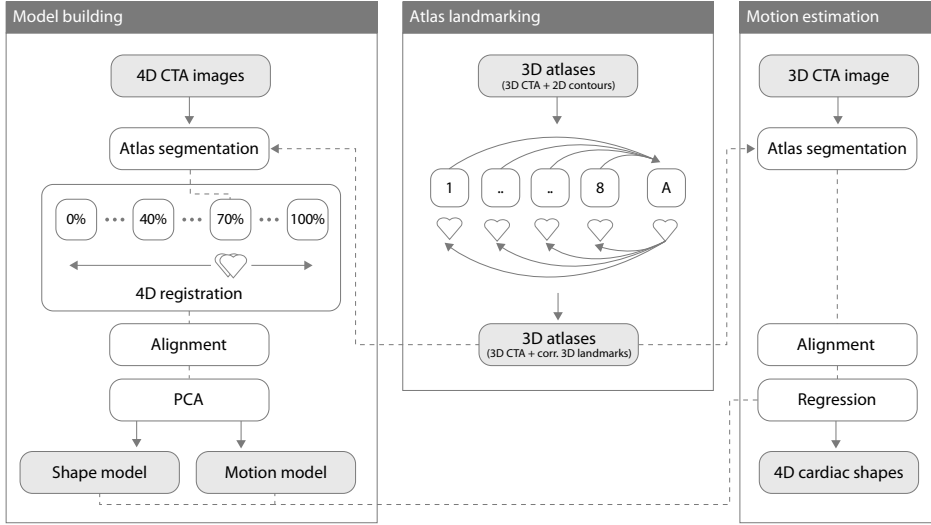


Figure 5.1: Overview of the cardiac motion prediction framework. Model building (left): (1) Landmarks are determined in a number of 4D CTA images by atlas segmentation of a reference time point (Section 5.2.2) and 4D registration (Section 5.2.2), (2) pose and heart rate variances are removed by aligning the landmark sets (Section 5.2.3) and (3) a shape and motion model is derived by performing PCA on the landmark coordinates and motion vectors (Section 5.2.1). Motion estimation (right): (1) Landmarks are determined in a 3D CTA scan by atlas segmentation, (2) The derived landmarks set is aligned with the mean landmark set of the shape model and (3) Motion is estimated by principle component regression (Section 5.2.1). For both procedures atlases are needed in which anatomically corresponding landmarks are determined (center, Section 5.2.2).

which the 3D shape information used for motion prediction is available at a later stage. Each shape sequence is now represented by a reference shape \mathbf{s}_r and a motion vector \mathbf{m} (with size $3TK$), describing the displacements from shape \mathbf{s}_r to the shapes at all T phases:

$$\mathbf{m} = ((\mathbf{s}_1 - \mathbf{s}_r)^\top, \dots, (\mathbf{s}_T - \mathbf{s}_r)^\top)^\top. \quad (5.3)$$

Motion prediction by principle component regression

To estimate the motion vectors from the shape landmark coordinates we apply a linear regression technique. Even though the underlying relation might be non-linear, a linear model is still desirable as in general the number of training data is much smaller than the number of parameters used. Using a non-linear model increases the risk of over-fitting substantially and will most probably result in high variance of the estimated model parameters.

By assuming a Gaussian distribution of the shape vectors \mathbf{s}_r and motion vectors \mathbf{m} respectively, their joint distribution can be written as a normal distribution $P(\mathbf{m}, \mathbf{s}_r) = N(\boldsymbol{\mu}_Z, \boldsymbol{\Sigma}_Z)$ with mean

$$\boldsymbol{\mu}_Z = \begin{bmatrix} \bar{\mathbf{m}} \\ \bar{\mathbf{s}}_r \end{bmatrix} \quad (5.4)$$



and covariance

$$\Sigma_Z = \begin{bmatrix} \Sigma_{mm} & \Sigma_{ms} \\ \Sigma_{sm} & \Sigma_{ss} \end{bmatrix}, \quad (5.5)$$

where Σ_{ss} and Σ_{mm} are the covariance matrices of shape and motion respectively, and $\Sigma_{ms} = \Sigma_{sm}$ is the covariance matrix between shape and motion. Following a linear regression approach, the motion for a given shape \mathbf{s}_r^* can be predicted by computing the mean of the conditional distribution $P(\mathbf{m}|\mathbf{s}_r^*)$ (Izenman, 2008):

$$\mathbf{m}^* = \bar{\mathbf{m}} + \Sigma_{ms} \Sigma_{ss}^{-1} (\mathbf{s}_r^* - \bar{\mathbf{s}}_r) \quad (5.6)$$

Multiple methods have been proposed to further regularize linear regression. Because the landmark locations are most probably highly correlated, we chose to use principle component regression and hence reduce the number of input and output variables by principle component analysis (PCA) on the shape and motion vectors respectively. A shape \mathbf{s}_r can then be represented by the mean shape $\bar{\mathbf{s}}_r$ and a linear combination of the modes of variation described by a parameter vector \mathbf{p} :

$$\mathbf{s}_r \approx \bar{\mathbf{s}}_r + \Phi \mathbf{p}, \quad (5.7)$$

where the columns of matrix Φ contain the highest eigenvectors resulting from the PCA corresponding to a certain percentage α of the shape variance to retain in the model. In a similar way, after PCA on the motion vectors, a motion sequence \mathbf{m} can be written as the mean motion $\bar{\mathbf{m}}$ and a linear combination of the modes of variation:

$$\mathbf{m} \approx \bar{\mathbf{m}} + \Psi \mathbf{q}, \quad (5.8)$$

where the columns of matrix Ψ contain the highest eigenvectors resulting from the PCA corresponding to a certain percentage β of the motion variance to retain in the model. In this work β is fixed to 95%.

Next, we use shape parameter vector

$$\mathbf{p}^* = \Phi^T (\mathbf{s}_r^* - \bar{\mathbf{s}}_r). \quad (5.9)$$

to predict motion parameter vector \mathbf{q}^* (Hastie et al., 2009). Replacing the original shape and motion vectors of Equation 5.6 by their respective parameter vectors gives

$$\mathbf{q}^* = \Sigma_{qp} \Sigma_{pp}^{-1} \mathbf{p}^*, \quad (5.10)$$

with \mathbf{q}^* the parameter vector representing the estimated motion. To ensure that the motion is plausible, \mathbf{q}^* is isotropically scaled such that it lies within ± 3 standard deviations of the motion model and the associated motion sequence \mathbf{m}^* is derived with Equation 5.8. The final estimated shape sequence \mathbf{S}^* is computed by combining the actual shape in the available cardiac phase (\mathbf{s}_r^*) with the estimated motion sequence \mathbf{m}^* :

$$\mathbf{S}^* = \langle \mathbf{s}_r^* + \mathbf{m}_1^*, \dots, \mathbf{s}_r^* + \mathbf{m}_T^* \rangle. \quad (5.11)$$

5.2.2 Landmarking

For computation of the shape and motion model described in Section 5.2.1, training segmentations S_p (with $1 \leq p \leq P$), consisting of anatomically corresponding landmark sets s_t , need to be determined for a number of 4D training images. Manual annotation of these landmarks would be very time-consuming. Therefore, we propose an automated procedure to derive such a training set from electrocardiogram (ECG) gated computed tomography angiography (CTA). The procedure consists of:

- (i) Determination of anatomically corresponding landmark positions between patients in one 3D (reference) phase of the cardiac cycle.
- (ii) Determination of anatomically corresponding landmark positions over time within patients.

We obtain the landmark correspondence between patients by multi-atlas segmentation of the end-diastolic frame of the image sequences, resulting in the landmark sets s_r (Section 5.2.2). To this end, anatomically corresponding landmarks are defined in the atlases (Section 5.2.2).

The temporal correspondence is then achieved by propagating the landmark set s_r from the end-diastolic phase to all other phases in the cardiac cycle by a 4D registration procedure, resulting in the complete shape sequences S_p (Section 5.2.2).

Determination of anatomically corresponding landmark positions between patients

We propose to use multi-atlas segmentation to derive anatomical landmark correspondence between patients. To this end we represent the manual segmentations by a number of surface landmarks a_j , with $1 \leq j \leq J$ and J the number of atlases available. These landmarks are located at anatomical corresponding locations among the atlases (see Section 5.2.2). We now define a transformation $T_u^j(\mathbf{x})$ which maps a point \mathbf{x} from atlas j to the patient image at the reference phase. Note that this transformation is defined in the opposite direction as is common in multi-atlas segmentation, as we want to transform landmarks instead of label images¹. We subsequently look for that transformation that optimally aligns the atlas and patient image:

$$\hat{u} = \arg \min_u C(u) \quad (5.12)$$

in which C denotes a cost function measuring the quality of the fit between the transformed patient and atlas image. In this work mutual information is used to compute these costs, and the nonrigid registration procedure was performed as described by Kirisli et al. (2010). By applying the resulting optimal transformation $T_{\hat{u}}^j(\mathbf{x})$ to the atlas surface landmarks, we map the points from atlas j to the patient image:

$$a'_j = T_{\hat{u}}^j(a_j) \quad (5.13)$$

¹In conventional multi-atlas segmentation transformation $T(\mathbf{x})$ maps points from the patient image to the fixed image. The labels are then propagated by transforming every voxel location of the patient image to the atlas image and looking up the label for that voxel.

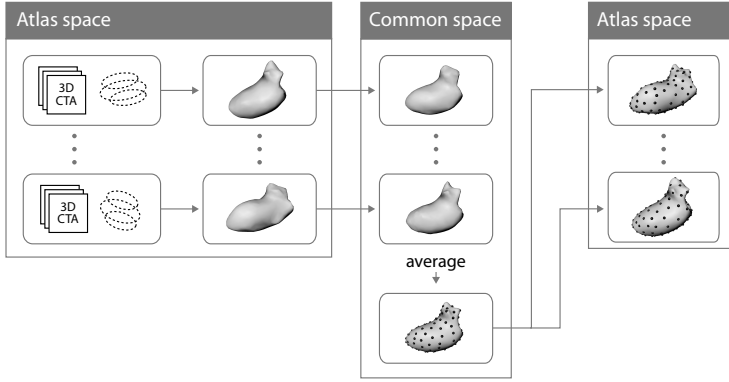


Figure 5.2: Atlas landmarking procedure: surface creation from manually annotated contours, creation of common space and mean surfaces, and transformation of mean surfaces back to atlases.

The final landmark set for a training image is then derived by averaging the J landmark sets \mathbf{a}'_j :

$$\mathbf{s}_r = \frac{1}{J} \sum_{j=1}^J \hat{\mathbf{a}}_j. \quad (5.14)$$

During the registration procedure, the cost function C is only computed on voxels that lie inside the heart surface. This ensures that neighboring structures located at different relative positions to the heart between patients, such as the ribs and spine, do not affect the quality of the alignment of the heart structures.

Anatomical landmark correspondence in atlases

A prerequisite for the landmarking procedure (Section 5.2.2) is the availability of anatomically corresponding landmarks in the J atlases. Each input atlas used in this work consists of a 3D end-diastolic CTA image and manually annotated contours of the following cardiac structures: pericardium, aorta (Ao), endocardium left ventricle (endoLV), epicardium left ventricle (epiLV), right ventricle, left atrium (LA) and right atrium (RA) (Kirisli et al., 2010). To establish corresponding landmarks on these annotated surfaces, we apply the following steps:

- (i) Mapping the J atlases to a common space.
- (ii) Averaging the J atlas surfaces per structure in this common space.
- (iii) Distributing landmarks across the resulting average surfaces.
- (iv) Mapping the surface landmarks back to the individual atlases.

An overview is given in Fig. 5.2 and details of the procedure are described below. The procedure is similar to the method presented by Frangi et al. (2002), but we directly use

a non-rigid transformation to align the atlases, perform pairwise alignment instead of a groupwise alignment, and define the similarity metric differently.

The first step of the atlas landmarking procedure, the creation of the common space, is based on pairwise alignment of the atlases. We perform a simultaneous alignment of the surfaces instead of aligning the intensity images, as the alignment is then only influenced by the structures of interest. Registration based on the intensity images is not preferred as the position and orientation of the heart with respect to the surrounding anatomy differs between patients. The surrounding anatomy will therefore deteriorate the quality of the alignment of the heart structures.

In order to register the manual segmentations, we first convert the annotated sets of 2D contour as available from the work of Kirisli et al. (2010) to 3D soft mask images by the following procedure.

We first fit a 3D surface to the manually annotated contours, which we denote with b . Subsequently, a signed distance function $f(\mathbf{x})$ to this surface is determined, where \mathbf{x} is a 3-dimensional voxel position in the mask image:

$$f(\mathbf{x}) = \begin{cases} d(\mathbf{x}, b) & \text{if } \mathbf{x} \text{ outside } b \\ -d(\mathbf{x}, b) & \text{if } \mathbf{x} \text{ inside } b \end{cases} \quad (5.15)$$

with $d(\mathbf{x}, b)$ the closest distance of \mathbf{x} to surface b . A soft mask image is then computed according to:

$$g(\mathbf{x}) = \text{erf}(-f(\mathbf{x})/\sigma_g) \quad (5.16)$$

with σ_g a parameter controlling the slope of error function $\text{erf}(\cdot)$. In this work σ_g was set to 0.8 mm. The values of $g(\mathbf{x})$ are minus one outside the surface, one inside the surface and smoothly vary from minus one to one at the border of the surface. By applying this error function, aliasing effects in the mask images are prevented.

Let $g_{ic}(\mathbf{x})$ be the soft mask image for atlas i and cardiac structure c . Furthermore, let $T_v^{ij}(\mathbf{x})$ be a B-spline transformation (Rueckert et al., 1999) aligning atlas i and j , described by a parameter vector \mathbf{v} . The pairwise alignment of two atlases i and j is now performed by finding that parameter vector $\hat{\mathbf{v}}$ that minimizes the sum of squared differences between the masks:

$$D_{ij}(\mathbf{v}) = \sum_{c=1}^C \sum_{\mathbf{x} \in X} (g_{ic}(\mathbf{x}) - g_{jc}(T_v^{ij}(\mathbf{x})))^2, \quad (5.17)$$

with X the set of voxels in the image and C the number of cardiac structures. Registration parameter settings are adopted from Kirisli et al. (2010).

The transformation $T^i(\mathbf{x})$ to map atlas i to the common space is determined by averaging all pairwise transformations $T_v^{ij}(\mathbf{x})$:

$$T^i(\mathbf{x}) = \frac{1}{J} \sum_{j=1}^J T_{\hat{\mathbf{v}}}^{ij}(\mathbf{x}). \quad (5.18)$$



These transformations are used to transform all atlas surfaces b to the common space, after which their signed distance functions are determined and averaged per structure:

$$f'_c(\mathbf{x}) = \frac{1}{J} \sum_{j=1}^J f'_{ic}, \quad (5.19)$$

with f'_{ic} the signed distance function of surface c and atlas i , created in the common space, and f'_c the signed distance function of the average surface of structure c . The mean surface is extracted at the zero level set of f'_c . A landmark set \mathbf{a} is generated by sampling surface points at approximately equally distributed locations. Finally, these landmarks are mapped back to the individual atlases by pair-wise registration of the soft masks of the mean surfaces and the soft masks of the surfaces in the individual atlases. The landmark set in atlas j is denoted with \mathbf{a}_j .

Determination of anatomically corresponding landmark positions over time

After determining landmark set \mathbf{s}_r for a training image by multi-atlas segmentation of the image at phase r (Section 5.2.2), the next step is to propagate the landmarks to anatomically corresponding locations throughout the entire cardiac cycle to form the landmark sequence S . We use the method presented in Metz et al. (2010) which was shown to perform well on (among others) cardiac data for the extraction of left ventricular volume curves. The method searches for the 4D B-spline transformation that aligns all time point images with reference phase r . To this end, it aims to minimize the variance of intensity values at corresponding voxel locations over time. Displacements in the time dimension are not allowed. Due to the 4D B-spline parametrization of the transformation, both spatial and temporal smoothness is achieved. Additionally, the motion is enforced to be cyclic, which implies that there is a smooth transition in the transformation between the last and first frame of the sequence.

A two-step approach is applied. First, the 4D registration is performed on the whole 4D image and the surface of the pericardium is subsequently propagated to the entire sequence using the resulting transformation. In the second step, the 4D registration is performed, while computing the dissimilarity metric only inside the pericardial surface, to account for non-smooth sliding motion of the heart along the lung surface. The resulting transformation is applied to \mathbf{s}_r to propagate the landmarks to the complete sequence.

For the experiments performed in this work, the spatial and temporal B-spline control point spacing were set to 15 mm and 1 time point (5% of the cardiac cycle) respectively. Per resolution level, 2000 iterations were performed. The number of spatial samples used to compute the dissimilarity metric was set to 2000 and the temporal number of samples was set to 5. For efficiency, quadratic B-splines were used for the parameterization of the transformation.

5.2.3 Alignment of landmark sequences

After application of the procedure described in Section 5.2.2, we have a set of landmarked 4D imaging data. Directly creating the statistical models from these landmark sequences would include the following undesired variations in the model:

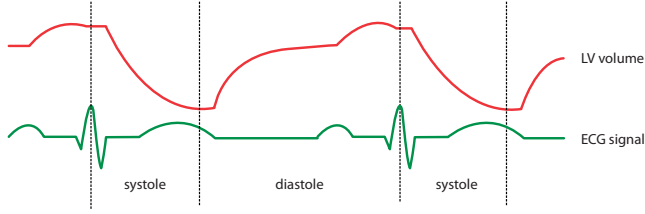


Figure 5.3: The change of left ventricular volume with respect to the ECG signal. By aligning the left ventricular volume curves, we implicitly align the ECG signals of the patients.

- (i) Temporal variations due to, for example, different patient heart rates.
- (ii) Variations due to the position and orientation of the patient in the scanner and the position and orientation of the heart within the patient.

In the following sections, we describe how these variances are removed from the training data.

Removing heart rate variations: temporal alignment

The landmark sequences derived by the procedure described in Section 5.2.2 are not sampled at physiologically corresponding temporal positions. This is, among others, caused by the ECG-gated reconstruction procedure: every time point image has been reconstructed at regular locations of the RR interval. Because the QT interval is, for example, known to be non-linearly related to the heart rate (Bazett, 1920), the linear scaling of the RR interval as pursued in the reconstruction procedure is not sufficient to remove non-linear variations.

We propose to remove this variation by determining physiologically corresponding temporal positions among the training sequences and interpolating the landmark sequences at these new temporal positions. Ideally, this interpolation is achieved by relating the ECG-signals, which are unfortunately not always available or stored in an unknown vendor-specific format. We therefore implicitly align the ECG signals of the patients by aligning their related left ventricular (LV) volume curves (Figure 5.3). Aligning LV volume curves was proposed previously by Peyrat et al. (2010) for image registration, but details of their curve alignment approach were not published. Figure 5.4(a) shows the LV curves for the training data used in this work before alignment.

The non-linear alignment of the curves consists of an groupwise registration procedure in which all curves are aligned with the mean curve. In the first iteration of the algorithm, the mean curve is chosen to be the curve which is closest to the average of all input curves. In subsequent iterations, the mean curve is determined by averaging all aligned curves. This procedure is repeated a number of iterations.

The alignment of two curves is performed using a 1D registration procedure. We first define the transformation model $T_w(t)$ to be a third order polynomial parameterized by four control points (Figure 5.6(a)). The first and last control point are fixed at 0% and 100% of the RR interval respectively. The positions of the intermediate two control

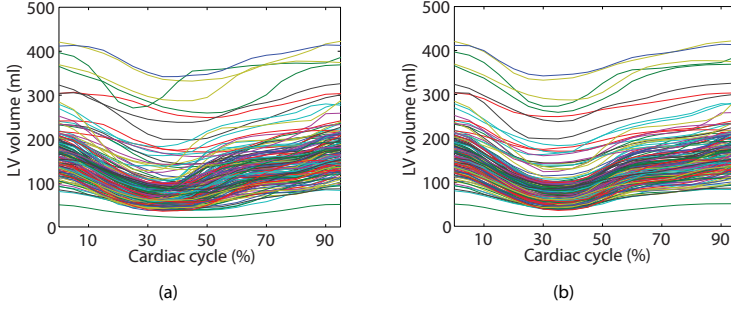


Figure 5.4: Left ventricular volume during the cardiac cycle before (a) and after alignment of the volume curves (b) in ml. Each line represents a patient.

points are optimized to optimally align the two curves (Figure 5.6(b) shows examples of possible transformation). We denote a left ventricular volume curve with $z_i(t)$ and define the similarity metric as the normalized cross correlation \mathcal{N} between z_i and the reference curve z_r :

$$\mathcal{N}(z_i, z_r) = \frac{1}{T-1} \sum_{t=1}^T \frac{(z_i(T_w(t)) - \bar{z}_i)(z_r(t) - \bar{z}_r)}{\sigma_{z_i} \sigma_{z_r}}, \quad (5.20)$$

with \bar{z}_i and σ_{z_i} the mean and standard deviation of the values of curve z_i respectively. Normalized cross correlation ensures that the absolute volume differences due to, for example, different sizes of the heart are not influencing the alignment. To derive curve values $z_i(T_w(t))$ at non-grid positions, linear interpolation is applied. Optimization is performed by exhaustively searching for the optimal positions of the two free control points.

The result of this iterative alignment procedure is shown in Figure 5.4(b). We perform five alignment iterations and discretize the temporal axis at 1% intervals for the possible positions of the two control points that determine the transformation of the curve.

After convergence of the curve alignment, the 4D landmark sets S are resampled according to the new time point positions using cubic interpolation.

Removing position and orientation variations: spatial alignment

The variances in the training landmark sequences due to patient and heart position and orientation are removed by Procrustes analysis (Goodall, 1991) on the P landmark sets s_r . This alignment procedure optimizes the translation, rotation and isotropic scaling of the shapes. The resulting transformation is applied to the entire sequences S .

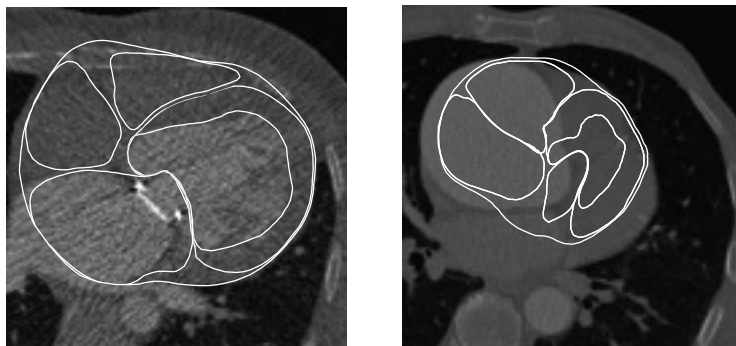


Figure 5.5: Images excluded from the experiments after visual inspection because of segmentation failure. Left: high noise dataset with artifacts caused by artificial valve. Right: large anatomical deviation due to aortic aneurysm.

5.3 Experiments and results

5.3.1 Imaging data

To derive the training landmark sequences, 170 retrospectively ECG gated 4D CTA images were collected. The scans were made for clinical diagnosis or research purposes and represent large variability in anatomy and pathologies. Images were acquired between September 2006 and March 2010 using a Siemens Definition or Siemens Definition Flash scanner. Reconstructions were made at every 5% of the cardiac cycle, resulting in 20 images per sequence. The field of view used for the reconstruction was 256×256 and the resulting voxel size is approximately $0.7 \times 0.7 \times 0.9 \text{ mm}^3$. The number of slices is on average 140. The slice thickness is 1.5 mm. Histogram equalization was performed on the CTA images, because a preliminary study revealed a positive effect on the 4D registration results.

For the multi-atlas based landmark propagation to the end-diastolic image, the eight manually segmented 3D atlases of Kirisli et al. (2010) were used.

5.3.2 Landmark propagation

The procedure described in Section 5.2.2 was performed to automatically determine anatomically corresponding landmarks in the 170 4D CTA images. The quality of the resulting surface sequences was scored by the first author as sufficient or insufficient for inclusion in the model by visual inspection. Surfaces were only scored insufficient in case of large errors. Consequently, twenty of the 170 landmark sequences were excluded from model building, resulting in a total number of 150 landmark sequences. Failures were caused by artifacts in the data, such as caused by the presence of a pacemaker, and large anatomical deviations from the atlases due to pathologies, for example, large aortic aneurysms. See Figure 5.5 for some examples. The following number of landmarks were used for the Ao, endoLV, epiLV, pericardium, LA, RA and RV respectively: 968, 2434, 3465,

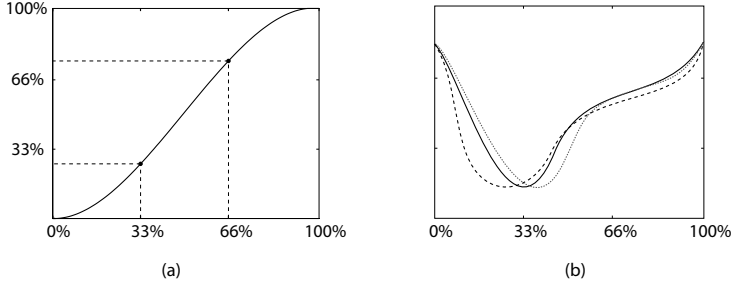


Figure 5.6: Left ventricular volume curve alignment: the temporal transformation is described by a third order polynomial which is based on the position of two control points (a). Examples of possible transformations of the solid curve are shown in (b).

7383, 1768, 1748 and 3084. The pericardium was only used to mask the computation of the dissimilarity metric in the 4D registration procedure (Section 5.2.2). All other structures were used for model building and motion prediction.

5.3.3 Accuracy of shape-conditional and mean motion

The motion of the four chambers and the aorta was predicted simultaneously based on the end-diastolic segmentation, by applying the conditional model described in Section 5.2.1. The end-diastolic phase (viz. at 70% of the RR-interval) was chosen as the reference phase r . Subsequently, 3D surface landmarks were determined at this reference time point by multi-atlas segmentation. The resulting landmark set was aligned (translation, rotation and isotropic scaling) with the mean shape \bar{s}_r of the shape model, after which the motion was predicted (Equation 5.10). The predicted motion was combined with the atlas-segmented 3D shape according to Equation 5.11, after which the 4D shapes were mapped back to the patient space using the inverse of the alignment transformation.

The accuracy of the motion prediction was evaluated in nested leave-one-out experiments on the training landmark sequences. The training data is repeatedly (150 times) divided into a set of 149 training shapes and one testing shape. The optimal value of α (the percentage of shape variance to retain) for a specific testing shape was determined by performing an inner leave-one-out experiment on the respective 149 training shapes. To this end, variances from 5% to 100% with steps of 5% were tested and the best performing α value is stored. To keep the running time within reasonable limits, only 30 of these inner leave-one-out iterations were performed per testing shape. After these 30 iterations the most often optimal α value was selected to be used for motion prediction in the outer leave-one-out iteration.

The performance of our method was compared to the accuracy achieved by overlaying the mean motion \bar{m} on the atlas segmented 3D shape:

$$S^m = \langle s_r^* + \bar{m}_1, \dots, s_r^* + \bar{m}_T \rangle, \quad (5.21)$$

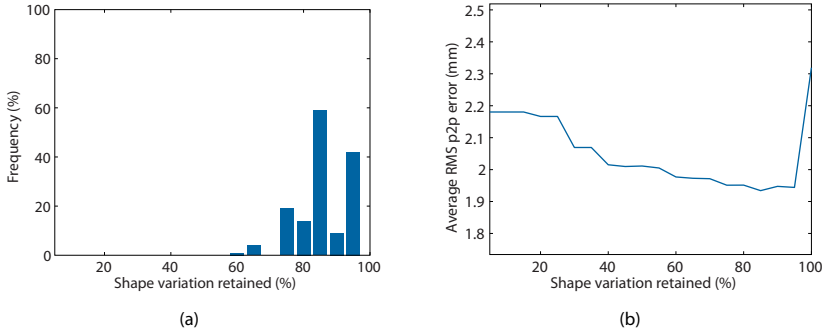


Figure 5.7: Histogram of optimal shape variance percentages selected for motion prediction (a) and influence of percentage of shape variance retained on the accuracy (point-to-point error in mm) of motion prediction averaged over 150 patients (b).

where we denote with S^m the shape sequence resulting from this approach. When it is assumed that the shape and motion of the heart are uncorrelated, S^m would maximize the prediction accuracy based on single phase shape information.

The accuracy is expressed in the average root mean squared point-to-point and point-to-surface distance to the training shapes (as derived by the procedure described in Section 5.2.2) per structure and time point. Next to the accuracy of mean and shape-conditional motion, we list the point-to-point and point-to-surface distances between the surface at the reference time point and the surfaces at all other time points to give insight in the magnitude of the motion. To test if shape-dependent motion prediction was significantly better than shape-independent motion prediction, a paired t-test was performed between the per structure point-to-point errors of the mean motion and the predicted shape-conditional motion in which the number of patients was used as the sample set size.

Results of the predictor optimization based on the variance of the shape model are shown in Figure 5.7(a) and 5.7(b). The first figure shows a histogram of the optimal percentages selected and the second shows how much the average root mean squared point-to-point error over all patients depends on the percentage of variance retained in the shape model. The most often optimal percentage of variance to retain was 85% with a corresponding number of shapes modes of 30 or 31. It can be noticed from Figure 5.7(b) that the accuracy is not very much influenced by slight changes in this value, as the graph is relatively flat between 75% and 95%.

Table 5.1 and 5.2 show the accuracy of the estimated shapes over all phases and averaged over the systolic phase respectively. Figure 5.8 shows per structure the average accuracy for the mean motion (dotted) and shape-conditional motion (solid) over the cardiac cycle. The tables and graphs show that shape-conditional motion prediction, as proposed in this work, performs better than shape-independent motion prediction by application of the mean motion. Additionally, the paired t-test showed that these differences are statistically significant. Resulting p-values are smaller than 0.01 for all

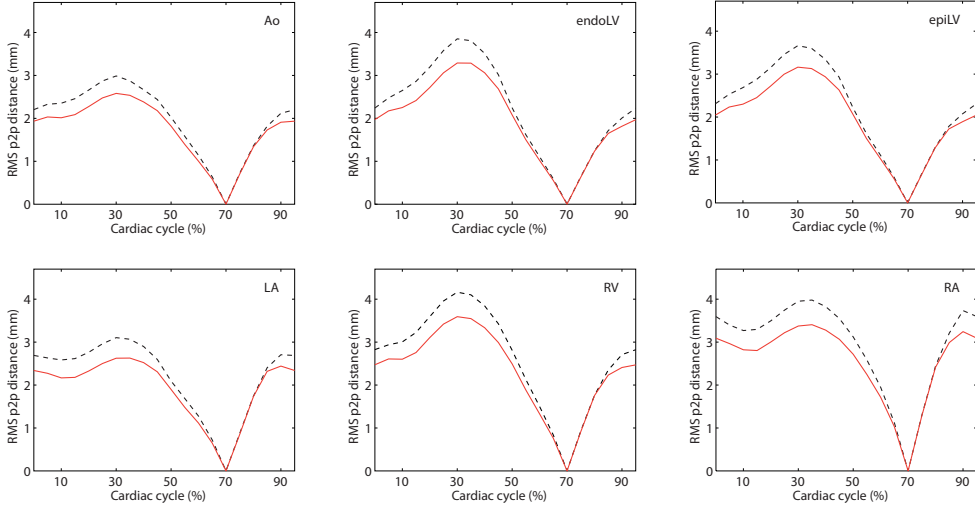


Figure 5.8: Accuracy of shape-conditional motion (solid) and mean motion (dotted) reported separately for all structures in mm.

structures.

5.3.4 Training set size

In this experiment, we investigated the dependency of the accuracy of the estimated shape sequences on the training set size. K -fold cross validation was performed. First, the data was randomly partitioned into $K = 10$ subsets. Subsequently, for every training set size, all possible combinations of subsets were used as training data and for each of these combinations a randomly selected hold out subset was used to compute the accuracy of the model. Based on the results of the experiment described in Section 5.3.3 we used the modes describing 85% of the variance of the shape model as motion predictors. The accuracy was determined as the root-mean-squared (RMS) point-to-point (p2p) error averaged over all patients and structures. The results for both the mean and shape-conditional motion are shown in Figure 5.9. Two important observations can be made from this figure. The first one is that the accuracy of motion prediction by application of the mean motion does not substantially change by adding training data. Adversely, the accuracy of shape-conditional motion prediction improves when adding more training data. In addition, the results indicated that it is probably beneficial to add even more training data, as the downward trend in the graph is still visible at the maximum amount of training data tested.

Table 5.1: Mean and standard deviation of the RMS error of mean and shape-conditional motion over all time points compared to the initial distance to the diastolic shape. Both point-to-point (p2p) and point-to-surface (p2s) errors are reported in mm.

	Ao	endIV	epIV	RV	LA	RA	All
p2p	initial displacement	3.9 ± 0.9	4.8 ± 0.9	4.5 ± 0.8	5.4 ± 1.2	4.1 ± 0.9	5.5 ± 1.5
	mean motion	2.2 ± 0.6	2.5 ± 0.6	2.5 ± 0.6	3.0 ± 0.8	2.4 ± 0.7	3.2 ± 1.1
	shape-conditional motion	1.9 ± 0.5	2.2 ± 0.5	2.2 ± 0.5	2.6 ± 0.7	2.1 ± 0.6	2.8 ± 0.9
p2s	initial displacement	2.0 ± 0.4	3.4 ± 0.7	2.7 ± 0.6	3.4 ± 0.7	2.3 ± 0.4	2.9 ± 0.6
	mean motion	1.1 ± 0.3	1.5 ± 0.4	1.4 ± 0.4	1.7 ± 0.5	1.5 ± 0.4	1.8 ± 0.5
	shape-conditional motion	1.0 ± 0.3	1.3 ± 0.4	1.2 ± 0.3	1.5 ± 0.4	1.3 ± 0.4	1.6 ± 0.5

Table 5.2: Mean and standard deviation of the RMS error of mean and shape-conditional motion for the systolic time point only, compared to the initial distance between the diastolic and systolic shape. Both point-to-point (p2p) and point-to-surface (p2s) errors are reported in mm.

	Ao	endIV	epIV	RV	LA	RA	All
p2p	initial displacement	6.2 ± 1.8	8.7 ± 1.7	7.9 ± 1.6	9.1 ± 2.3	6.5 ± 1.9	8.5 ± 2.9
	mean motion	3.0 ± 1.1	3.9 ± 1.2	3.7 ± 1.1	4.2 ± 1.4	3.1 ± 1.1	4.0 ± 1.7
	shape-conditional motion	2.6 ± 1.0	3.3 ± 1.0	3.1 ± 0.9	3.6 ± 1.2	2.6 ± 0.9	3.4 ± 1.4
p2s	initial displacement	3.1 ± 0.8	6.4 ± 1.3	5.0 ± 1.1	5.9 ± 1.4	2.9 ± 0.8	3.7 ± 1.0
	mean motion	1.5 ± 0.6	2.4 ± 0.9	2.1 ± 0.7	2.3 ± 0.8	1.9 ± 0.7	2.2 ± 0.9
	shape-conditional motion	1.3 ± 0.5	2.0 ± 0.7	1.8 ± 0.6	2.0 ± 0.7	1.5 ± 0.6	1.8 ± 0.8

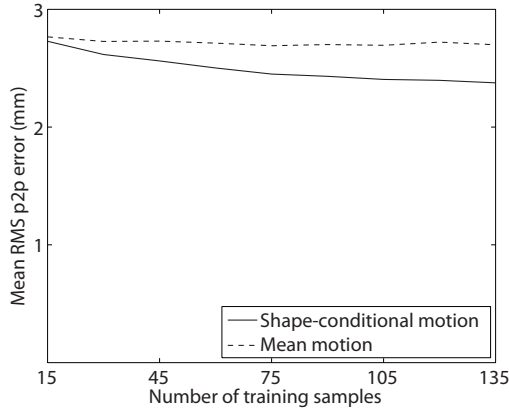


Figure 5.9: Relation between the number of training shapes and the accuracy. The dashed and solid line show the mean RMS p2p errors (mm) of the mean and shape-conditional motion respectively. RMS errors were computed per dataset over all cardiac structures.

5.3.5 Visualization of the relation between shape and motion

To visualize the relation between shape and motion, we performed the following experiment. Using all available data, we built both the shape and motion models for the endocardium of the left ventricle. We then varied the shape by using values of -3, 0 and +3 standard deviations as the parameters for the first and second mode of variation of the shape model and predicted the motion for this shape. Note that parameter values of zero will generate the mean shape and result in a prediction of the mean motion by definition. We visualized the shape-dependent motion differences by coloring the magnitude of displacement (point-to-point distance) between diastole and systole on visualizations of the predicted systolic shape. Figure 5.10 shows these visualizations together with the end diastolic shapes (in grey) from which the motion is predicted. Two different views for every shape are given. The two first modes explain mainly how elongated the left ventricle is. It can be noticed that a less elongated left ventricle shows a more isotropic contraction than an more elongated one.

5.4 Discussion

We presented a method to predict cardiac motion from the shape of the heart at end-diastole and evaluated its performance by leave-one-out experiments on 150 cardiac shape sequences. The main novelty of the presented framework is that it enables to incorporate the correlation between the shape and motion of the heart, which was shown to significantly improve the accuracy of the predicted cardiac shape over the entire heart cycle. This result is relevant for applications in which 4D shape models of the heart are beneficial, e.g. in relating 3D preoperative cardiac data to 2D+t intraoperative X-ray angiography.

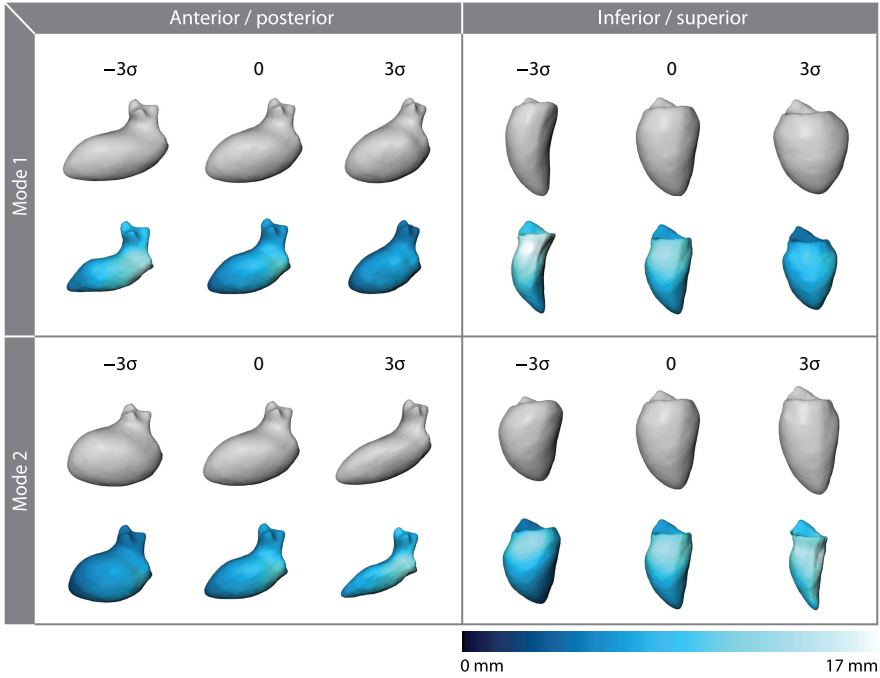


Figure 5.10: Relation between shape and motion: the grey surfaces show the end diastolic shape for a given mode configuration; the colored surface shows the predicted systolic shape and the magnitude of the displacement between the end-diastolic and systolic shape. The two first modes mainly explain how elongated the left ventricle is. Furthermore, it can be noticed that a less elongated left ventricle shows a more isotropic contraction than a more elongated one.

In a qualitative experiment, we visualised the correlation between the shape and motion of the heart by showing the first two modes of variation of the shape model and its impact on the predicted motion (Figure 5.10). For the first mode, it is clearly visible that a less elongated left ventricle shows a more isotropic contraction. The proposed method enables to gain more insight into these kind of correlations.

We specifically developed our approach for cardiac motion prediction based on a single frame only. In principle, the method could also be adapted to situations in which multiple time frames are available. Previous work on the same topic by Hoogendoorn et al. (2009) and Figueras et al. (2010) is especially suited for these situations in which multi-phase shape information is known. The best possible estimate of these methods for cases in which only a single 3D shape is known is the mean motion. With the presented method, shape information at a single phase can be used for patient-specific cardiac motion prediction, which in our experiments was shown to perform significantly better.

To extract the training landmark sequences from 4D CTA data, we proposed a fully automatic approach based on multi-atlas based segmentation and 4D registration. Although this procedure was only applied to CTA data, the method can potentially be used



to derive motion models from other modalities such as dynamic MRI as well.

Motion prediction was performed by principal component regression. The selection of the predictors was thus based on retaining a certain percentage of the variance of the shape model. Although the actual value of this parameter was optimized, other selection methods may result in a better performance, as the parameters explaining the highest variations in the shape model are not necessarily the best predictors of the motion. Investigation of predictor selection and other prediction techniques, such as partial least squares regression (Geladi and Kowalski, 1986), are subject to future work.

In the experiments, we assumed that the temporal position of the predicting 3D shape within the temporally aligned space of the training data is known. In real clinical situations, this might not be the case. If, however, an ECG signal is recorded, this relation can be determined by relating the recorded ECG signal to the aligned left ventricular volume curves of the training shapes (see Figure 5.3). Small errors in this procedure are expected to cause only minor changes in accuracy, as the heart is relatively stable at end-diastole. After estimating the motion, the resulting 4D shape should be mapped back from the mean space of the groupwise curve alignment to the patient space using the ECG signal. These ECG signals are always recorded during interventions and cardiac image acquisition, which does therefore not impose additional requirements for application of the proposed method. In future work, we would like to investigate the application of motion prediction in the alignment of preoperatively acquired 3D CTA data to intraoperatively acquired 2D+t X-ray images.

The method was evaluated by computing the errors with respect to the surfaces derived by multi-atlas registration and 4D registration. Errors introduced by the procedure to extract these training surfaces from the data are therefore not included in the presented results, but both the multi-atlas segmentation and 4D registration procedure have been evaluated before on cardiac data (Kirisli et al., 2010; Metz et al., 2010).

It can be deduced from the training set size experiment (Figure 5.9) that the use of more training data in building the model might still improve the accuracy of motion prediction. This can be explained by the high variability of cardiac shape and motion, and the pathological nature of the training data.

5.5 Conclusions

A method was presented to predict cardiac motion from the end-diastolic shape of the heart. Furthermore, a framework was proposed to derive landmark sequences to train the method from a set of 4D CTA images. It was shown that the proposed shape-conditional approach significantly improved the accuracy of the predicted motion compared to shape independent motion prediction by application of the mean motion.

Acknowledgements

All registrations were performed using *elastix* (Klein et al., 2010). Normal estimation, surface reconstruction and SDM computation were implemented using the Computational Geometry Algorithms Library (CGAL) (Fogel and Teillaud, 2006). Image and sur-

face storage was implemented using ITK (Yoo et al., 2002b) and VTK (Schroeder et al., 1997). Landmark redistribution was performed using MeVisLab (MeVisLab, Software for Medical Image Processing and Visualization).

6

Alignment of 4D Coronary CTA with Monoplane X-Ray Angiography: A Feasibility Study

This chapter is based on the manuscript: Alignment of 4D Coronary CTA with Monoplane X-Ray Angiography: A Feasibility Study, **C.T. Metz**, M. Schaap, S. Klein, P.R. Rijnbeek, L.A. Neeffjes, N.R. Mollet, C. Schultz, P.W. Serruys, W.J. Niessen, T. van Walsum, *in preparation*.

Abstract

In this chapter, we investigate the feasibility of a 3D+t/2D+t registration strategy to relate preoperative CTA to intraoperative X-ray angiography. To achieve this we use the methods introduced in the previous chapters for creating a patient-specific 4D model of the geometry and motion of the coronary arteries. Subsequently, we temporally register this preoperative model to the intraoperative imaging data by means of ECG alignment. In the final step of the method, we spatially align the temporally aligned model to the intraoperative imaging data. A nonlinear conjugate gradient optimizer is used to optimize a similarity metric based on 3D coronary centerlines projected onto the X-ray image and a fuzzy segmentation of vessel structures in this image. The spatial alignment is simultaneously performed on multiple X-ray images within a temporal window, also taking into account motion due to respiration. We evaluate the approach by comparing projected centerlines with manually annotated 2D centerlines in the X-ray images. In the experiments we show that the proposed registration approach has advantages over the more classic 3D/2D approach in terms of registration success and reproducibility.



6.1 Introduction

Percutaneous coronary intervention (PCI) is an often used minimally invasive procedure to reopen coronary arteries which are narrowed due to advanced atherosclerosis. The procedural success rate of PCI is very high (>98%; Tsuchida et al., 2007; Hoyer et al., 2005), but certain cases remain difficult to treat and might therefore be referred for coronary artery bypass grafting (CABG). CABG is far more invasive as the chest of the patient needs to be opened. Additional risks, such as uncomfortable sternotomy, infections, pulmonary emboli and stroke are inherent to this type of major surgery (Grech, 2011).

In PCI, narrowing or occlusion of coronary arteries is treated by moving a guidewire from a blood vessel in the upper thigh to the site of the lesion. Once the guidewire is in place, a hollow balloon catheter is positioned over the guidewire and the vessel is widened by inflation of the balloon. Often, at the same time, an expandable wire mesh tube (stent) is implanted to keep the vessel open. The procedure is performed percutaneously and (biplane) X-ray imaging is applied to visualize the vessels and equipment. Due to the projective nature of X-ray imaging, the cardiologist needs to make a mental picture of the actual 3D situation inside the patient.

Reduced procedural success and higher complication rates have been reported for complex vascular anatomies, bifurcating lesions and chronically totally occluded vessels (Tsuchida et al., 2007; Hoyer et al., 2005). Using additional information from a pre-operative CTA scan is potentially beneficial in these cases. A vessel roadmap from CTA can, for example, be used to magnetically steer the guidewire through difficult branching points (Ramcharitar et al., 2007, 2008, in press). Likewise, information about the composition of the plaque, such as the location of calcium inside the lesion, may be useful when crossing chronic total occlusions, especially when applying radio frequency or laser ablation.

To be able to use the additional information from CTA, accurate alignment of the preoperative image with the intraoperative situation is essential. This alignment is often determined automatically using 3D/2D registration. An extensive overview of 3D/2D registration approaches is given in the work of Markelj et al. (in press); here we focus specifically on vascular applications.

Most work in this area is on neurological applications, where the vasculature can be considered as static (e.g. Bullitt et al., 1999; Groher et al., 2007; Hipwell et al., 2003; McLaughlin et al., 2005). A small amount of work was presented on the alignment of preoperative cardiac data to intraoperative 2D imaging modalities. Imamura et al. (2002) rigidly register 3D CTA to 2D X-ray images to guide endovascular stent grafting. In the work of Chen et al. (2007), CT scans are rigidly registered to dual-energy digital radiography to evaluate the applicability of this modality for calcium detection. Only a few studies have been dedicated to 3D/2D coronary artery registration. Turgeon et al. (2005) proposed a static registration technique to align rotational angiography data to intraoperative X-ray angiography. Their approach is based on segmentation of the coronary arteries from the preoperative imaging data and comparison of the intraoperative angiography images with projections of the resulting coronary model. The method was evaluated in a simulation study using both mono- and biplane X-ray data. Another ap-

proach based on segmentation of the 3D data was proposed by Ruijters et al. (2009). This method employs vessel enhancement filtering on the 2D X-ray images to generate a fuzzy segmentation of the coronary arteries. They show that this approach, together with a stochastic optimization procedure, leads to more robust registration results.

In previous work, we also performed static ECG-gated registration of the coronary arteries using an intensity based approach (Metz et al., 2009b). The disadvantage of static approaches is that information from the CTA data can only be used at the time point in the cardiac cycle at which the registration was performed, whereas one would preferably have access to this information for the complete cardiac cycle. We therefore investigated the derivation of coronary motion models from 4D CTA data to apply for dynamic registration of CTA and X-ray angiography (Metz et al., 2009a). A similar dynamic approach was used by Figl et al. (2010) to guide robotic minimally invasive bypass surgery. They register 4D coronary CTA images to stereo endoscopic images using a photo-consistency measure. Derivation of heart motion from CTA and MRA was performed before, for example by Wierzbicki et al. (2004), but their focus was only on the big cardiac structures. For coronary motion estimation from CTA, Laguitton et al. (2006) proposed a technique to track the coronary arteries in time by comparison of local image based features. In the work of Yang et al. (2010) coronary centerline trees are first extracted in all phases of the 4D CTA data and subsequently motion estimation is performed by a point matching algorithm. Lastly, Zhang et al. (2010b,c,a) presented different approaches based on image registration and local tracking methods to estimate coronary motion.

Another application of 3D/2D registration concerns the vasculature of the liver (Jomier et al., 2006; Groher et al., 2007; Zikic et al., 2008; Groher et al., 2009). Especially the work by Zikic et al. (2008) and Groher et al. (2009, 2010) is of interest as they propose a registration method that incorporates nonrigid deformation due to respiratory motion. As the coronary arteries are also affected by the cardiac motion, we expect their motion to be faster and the nonrigid motion component to be larger. Introducing knowledge about the coronary motion derived from preoperative imaging data may therefore be beneficial.

In this chapter we investigate the feasibility of a 3D+t/2D+t registration approach for aligning preoperative 4D coronary CTA with intraoperative X-ray angiography. The method depends on extraction of a patient specific coronary motion model, which is subsequently aligned with the intraoperative X-ray images. Motion modeling is performed from 4D CTA by centerline extraction at the end-diastolic time point and motion estimation by image registration. Alignment of the model with the X-ray data is performed for multiple time points simultaneously.

6.2 Method

Registration of coronary CTA and X-ray angiography is a challenging task due to the complex combination of different sources of misalignment. We consider transformations caused by the following elements:

- (i) **Patient pose:** the position and orientation of the patient with respect to the imaging coordinate system preoperatively differs from the situation intraoperatively. For

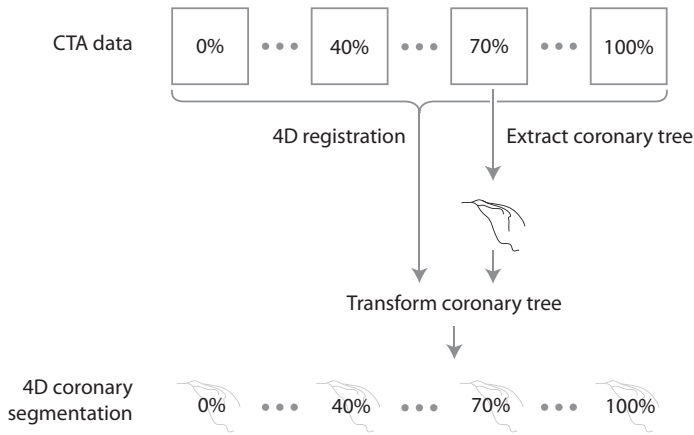


Figure 6.1: Dynamic segmentation from 4D CTA: centerlines are extracted from the end-diastolic time point and propagated to the other time points using the result of a 4D registration procedure.

example, the height of the table with respect to the isocenter of the imaging system and the position and orientation of the patient on the table are different.

- (ii) **Cardiac cycle:** the contraction and expansion of the heart muscle causes the coronary arteries to deform nonrigidly.
- (iii) **Respiratory cycle:** the heart also moves due to breathing motion. This motion is mainly in the inferior-posterior direction, but movement in the other directions and rotation of the heart have been reported as well (Shechter et al., 2004, 2006). Moreover, it has also been shown that small nonrigid deformations of the heart take place during the respiratory cycle (Shechter et al., 2004).

We base our approach on creating a patient specific 4D coronary model that captures the motion of the cardiac cycle (Section 6.2.1). This 4D coronary model is then matched temporally to the intraoperative situation, after which the spatial alignment takes place via a 3D+t/2D+t registration procedure (Section 6.2.2). Motion due to the respiration is assumed to be mainly rigid, allowing us to include it in the optimization of the position and orientation of the preoperative image.

6.2.1 4D coronary modeling

The patient specific 4D coronary models are derived from 4D CTA by segmentation and motion estimation. 4D CTA data is reconstructed at regular intervals, capturing the shape of the coronary arteries at different temporal positions in the RR-interval. Our approach consists of extracting the shape of the coronary arteries at the end-diastolic time point and their motion from the complete image sequence. By combining these two, a 4D coronary model is derived (Figure 6.1).

For the segmentation at the end-diastolic time point, the user has to manually annotate the start and end points of the vessels. These points are used as initialization of the centerline extraction method presented in Chapter 2 using the vesselness/intensity cost function. In case of failure, one extra point along the vessel is annotated and used as an intermediate point in the extraction process. The resulting centerlines are used to initialize the segmentation method presented in Schaap (2010, Chapter 5) to automatically find the arterial lumina. From the segmentations, we then derive more accurate centerlines (see Schaap, 2010, Section 5.3.5). Motion estimation is performed by application of the registration method described in Chapter 4 on the 4D CTA data. Parameter settings used are outlined in Chapter 5. The resulting transformation is applied to propagate the centerlines to the complete cardiac cycle. We denote the 4D centerline model with $Q = \{Q_t \mid 0 \leq t \leq 1\}$, where Q_t is the set of centerlines at time point t .

6.2.2 Alignment of 4D coronary model to X-ray sequence

We model the alignment of the 4D coronary model with the interventional situation by two separate transformations. The first transformation $T_{\mu}^{\text{temp}}(t)$ maps a time point $0 \leq t \leq 1$ from the 4D coronary model to the corresponding time point in the X-ray sequence. The second transformation $T_{\nu}^{\text{spat}}(\mathbf{x}, t)$ takes care of the position and orientation of the model at X-ray time point t and maps a coordinate $\mathbf{x} \in \mathbb{R}^3$ from the 4D coronary model to the coordinate system of the intraoperative imaging system. The vectors μ and ν hold the parameter values of the respective transformations.

Temporal alignment and T_{μ}^{temp}

Temporal alignment is performed to account for different heart rates during CTA acquisition and intervention. We estimate a transformation $T_{\mu}^{\text{temp}}(t)$ to map temporal positions of the 4D coronary model to corresponding temporal positions in the X-ray sequence. As the cardiac cycle non-linearly relates to the heart rate (Bazett, 1920), we define $T_{\mu}^{\text{temp}}(t)$ to be a third order polynomial:

$$T_{\mu}^{\text{temp}}(t) = at^3 + bt^2 + ct + d. \quad (6.1)$$

Furthermore, we only allow an ascending T_{μ}^{temp} and we keep the R-peak at a fixed location:

$$T_{\mu}^{\text{temp}}(0) = 0 \quad (6.2)$$

$$T_{\mu}^{\text{temp}}(1) = 1, \quad (6.3)$$

reducing the number of parameters in μ to be estimated to two. An example of a transformation is shown in Figure 6.2(a).

Parameter vector μ contains the mapped values $T_{\mu}^{\text{temp}}(t)$ for temporal positions $t = 1/3$ and $t = 2/3$. Optimization is performed by searching exhaustively for the mapped values that maximize the normalized cross correlation between the deformed ECG curve of the CTA acquisition and the ECG curve of one cardiac cycle during the intervention, while taking into account that $T_{\mu}^{\text{temp}}(1/3) < T_{\mu}^{\text{temp}}(2/3)$. To deform the ECG

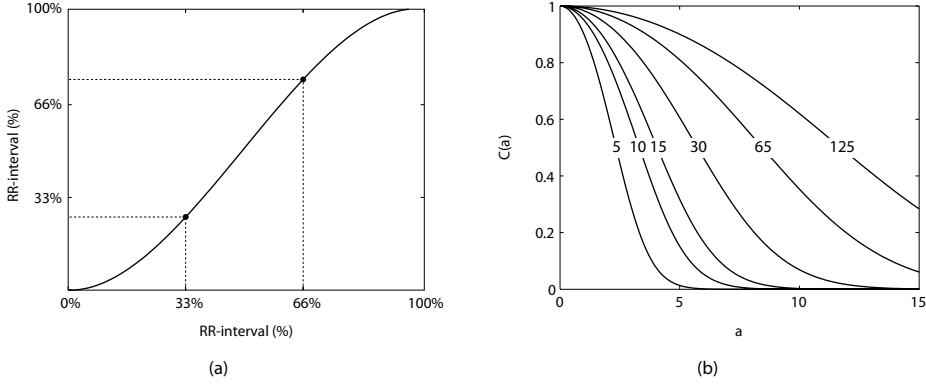


Figure 6.2: (a) Example of temporal alignment transformation. A third order polynomial is used to describe the transformation and the R-peak position is kept constant. (b) Examples of $g(a, g_a)$ for different values of g_a (indicated on the lines of the graph).

signal corresponding to the 4D coronary model, we determine the inverse of Equation 6.1. Resulting transformations allow for local temporal contraction or expansion of the ECG signal. This ECG alignment step is identical to one step of the iterative procedure described in Section 5.2.3 for the alignment of left ventricular volume curves.

The ECG signals used in the alignment are extracted from the DICOM tags of the imaging data. As the CTA data is acquired during multiple cardiac cycles, the ECG signals that are recorded during the CTA acquisition are averaged. This is achieved by first finding the locations of the R-peaks and detecting irregular heart beats using the Modular ECG Analysis System (MEANS) (van Bommel et al., 1990) and subsequently averaging of the ECG signals of the regular heartbeats. Assuming that the variances in the heart rate during the CTA acquisition are low, we linearly scale the separate ECG signals to align the R-peaks before averaging. For the X-ray angiography images, R-peaks are detected in the same way, but in this case we just select one cycle from the sequence for both the temporal and spatial alignment.

After ECG alignment we resample our 4D coronary model at the time point positions of the X-ray sequence using $T_{\mu}^{\text{temp}}(t)$. To this end we invert Equation 6.1 and derive non-integer time point positions of the 4D coronary model by spline interpolation. We denote the temporally aligned model with $Q^* = \{Q_t^* | 0 \leq t \leq 1\}$, where Q_t^* is the 3D coronary model at X-ray time point position t .

Spatial alignment and T_v^{spat}

The second transformation $T_v^{\text{spat}}(\mathbf{x}, t)$ describes the spatial alignment of coronary model Q_t^* with the intraoperative situation at X-ray time point position t . In this registration procedure, we employ information from multiple time points in a temporal window W simultaneously, thereby adding as much information as possible to the registration problem (Figure 6.3). We also take into account heart motion over time due to respiration

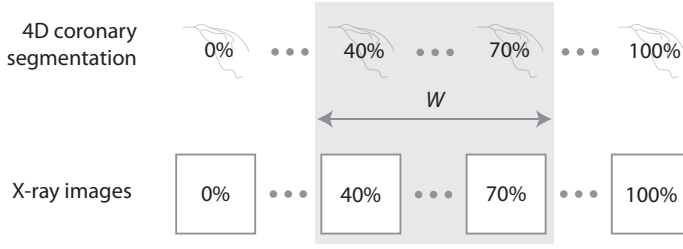


Figure 6.3: Registration is performed for $|W|$ X-ray images simultaneously adding as much information to the registration as possible. In this image we assume that the sequences have been temporally aligned.

by defining a rigid transformation for both the start and end point of this temporal window. The rotation and translation of the model at intermediate time points are obtained by spherical linear interpolation (Shoemake, 1985) and linear interpolation respectively. This approach results in twelve degrees of freedom to be determined: six rotations and six translations. Three rotations and three translations for the start of the temporal window and three rotations and three translations for the end of the temporal window.

The spatial transformation $T_v^{\text{spat}}(\mathbf{x}, t)$ is therefore defined as:

$$T_v^{\text{spat}}(\mathbf{x}, t) = \mathbf{R}_v(t) \mathbf{x} + \mathbf{m}_v(t) \quad (6.4)$$

with $\mathbf{R}_v(t)$ a rotation matrix derived from the three rotation angles at time point t and $\mathbf{m}_v(t)$ the translation vector at time point t . For convenience in the initialization procedure, we define the translation parameters orthogonal to and along the projection direction. The translation vector is therefore defined as:

$$\mathbf{m}_v(t) = x_t \mathbf{q}_x + y_t \mathbf{q}_y + z_t \mathbf{q}_z, \quad (6.5)$$

with $\|\mathbf{q}_x\| = 1$, $\|\mathbf{q}_y\| = 1$ and $\|\mathbf{q}_z\| = 1$ the vectors perpendicular to and in the direction of the projection directions (Figure 6.4) and x_t , y_t and z_t the translation parameter values at time point t derived from \mathbf{v} . Rotations are defined around the main axis of the imaging system's coordinate system (Figure 6.4).

The quality of the fit is measured by a similarity metric $S(\mathbf{v})$ and based on fuzzy segmentation of the X-ray images and distance transforms of the projected 4D centerline model Q^* , inspired by the work of Ruijters et al. (2009). Let us denote with \mathbf{P} the perspective projection matrix describing the geometry of the imaging system and with Ω_t the 2D image domain of the X-ray image at time point t . Furthermore, we define a function $D(\mathbf{y}, Y)$, which returns the closest distance of voxel \mathbf{y} to the set of 2D centerlines Y . The similarity metric is then defined as:

$$S(\mathbf{v}) = \sum_{t \in W} \sum_{\mathbf{y} \in \Omega_t} g\left(D\left(\mathbf{y}, \mathbf{P} T_v^{\text{spat}}\left(Q_t^*, t\right)\right)\right) F(\mathbf{y}, t). \quad (6.6)$$

The function $g(a)$ controls the neighborhood of the projected centerlines taken into account and equals one when a is zero and decreases with increasing a :

$$g(a) = 2 - \frac{2}{1 + \exp(-a^2/g_a)} \quad (6.7)$$

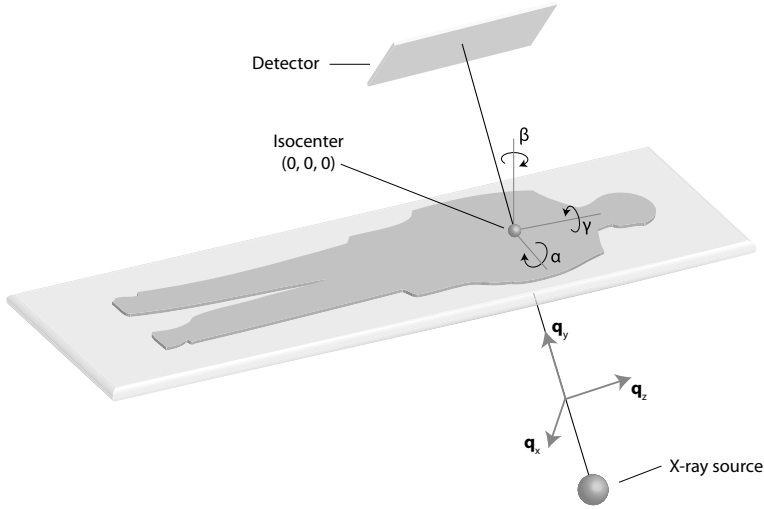


Figure 6.4: Overview of the parameters that need to be determined in the spatial registration step. Note that the axes of the translation parameters are shifted along the projection direction for visualization purposes; the origin is at the isocenter of the imaging system. The three translation directions (q_x , q_y , q_z) are defined perpendicular to and along the projection direction. Rotations α , β , γ are defined with respect to the patient coordinate system.

with g_a a parameter controlling the steepness of the function (see Fig. 6.2(b) for examples). $F(y, t)$ denotes the fuzzy segmentation of the X-ray image at time point t taking values between zero and one. We apply a multiscale vesseness filter on the input images (Frangi et al., 1998) to obtain this fuzzy segmentation. The differences between our metric and the metric proposed by Ruijters et al. (2009) are the use of temporal window W and a smooth function to transform the squared distance transform values.

The optimization procedure consists of finding a set of parameters that maximizes the similarity metric:

$$\hat{\nu} = \operatorname{argmax}_{\nu} S(\nu) \quad (6.8)$$

We use a nonlinear conjugate gradient optimizer (Dai, 2001; Klein et al., 2007) and derive the derivative of our metric using finite differences. Furthermore, we apply a multi-resolution approach in which parameter g_a is lowered to half its value after each resolution step. Parameter scaling is performed to ensure a good behaviour of the optimizer. To this end, we set the scales in such a way that one degree of rotation corresponds to one millimeter translation. Initialization of the model is performed by first moving the center of gravity of Q_t^* to the origin of the intraoperative coordinate system and subsequent manual initialization of x_t and z_t (Equation 6.5) while observing only the X-ray image at the center of the temporal window. Start and end translation for the window are thus initially equal. All remaining parameters are initially set to zero.

Table 6.1: Patient and intervention characteristics. Listed are which coronary tree is involved (L=left, R=right), the frame-rate of the X-ray acquisition, the number of X-ray images of the cycle on which the registration is performed, the heart rate (HR) of the patient during the CTA acquisition and intervention, and the number of days between CTA acquisition and intervention.

Patient	1	2	3-1	3-2	4-1	4-2	5	6	7	8	9	10
Tree	R	L	L	L	R	R	L	L	L	R	L	R
Interval (days)	5	14	46	177	4	77	161	149	50	15	66	10
X-ray data												
Framerate (fps)	15	15	15	15	15	15	30	15	15	15	15	15
# frames cycle	12	18	12	11	12	13	21	11	9	12	13	10
Heart rate (bpm)												
CTA	69	60	91	91	77	77	71	53	135	78	54	78
X-ray	75	50	75	82	75	69	86	82	100	75	69	90

6.3 Experiments and results

6.3.1 Imaging data

We collected thirteen X-ray angiography sequences of eleven patients for which also retrospectively ECG gated 4D CTA images were available. The X-ray images of the two patients for which multiple sequences were collected were from different intervention dates. One of the patients was excluded, because the 4D segmentation failed due to streaking artifacts caused by a pacemaker. The experiments were thus performed on twelve datasets of 10 patients. Patient and intervention information such as the coronary tree involved, the heart rate of the patient and the interval between the CTA and X-ray acquisition are listed in Table 6.1.

X-ray images were acquired using a Siemens Axiom Artis biplane system, but as no calibration data was available, only monoplane experiments using the sequences of the primary C-arm are considered. Acquisition took place between August 2007 and November 2009. The size of the X-ray images was 512x512 voxels with a voxel size of approximately 0.22x0.22 mm². From every X-ray sequence we selected one contrast enhanced cardiac cycle to be used in the experiments.

CTA images were acquired using a Siemens Definition or Siemens Definition Flash scanner. Reconstructions were made at every 5% of the cardiac cycle, resulting in 20 3D images per sequence. The field of view used for the reconstruction was 256x256 voxels and the resulting voxel size was approximately 0.7x0.7x0.9 mm³. The average number of slices was 140. The slice thickness was 1.5 mm. Histogram equalization was performed on the CTA images, because a preliminary study revealed a positive effect on the 4D registration results. On the X-ray sequences a very basic background subtraction was performed by subtracting from every voxel value the median intensity value over time.

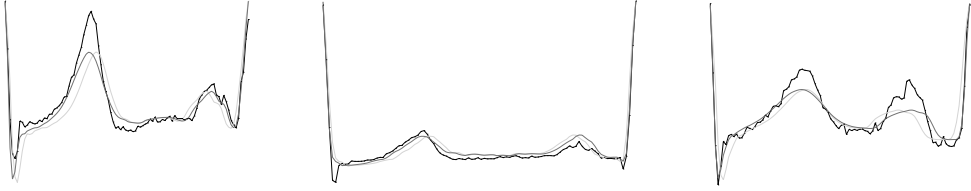


Figure 6.5: Examples of ECG signals used in the temporal alignment. Black line: reference ECG of a cardiac cycle from the X-ray sequence. Light grey: CTA ECG signal before alignment. Dark grey: CTA ECG signal after alignment.

6.3.2 Evaluation of registration

Temporal alignment

Before spatial registration, the 4D coronary model is aligned temporally with the X-ray sequence as described in Section 6.2.2. Inspection of the ECG alignment revealed that for some patients the shape of the ECG from the CTA acquisition and the intervention differs. Only for case 8 this caused the ECG alignment to fail completely, resulting in an incorrect resampling of the 4D coronary model. Three examples of the ECG alignment are shown in Figure 6.5.

Spatial alignment and evaluation methodology

After temporal alignment and manual initialization, we performed the spatial alignment of the 4D coronary model with the interventional situation as described in Section 6.2.2.

The following parameters were set empirically: the maximum number of iterations for the conjugate gradient optimizer to 100, the maximum number of iterations for the internal line search optimizer to 20, the number of resolution levels to four and the value of g_a in the coarsest level to 1000. Three scales were used for the vesselness filter: 0.8, 1.3 and 2 mm.

For evaluation purposes, we manually annotated the vessels included in the 4D coronary model in every X-ray image of the sequence. See Figure 6.6 for examples of these annotations. To measure the quality of the registration we compute for every point along an annotated centerline segment the closest distance to a corresponding projected centerline and report the average and standard deviation of these distance values. Correspondence between the projected and annotated centerlines is determined by searching for every annotated 2D centerline segment the projected centerline that is on average closest.

Experiment 1: registration accuracy

In the first experiment, we evaluate the registration performance of the presented method. The window W is set to cover the entire cardiac cycle. Table 6.2 shows the resulting centerline distances.

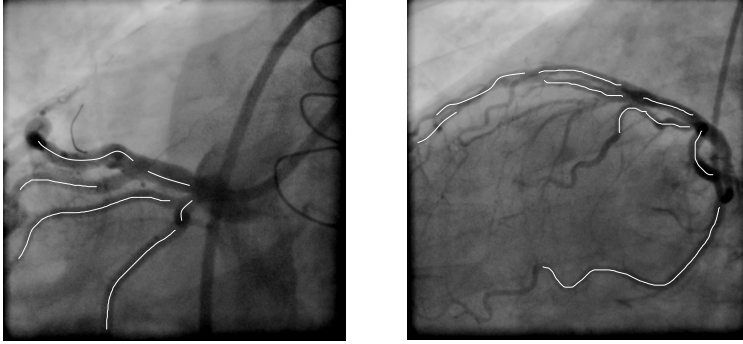


Figure 6.6: Examples of manual annotations overlaid in white on the corresponding X-ray image.

Table 6.2: Average centerline distance in mm before and after registration. The second column indicates the coronary tree involved.

Patient	Tree	Before	After
1	Right	3.9 ± 3.5	1.7 ± 1.3
2	Left	1.9 ± 1.4	1.4 ± 1.1
3-1	Left	4.8 ± 3.7	2.8 ± 2.8
3-2	Left	3.1 ± 2.1	1.3 ± 1.0
4-1	Right	5.2 ± 4.7	2.8 ± 2.1
4-2	Right	6.4 ± 4.0	1.8 ± 1.4
5	Left	3.7 ± 2.7	1.4 ± 1.2
6	Left	3.9 ± 3.2	2.5 ± 2.5
7	Left	2.9 ± 2.1	2.4 ± 2.2
8	Right	4.2 ± 2.8	3.0 ± 3.0
9	Left	2.9 ± 1.9	1.3 ± 1.1
10	Right	6.2 ± 5.9	5.1 ± 5.8

Figure 6.7 shows for four cases the average and standard deviation of the distance values over time. In case 10 registration failed completely. For the other three cases shown, it can be noticed that both the mean and standard deviation of the distance values decreases considerably with respect to the manual initialization.

Figure 6.8 and 6.9 show for four cases and multiple time points the coronary center-lines projected onto the corresponding X-ray image before and after registration.

Experiment 2: effect of initialization

To investigate the effect of the initialization on the outcome of the registration, in the second experiment we performed 10 additional registrations per data set using different initializations. The initializations were randomly generated near the manual initializa-

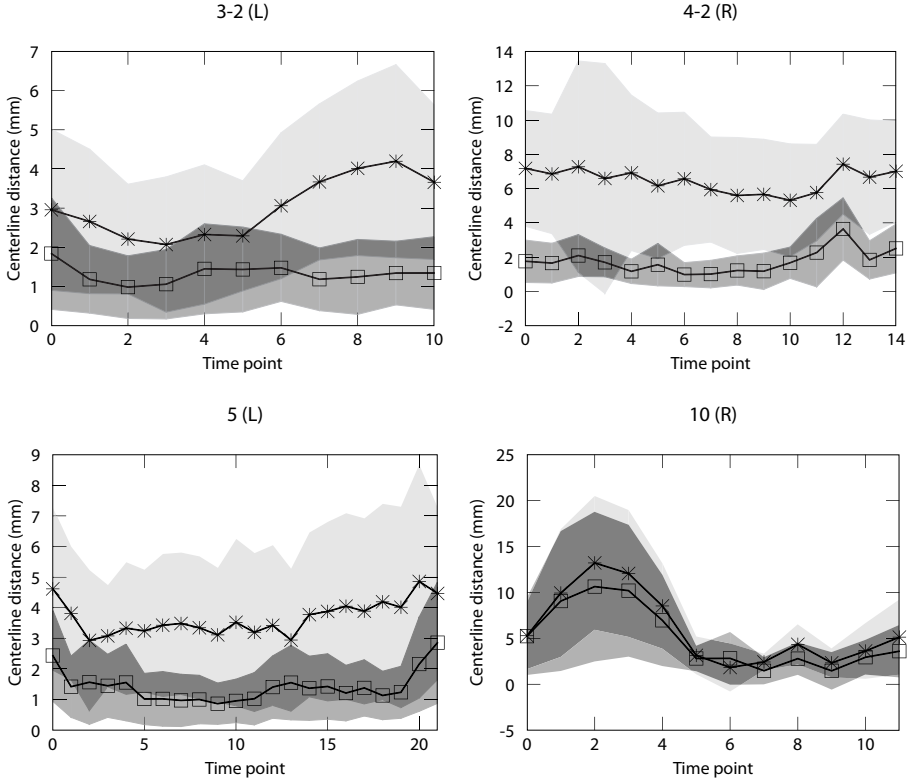


Figure 6.7: Accuracy over time for four cases. Asterisks (light grey): mean (standard deviation) of 2D centerline distance values before registration (after initialization). Boxes (dark grey): mean (standard deviation) of 2D centerline distance values after registration. The title of the plots shows the patient number and tree involved (L=left, R=right).

tion as follows. Given the initialization values used in experiment 1, all 12 parameters were perturbed with a random value in the range of $[-5^\circ, 5^\circ]$ and $[-3 \text{ mm}, 3 \text{ mm}]$ while keeping corresponding parameters for the start and the end of the temporal window equal. Registration was performed using a temporal window covering the complete cardiac cycle. Figure 6.10 shows the resulting values for the parameters. Per patient both the parameter for the start (left) and end (right) of the temporal window are shown. Furthermore, per patient we indicated if registration involved the left (L) or right (R) coronary tree. For visualization purposes we mean-centered the parameter values, which means that we subtract from every value the per-patient average of that parameter. It can be noticed that for the datasets having the worst accuracy (compare Table 6.2), variation in the parameter values is largest. Furthermore, it can be noticed that the variance of translation parameter y is relatively large. This parameter reflects the translation in the direction of the projection direction, which has less influence on the appearance of the projected model than the other parameters.

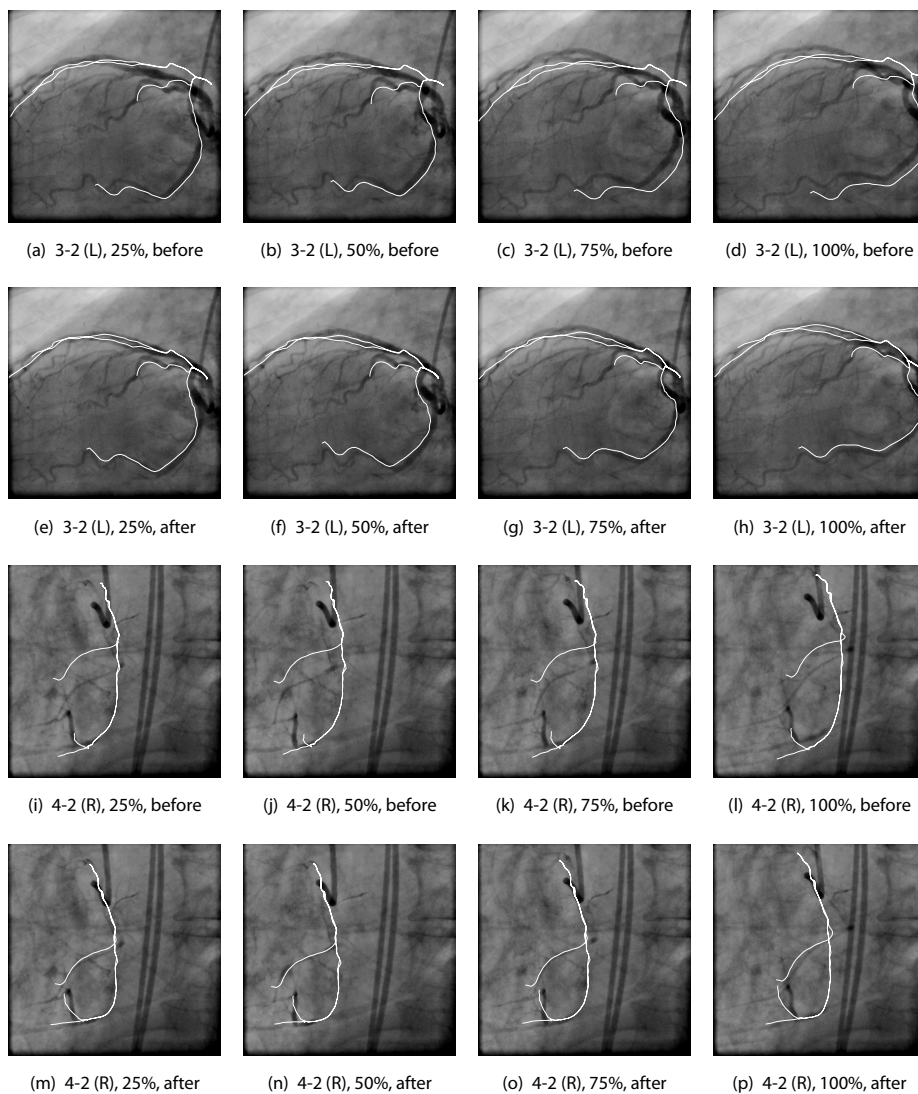


Figure 6.8: Results of the registration. Projected centerlines from the 4D coronary model before (a)-(d), (i)-(l) and after (e)-(h), (m)-(p) registration are overlaid in white. Captions indicate the patient number, the tree involved (L=left, R=right) and the percentage of the RR-interval at which the image was made.

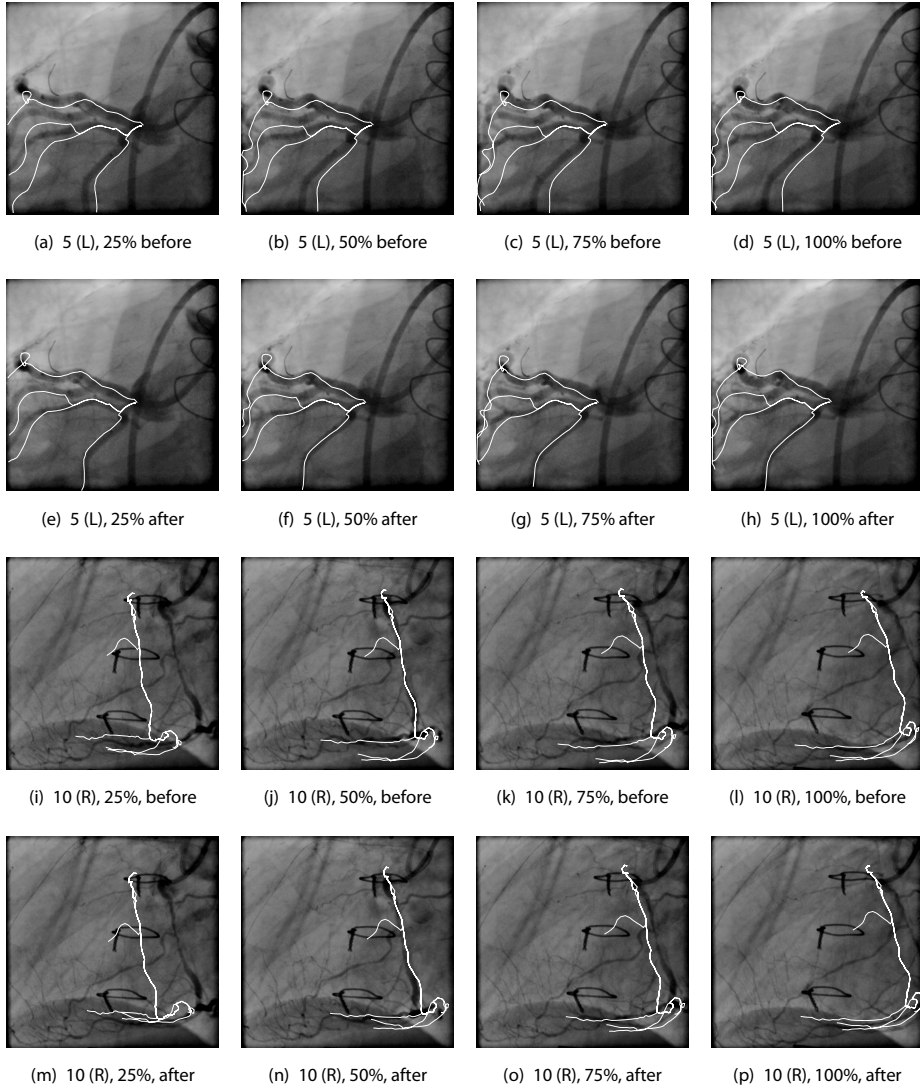


Figure 6.9: Results of the registration (continued). Projected centerlines from the 4D coronary model before (a)-(d), (i)-(l) and after (e)-(h), (m)-(p) registration are overlaid in white. Captions indicate the patient number, the tree involved (L=left, R=right) and the percentage of the RR-interval at which the image was made.

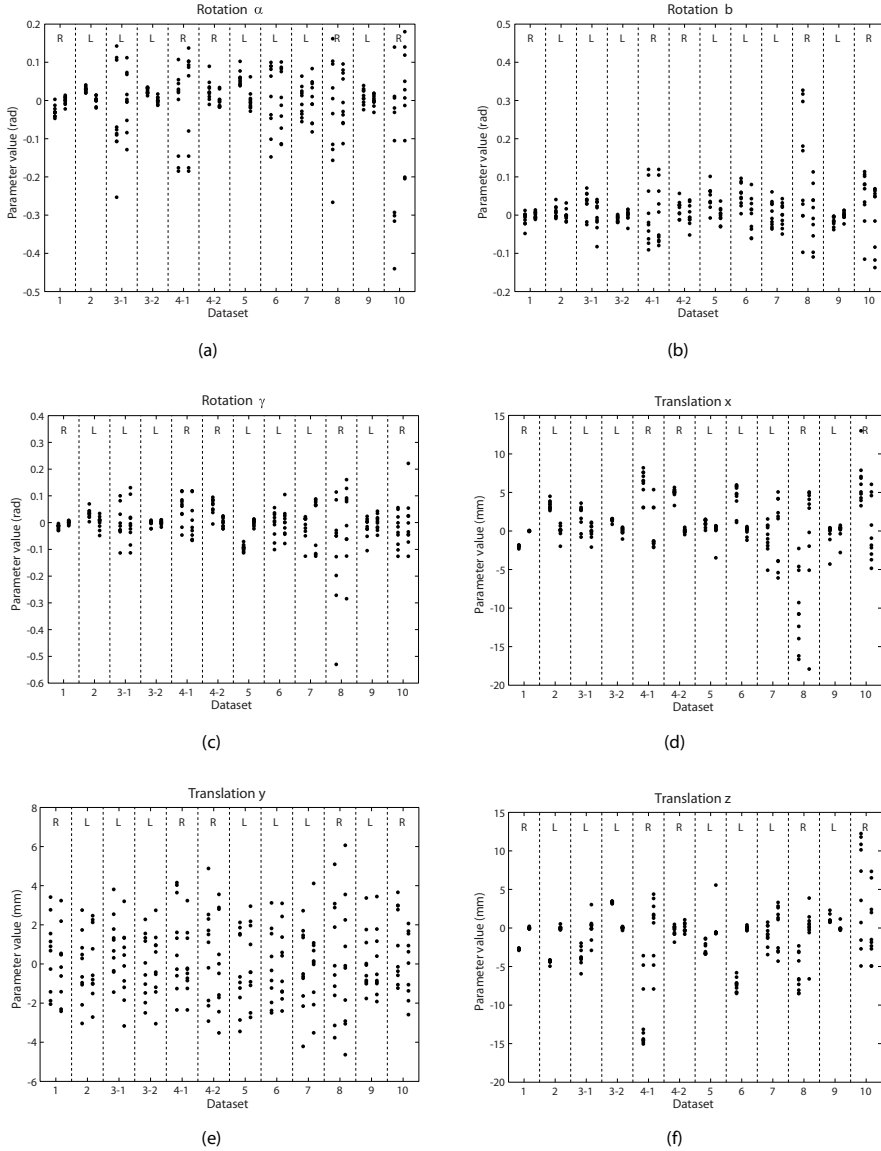


Figure 6.10: Parameters resulting from registration using different initializations. The parameter values are centered around their per-patient mean. Per patient both the parameter for the start (left) and end (right) of the temporal window is given. Furthermore, it is indicated if registration involved the right (R) or left (L) coronary tree.



Experiment 3: comparison of 3D+t/2D+t and 3D/2D registration

In the last experiment we performed additional registrations in which the width of the temporal window was set to one time point, thus performing a normal 3D/2D registration. To this end, the 10 initializations per dataset from experiment 2 were used. Evaluation was performed for both the 3D+t/2D+t and the 3D/2D approach on the initialization time point only.

Results are shown in Figure 6.11. The accuracy of the registration is shown in Figure 6.11(a) where every dot represents one registration result. Black dots represent the 3D+t/2D+t method in which the complete cardiac cycle was used for registration and grey dots the 3D/2D method where only the initialization time point was used in the registration. For every patient the tree involved (L=left, R=right) is indicated. The variance of the accuracy is in nine of the 12 cases smaller for the 3D+t/2D+t method than for the 3D/2D method. In some cases (e.g. case 4-2) the 3D+t/2D+t is able to align the model to the X-ray data whereas the 3D/2D method failed. However, it can also be noticed that in some cases the accuracy is better for the 3D/2D method. This may be explained by the fact that only the position and orientation of the model for the initialization time point needs to be optimized whereas for the 3D+t/2D+t method the other time points are taken into account as well. The method therefore finds those parameters that give on average the best fit. Figure 6.11(b) shows a boxplot of the differences between the 3D/2D method and the 3D+t/2D+t method. To this end, we first compute the per-patient mean and standard deviation over all initializations. We then compute the difference between the means and standard deviations of both methods and create the boxplot from these differences. We also performed a Wilcoxon test on these 12 difference values which showed that they are not significantly different. This might be caused by the small number of samples used to perform the test and the fact that the results in cases where both methods fail are quite random. The figures show however that there is a small trend to better average results and that the standard deviation is lower in the majority of cases.

6.4 Discussion

In this chapter we investigated the alignment of preoperative 4D coronary CTA data with intraoperative X-ray angiography using 4D models describing coronary geometry and motion. We showed that this approach is able to substantially improve over an initial alignment derived from the C-arm configuration and a subsequent manual translation of the model. Furthermore, we observed that the proposed 3D+t/2D+t approach could find a correct alignment in some of the cases where the 3D/2D approach failed. We also showed that for nine of the 12 cases 3D+t/2D+t registration is more robust to initialization than 3D/2D registration.

Although we showed the feasibility of the proposed approach, there were still some cases in which registration failed or delivered suboptimal results. There are different possible causes for these errors.

In the first place, there may be errors in the CTA-derived 4D coronary models. Very diseased vessels could disturb the results of the centerline extraction and lumen seg-

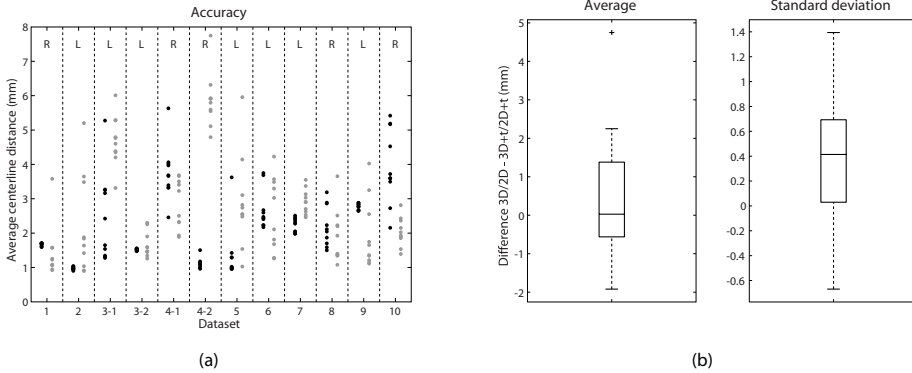


Figure 6.11: Comparison between 3D+t/2D+t and 3D/2D registration. (a) Accuracy results for both methods. Black dots represent 3D+t/2D+t registration results, grey dots 3D/2D results. In every column the coronary tree involved is indicated (L=left, R=right). (b) A boxplot of the differences between the per-patient average and standard deviation of accuracy values.

mentation. Furthermore, accurately aligning the relatively small coronary arteries using image registration is very challenging and small errors in the motion estimates are therefore likely (and in fact have been observed for our data). Also, X-ray images can be considered as real-time snapshots of the vasculature at a certain cardiac phase whereas the time point images of the 4D CTA are effectively an average over a temporal window, in our case comprising 5% of the cardiac cycle.

Another factor contributing to the difference between the 4D coronary model and the actual situation may be that even with an identical ECG signal cardiac motion may be different. In addition, patient stress and the presence of instruments inside the coronary arteries may alter coronary shape and motion. Also, coronary anatomy and motion can change between the CTA acquisition and the intervention due to disease progression. This can especially be a factor when the time between the CTA acquisition and intervention is relatively large, such as in case 3-2, 5 and 6. Differences in heart rate might also contribute to different motion patterns. Lastly, the breathing motion is known to cause small nonrigid deformations of the coronary arteries as well. In this work, we only took rigid breathing motion into account.

In the second step of our method, the 4D coronary model is temporally related to the intraoperative situation by ECG-alignment. For some patients, differences between the shape of the ECG signal of the CTA acquisition and the intervention were observed. For case 8, this resulted in complete failure of the temporal alignment. For some other cases, this introduced small deviations in the temporal alignment. Furthermore, when the ECG signal is relatively flat, alignment will mainly depend on the R-peaks and may be less reliable at intermediate locations.

In the spatial alignment of the method, a 3D+t/2D+t registration approach is used in which the similarity metric is based on fuzzy segmentation of the coronary arteries. This segmentation includes false positive responses which could disturb the regis-



tration. The catheter is, for example, often visible in the X-ray images and results in very large responses of the vesselness filter due to its tubular shape and contrast. Furthermore, multiple vessels may project on top of each other in the X-ray images which decreases the amount of valuable information that can be used by the registration algorithm. Next to over-projection, the method does not take a per vessel correspondence between the 4D coronary model and the 2D fuzzy segmentation into account. Aligning non-corresponding vessels could therefore result in relatively high similarity metric values and consequently local maxima in the optimization landscape.

There is much potential for improving the method. The use of biplane data is expected to improve the spatial optimization procedure, overcoming issues due to over-projection and correspondence free registration. The availability of accurate calibration data for these biplane acquisitions is a prerequisite for this. The fuzzy segmentation of the X-ray angiography images could be improved by preventing non-vessel objects to appear in the segmentation results.

Differences between the preoperative 4D coronary model and the intraoperative situation, e.g. due to the presence of instruments in the vessels and breathing induced nonrigid motion, can potentially be dealt with by applying a nonrigid registration approach such as proposed by Zikic et al. (2008) and Groher et al. (2009, 2010) in which every vessel of the coronary model is separately aligned nonrigidly to the intraoperative situation.

An alternative for the temporal alignment based on ECG signals is to optimize the value of the two temporal parameters simultaneously with the spatial parameters. The temporal alignment is then driven by the same similarity metric as the spatial alignment eliminating the need for using ECG signals, which might have a different shape between CTA and X-ray acquisition and can be disturbed by noise.

6.5 Conclusion

We investigated the feasibility of a 3D+t/2D+t registration approach to align preoperative CTA and intraoperative X-ray angiography data. It was shown that this approach has advantages over the more classic 3D/2D approach in terms of registration success and reproducibility. Even though there is room for improvement with respect to registration success and accuracy, our experiments show the potential of the proposed methodology.

A series of thin, white, wavy lines that flow from the top left towards the bottom right, creating a sense of movement and depth against the light gray background.

7

Summary and Future Perspectives



7.1 Summary

In this thesis we described the development and evaluation of techniques to align preoperative coronary CTA data with intraoperative X-ray angiography. We proposed a strategy based on patient specific modeling of coronary artery geometry, motion, and deformation. These coronary models were derived from 4D cardiac CTA by extracting their shape at the end-diastolic phase of the cardiac cycle and estimating their motion and deformation by image registration. Subsequently, the models were aligned to the intraoperative X-ray images employing information from multiple time points simultaneously.

In the first chapters we presented techniques to create the patient specific 4D coronary models. We described in **Chapter 2** the application and evaluation of a minimum cost path approach for coronary centerline extraction from 3D CTA. Quantitative evaluation on 48 coronary arteries showed a success rate of 88% and accuracy of 0.64 mm. Additional experiments showed successful centerline extraction for 233 out of the 252 evaluated coronary arteries (92%) in 63 additional CTA images.

Next to our work on coronary centerline extraction, several other methods for this purpose have been proposed in literature. However, as no standardized evaluation methodology was available, the reliable evaluation and comparison of the performance of these existing and newly developed methods was difficult. In **Chapter 3**, we described the development of a standardized evaluation methodology and reference database for the quantitative evaluation of coronary artery centerline extraction algorithms. This framework consists of a publicly available database with thirty-two CTA images, a reference standard derived from manual annotations and well-defined evaluation measures. The applicability of the framework was shown by evaluating and comparing thirteen coronary artery centerline extraction algorithms, implemented by different research groups. Currently, the framework has over 100 subscriptions and its use is required for publishing results in high quality medical imaging journals.

By application of the method described in **Chapter 2** or one of the methods evaluated in **Chapter 3** a static segmentation of the coronary tree can be derived, for example, at the end-diastolic phase of the cardiac cycle. However, to create a coronary model over the complete cardiac cycle, the motion and deformation of the arteries needs to be known as well. In this work, this is estimated by means of image registration. In **Chapter 4** we proposed a method for motion estimation in dynamic medical imaging data. The method performs a groupwise registration, thus avoiding a bias towards a specifically chosen reference time point. Furthermore, it takes both spatial and temporal smoothness of the transformations into account and is able to enforce cyclic motion. The method is based on a 3D (2D+time) or 4D (3D+time) free-form B-spline deformation model, a similarity metric that minimizes the intensity variances over time and constrained optimization using a stochastic gradient descent method with adaptive step size estimation. Quantitative evaluation showed subvoxel accuracy and high consistency of the registration results.

If dynamic imaging data is available, combining a static coronary segmentation and a motion estimate derived by image registration is a reasonable approach to create 4D coronary models. However, the increase in radiation dose associated with these dynamic acquisitions is not always justifiable. Prospective electrocardiogram gating is therefore increasingly applied to reduce the patient radiation dose, often limiting reconstruction

to a single 3D image. In **Chapter 5** we therefore presented a method to predict the motion of the cardiac structures for the entire cardiac cycle from shape information of a single phase. Motion prediction was performed by principle component regression via statistical shape and motion models. Our prior hypothesis in this approach was that the motion of the heart is at least partially explained by its shape. Quantitative evaluation on 150 4D computed tomography angiography (CTA) images showed a small but statistically significant increase in the accuracy of the estimated shape sequences compared to shape-independent motion prediction.

Finally, in **Chapter 6** we investigated the feasibility of the 3D+t/2D+t registration for registering CTA data to X-ray angiography data. We applied methods from the previous chapters for patient specific 4D modeling of the coronary arteries and aligned this preoperative model temporally to the intraoperative situation by means of ECG alignment. In the last step, the temporally aligned 4D coronary model was used to perform the spatial alignment. A non-linear conjugate gradient optimizer was used to optimize a similarity metric based on centerline projection and fuzzy X-ray segmentation. This spatial alignment was simultaneously performed on multiple X-ray images within a temporal window, also taking into account rigid motion due to respiration. We evaluated the approach by comparing projected centerlines with manually annotated 2D centerlines in the X-ray images. In the experiments we showed that the proposed registration approach has advantages over the more classic 3D/2D approach in terms of registration success and reproducibility.

In conclusion, the proposed registration strategy based on coronary motion modeling is promising for aligning preoperative CTA to intraoperative X-ray angiography.

7.2 Future perspectives

Accurate alignment of preoperative CTA and intraoperative imaging data for PCI is very challenging due to a complicated mix of motion from different sources. In this thesis we presented several steps towards this alignment. Additional research is still needed to improve both registration success and accuracy. For the latter, demands are high as the diameter of the coronary arteries is relatively small.

The ultimate goal of the work in this thesis is the integrated visualization of preoperative imaging data and instruments during PCI interventions. This may be beneficial in difficult cases, especially for cases in which the arteries are totally occluded. Successful treatment of these chronic total occlusions depends, according to Serruys (2006), on the availability of the following techniques: remote steering of the wire, forward looking imaging techniques, such as optical coherence tomography (OCT) or intravascular ultrasound (IVUS), and application of ablative power. For the treatment of chronic total occlusions a device integrating these techniques is needed. However, for coronary interventions such a device is currently not available and several technological challenges need to be addressed before it can be realised. Integration of preoperative CTA complements these techniques, as it provides a roadmap for navigation, and may also be used to complement intracoronary imaging, as it allows the visualization of plaque further ahead. Whether the integration of CTA data will be possible with sufficient accuracy to



be used for navigating the guidewire, replacing intracoronary imaging, remains to be investigated.

In Chapter 6 we suggested several approaches to improve upon our current results. Some progress could be made in the first part of the approach to derive more accurate 4D coronary models from CTA. Next, temporal alignment on ECG data might not be optimal and may be replaced or succeeded by temporal alignment based on the imaging data. In the spatial alignment, improvements could be made in the fuzzy segmentation of the X-ray images, in which mainly excluding the catheter might be beneficial. Ambiguity introduced by the projective nature of X-ray angiography, such as multiple vessels projecting on top of each other, and limitations in the capture range could be decreased by using biplane data. Finally, differences between the preoperative model and intraoperative situation will persist due to, for example, the introduction of instruments in the vessels, progression of disease between CTA acquisition and intervention and non-rigid motion due to respiration. Per-vessel non rigid alignment of the coronary arteries may be used to solve these remaining differences (Zikic et al., 2008; Groher et al., 2009, 2010).

In future research it would also be interesting to compare alternatives for the alignment of the 4D coronary models to the intraoperative situation. One of these alternatives is to reconstruct a 4D coronary model from biplane X-ray angiography and match this model to the preoperative 4D coronary model. Another approach is to create an intraoperative dynamic coronary model from a coronary artery or vessel segment by application of a magnetic tracking device, recording world coordinate positions of the tip of the guidewire during a pull-back of the wire through the vessel of interest (Jeron et al., 2009). Such a model can then be aligned with the preoperative 4D coronary model, but this might be challenging as the intraoperative model contains smaller parts of the coronary tree and in the case of total occlusions will only include the artery proximal to the lesion.

Application of our approach in clinical practice also requires tracking of the anatomy after the initial alignment of the 4D CTA model with the X-ray angiography images. We did not address this topic, which mainly requires breathing motion compensation, in our work. The limited visibility of the cardiac structures in the X-ray images when no contrast agent is introduced makes this a challenging topic. Several approaches can be envisioned, the most straightforward would be applying a similar methodology as we did, i.e. modeling the heart motion because of breathing. Whether this approach is feasible, and whether heart motion as function of breathing state can be modeled as easily, remains to be investigated. Other approaches, such as image-based or electromagnetic tracking of the instruments (guidewires and catheters) could also be pursued. The combination of these types of approaches with the work described in this thesis would provide the technology to build a prototype cardiac image guidance system.

The techniques presented in this thesis are not only useful for the specific application of the registration of coronary CTA and X-angiography. A similar approach could, for example, be applied on respiratory gated CTA, which might be useful for radiotherapy applications. Klinder et al. (2010), for example, perform motion prediction using respiratory gated CT using a similar approach as we presented in Chapter 5.

Whereas the application of motion prediction seems to be mainly relevant in image guided interventions, the other techniques presented in this thesis do have applications

in the diagnostic field. Centerline extraction is for example useful for (semi)automated analysis of coronary CTA data. Extracted centerlines are, for example, useful for visualization purposes, such as the creation of curved planar reformatted images. They can also be used as initialization for lumen segmentation, in a first step of automated stenosis quantification. Motion estimation by image registration as presented in Chapter 4 is useful for all kinds of applications and we showed applications on various imaging modalities and anatomies.

In conclusion, in this thesis we developed and evaluated techniques which are important towards the integration of CTA imaging data during interventional cardiology procedures.



Bibliography

- Ablitt, N. A., Gao, J., Keegan, J., Stegger, L., Firmin, D. N., Yang, G.-Z., 2004. Predictive Cardiac Motion Modeling and Correction With Partial Least Squares Regression. *IEEE Trans. Med. Imaging* 23 (10), 1315–1324.
- Armato, S. G., McLennan, G., McNitt-Gray, M. F., Meyer, C. R., Yankelevitz, D., Aberle, D. R., Henschke, C. I., Hoffman, E. A., Kazerooni, E. A., MacMahon, H., Reeves, A. P., Croft, B. Y., Clarke, L. P., Group, L. I. D. C. R., 2004. Lung Image Database Consortium: Developing a Resource for the Medical Imaging Research Community. *Radiology* 232 (3), 739–748.
- Aylward, S., Bullit, E., 2002. Initialization, Noise, Singularities, and Scale in Height Ridge Traversal for Tubular Object Centerline Extraction. *IEEE Trans. Med. Imaging* 21 (2), 61–75.
- Balci, S., Golland, P., Shenton, M., Wells, W., 2007a. Free-form B-Spline Deformation Model for Groupwise Registration. In: *Proc. Stat. Regis. Workshop - Int. Conf. Med. Image Comput. Comput. Assist. Interv.* pp. 23–30.
- Balci, S., Golland, P., Wells, W., 2007b. Non-Rigid Groupwise Registration using B-Spline Deformation Model. *Insight J. - Proc. MICCAI Open Sci. Workshop*, <<http://hdl.handle.net/1926/568>>.
- Bartz, D., Lakare, S., 2005. Scaffolding-Based Segmentation of Coronary Vascular Structures. In: *Proc. Int. Workshop Vol. Graph.* pp. 47–54.
- Bauer, C., Bischof, H., 2008a. A Novel Approach for Detection of Tubular Objects and Its Application to Medical Image Analysis. In: *Proc. Deutsche Arbeitsgemeinschaft für Mustererkennung.* pp. 163–172.
- Bauer, C., Bischof, H., 2008b. Edge Based Tube Detection for Coronary Artery Centerline Extraction. *Midas J. - Proc. MICCAI Workshop - Grand Challenge Coronary Artery Tracking*, <<http://hdl.handle.net/10380/1403>>.
- Bauer, C., Bischof, H., 2008c. Extracting Curve Skeletons From Gray Value Images for Virtual Endoscopy. In: *Proc. Med. Imaging Augm. Reality. Vol. 5128 of Lect. Notes Comput. Sci.* pp. 393–402.
- Bazett, H., 1920. An Analysis of the Time Relationships of Electrocardiograms. *Heart* 7, 353–370.
- Bhatia, K. K., Hajnal, J., Hammers, A., Rueckert, D., 2007. Similarity Metrics for Groupwise Non-Rigid Registration. In: *Proc. Int. Conf. Med. Image Comput. Comput. Assist. Interv. Vol. 4792 of Lect. Notes Comput. Sci.* pp. 544–552.
- Bhatia, K. K., Hajnal, J. V., Puri, B. K., Edwards, A. D., Rueckert, D., 2004. Consistent Groupwise Non-Rigid Registration for Atlas Construction. In: *Proc. IEEE Int. Symp. Biomed. Imaging.* pp. 908–911.
- Bidaut, L. M., Vallée, J. P., 2001. Automated Registration of Dynamic MR Images for the Quantification of Myocardial Perfusion. *J. Magn. Reson. Imaging* 13 (4), 648–655.
- Bistoquet, A., Oshinski, J., Skrinjar, O., 2008. Myocardial Deformation Recovery From Cine MRI Using a Nearly Incompressible Biventricular Model. *Med. Image Anal.* 12 (1), 69–85.
- Blackall, J., King, A., Penney, G., Adam, A., Hawkes, D., 2001. A Statistical Model of Respiratory Motion and Deformation of the Liver. In: *Proc. Int. Conf. Med. Image Comput. Comput. Assist. Interv. Vol. 2208 of Lect. Notes Comput. Sci.* pp. 1338–1340.
- Boldea, V., Sharp, G. C., Jiang, S. B., Sarrut, D., 2008. 4D-CT Lung Motion Estimation With Deformable Registration: Quantification of Motion Nonlinearity and Hysteresis. *Med. Phys.* 35 (3), 1008–1018.
- Boskamp, T., Rinck, D., Link, F., Kümmerlen, B., Stamm, G., Mildenerger, P., 2004. New Vessel Analysis Tool for Morphometric Quantification and Visualization of Vessels in CT and MR Imaging Data Sets. *Radiographics* 24 (1), 287–297.



- Bouraoui, B., Ronse, C., Baruthio, J., Passat, N., Germain, P., 2008. Fully Automatic 3D Segmentation of Coronary Arteries Based on Mathematical Morphology. In: Proc. IEEE Int. Symp. Biomed. Imaging. pp. 1059–1062.
- Brown, J. R., O'Connor, G. T., 2010. Coronary Heart Disease and Prevention in the United States. *N. Engl. J. Med.* 362 (23), 2150–2153.
- Bullitt, E., Liu, A., Aylward, S. R., Coffey, C., Stone, J., Mukherji, S. K., Muller, K. E., Pizer, S. M., 1999. Registration of 3D Cerebral Vessels With 2D Digital Angiograms: Clinical Evaluation. *Acad. Radiol.* 6 (9), 539–546.
- Bülöw, T., Lorenz, C., Renisch, S., 2004. A General Framework for Tree Segmentation and Reconstruction From Medical Volume Data. In: Proc. Int. Conf. Med. Image Comput. Comput. Assist. Interv. Vol. 3216 of Lect. Notes Comput. Sci. pp. 533–540.
- Busch, S., Johnson, T. R. C., Nikolaou, K., von Ziegler, F., Knez, A., Reiser, M. F., Becker, C. R., 2007. Visual and Automatic Grading of Coronary Artery Stenoses With 64-Slice CT Angiography in Reference to Invasive Angiography. *Eur. Radiol.* 17 (6), 1445–1451.
- Cademartiri, F., Grutta, L. L., Palumbo, A., Malagutti, P., Pugliese, F., Meijboom, W., Baks, T., Mollet, N., Bruining, N., Hamers, R., de Feyter, P., 2007. Non-Invasive Visualization of Coronary Atherosclerosis: State-of-Art. *J. Cardiovasc. Med.* 8 (3), 129–137.
- Carrillo, J., Hoyos, M., Dávila, E., Orkisz, M., 2007. Recursive Tracking of Vascular Tree Axes in 3D Medical Images. *Int. J. Comput. Ass. Radiol. and Surg.* 1 (6), 331–339.
- Castillo, E., Castillo, R., Martinez, J., Shenoy, M., Guerrero, T., 2010. Four-Dimensional Deformable Image Registration Using Trajectory Modeling. *Phys. Med. Biol.* 55 (1), 305–327.
- Castillo, R., Castillo, E., Guerra, R., Johnson, V. E., McPhail, T., Garg, A. K., Guerrero, T., 2009. A Framework for Evaluation of Deformable Image Registration Spatial Accuracy Using Large Landmark Point Sets. *Phys. Med. Biol.* 54 (7), 1849–1870.
- Castro, C., Luengo-Oroz, M. A., Santos, A., Ledesma-Carbayo, M. J., 2008. Coronary Artery Tracking in 3D Cardiac CT Images Using Local Morphological Reconstruction Operators. *Midas J. - Proc. MICCAI Workshop - Grand Challenge Coronary Artery Tracking*, <<http://hdl.handle.net/10380/1436>>.
- Chandrasekara, R., Rao, A., Sanchez-Ortiz, G., Mohiaddin, R., Rueckert, D., 2003. Construction of a Statistical Model for Cardiac Motion Analysis Using Nonrigid Image Registration. In: Proc. Inf. Process. Med. Imaging. Vol. 2732 of Lect. Notes Comput. Sci. pp. 599–610.
- Chen, X., Gilkeson, R., Fei, B., 2007. Automatic 3D-To-2D Registration for CT and Dual-Energy Digital Radiography for Calcification Detection. *Med. Phys.* 34 (12), 4934–4943.
- Christensen, G. E., Johnson, H. J., 2001. Consistent Image Registration. *IEEE Trans. Med. Imaging* 20 (7), 568–582.
- Chun, S., Schretter, C., Fessler, J., 2010. Sufficient Condition for Local Invertibility of Spatio-Temporal 4D B-Spline Deformations. In: Proc. IEEE Int. Symp. Biomed. Imaging. pp. 1221–1224.
- Cootes, T., Cooper, D., Taylor, C., Graham, J., 1995. Active Shape Models - Their Training and Application. *Comput. Vision Image Understanding* 61 (1), 38–59.
- Dai, Y.-H., 2001. An Efficient Hybrid Conjugate Gradient Method for Unconstrained Optimization. *Ann. Oper. Res.* 103, 33–47.
- Davatzikos, C., Shen, D., Mohamed, A., Kyriacou, S. K., 2001. A Framework for Predictive Modeling of Anatomical Deformations. *IEEE Trans. Med. Imaging* 20 (8), 836–843.

- Davies, S. W., 2001. Clinical Presentation and Diagnosis of Coronary Artery Disease: Stable Angina. *Br. Med. Bull.* 59, 17–27.
- de Bruijne, M., Lund, M., Tankó, L., Pettersen, P., Nielsen, M., 2007. Quantitative Vertebral Morphometry Using Neighbor-Conditional Shape Models. *Med. Image Anal.* 11 (5), 503–512.
- De Craene, M., Camara, O., Bijmens, B. H., Frangi, A. F., 2009. Large Diffeomorphic FFD Registration for Motion and Strain Quantification From 3D-US Sequences. In: *Proc. Funct. Imaging Model. Heart*. Vol. 5528 of *Lect. Notes Comput. Sci.* pp. 437–446.
- Deschamps, T., Cohen, L., 2001. Fast Extraction of Minimal Paths in 3D Images and Applications to Virtual Endoscopy. *Med. Image Anal.* 5, 281–299.
- Dewey, M., Schnapauff, D., Laule, M., Lembcke, A., Borges, A. C., Rutsch, W., Hamm, B., Rogalla, P., 2004. Multislice CT Coronary Angiography: Evaluation of an Automatic Vessel Detection Tool. *RöFo* 176 (4), 478–483.
- Dijkstra, E., 1959. A Note on Two Problems in Connexion With Graphs. *Num. Math.* 1 (1), 269–271.
- Dikici, E., O'Donnell, T., Grady, L., Setser, R., White, R., 2008. Coronary Artery Centerline Tracking Using Axial Symmetries. *Midas J. - Proc. MICCAI Workshop - Grand Challenge Coronary Artery Tracking*, <<http://hdl.handle.net/10380/1425>>.
- Dodge, J. T., Brown, B. G., Bolson, E. L., Dodge, H. T., 1992. Lumen Diameter of Normal Human Coronary Arteries. Influence of Age, Sex, Anatomic Variation, and Left Ventricular Hypertrophy or Dilation. *Circulation* 86 (1), 232–246.
- Ecabert, O., Peters, J., Schramm, H., Lorenz, C., von Berg, J., Walker, M. J., Vembar, M., Olszewski, M. E., Subramanyan, K., Lavi, G., Weese, J., 2008. Automatic Model-Based Segmentation of the Heart in CT Images. *IEEE Trans. Med. Imaging* 27 (9), 1189–1201.
- Ehrhardt, J., Werner, R., Schmidt-Richberg, A., Handels, H., 2010. A Statistical Shape and Motion Model for the Prediction of Respiratory Lung Motion. In: *Proc. SPIE Med Imaging: Image Process.* pp. 762353–1–762353–9.
- Eiho, S., Sekiguchi, H., N. Sugimoto, T. Hanakawa, S. U., 2004. Branch-Based Region Growing Method for Blood Vessel Segmentation. In: *Proc. Int. Soc. Photogramm. Remote Sens.* pp. 796–802.
- Einstein, A. J., Moser, K. W., Thompson, R. C., Cerqueira, M. D., Henzlova, M. J., 2007. Radiation Dose to Patients From Cardiac Diagnostic Imaging. *Circulation* 116 (11), 1290–1305.
- Failo, R., Wielopolski, P. A., Tiddens, H. A. W. M., Hop, W. C. J., Mucelli, R. P., Lequin, M. H., 2009. Lung Morphology Assessment Using MRI: A Robust Ultra-Short TR/TE 2D Steady State Free Precession Sequence Used in Cystic Fibrosis Patients. *Magn. Reson. Med* 61 (2), 299–306.
- Figl, M., Rueckert, D., Hawkes, D., Casula, R., Hu, M., Pedro, O., Zhang, D. P., Penney, G., Bello, F., Edwards, P., 2010. Image Guidance For Robotic Minimally Invasive Coronary Artery Bypass. *Comput. Med. Imaging Graph.* 34 (1), 61–68.
- Figueras, C., Sukno, F., Frangi, A., 2010. Bilinear Point Distribution Models for Heart Motion Analysis. In: *Proc. IEEE Int. Symp. Biomed. Imaging*. pp. 476–479.
- Florin, C., Moreau-Gobard, R., Williams, J., 2004. Automatic Heart Peripheral Vessels Segmentation Based On Normal MIP Ray Casting Technique. In: *Proc. Int. Conf. Med. Image Comput. Comput. Assist. Interv.* Vol. 3216 of *Lect. Notes Comput. Sci.* pp. 483–490.
- Florin, C., Paragios, N., Williams, J., 2005. Particle Filters, a Quasi-Monte Carlo Solution for Segmentation of Coronaries. In: *Proc. Int. Conf. Med. Image Comput. Comput. Assist. Interv.* Vol. 3749 of *Lect. Notes Comput. Sci.* pp. 246–253.



- Florin, C., Paragios, N., Williams, J., 2006. Globally Optimal Active Contours, Sequential Monte Carlo and On-Line Learning for Vessel Segmentation. In: Proc. Eur. Conf. Comput. Vision. pp. 476–489.
- Fogel, E., Teillaud, M., 2006. Generic Programming and the CGAL Library. Springer.
- Frangi, A., Niessen, W., Vincken, K., Viergever, M., 1998. Multiscale Vessel Enhancement Filtering. In: Proc. Int. Conf. Med. Image Comput. Comput. Assist. Interv. Vol. 1496 of Lect. Notes Comput. Sci. pp. 130–137.
- Frangi, A., Rueckert, D., Schnabel, J., Niessen, W., 2002. Automatic Construction of Multiple-Object Three-Dimensional Statistical Shape Models: Application to Cardiac Modeling. IEEE Trans. Med. Imaging 21 (9), 1151–1166.
- Friman, O., Hindennach, M., Peitgen, H.-O., 2008a. Template-Based Multiple Hypotheses Tracking of Small Vessels. In: Proc. IEEE Int. Symp. Biomed. Imaging. pp. 1047–1050.
- Friman, O., Kühnel, C., Peitgen, H.-O., 2008b. Coronary Artery Centerline Extraction Using Multiple Hypothesis Tracking and Minimal Paths. Midas J. - Proc. MICCAI Workshop - Grand Challenge Coronary Artery Tracking, <<http://hdl.handle.net/10380/1433>>.
- Fritz, D., Rinck, D., Dillmann, R., Scheuering, M., 2006. Segmentation of the Left and Right Cardiac Ventricle Using a Combined Bi-Temporal Statistical Model. In: Proc. SPIE Med Imaging: Image Process. pp. 605–614.
- Fritz, D., Rinck, D., Unterhinninghofen, R., Dillmann, R., Scheuering, M., 2005. Automatic Segmentation of the Left Ventricle and Computation of Diagnostic Parameters Using Regiongrowing and a Statistical Model. In: Proc. SPIE Med Imaging: Image Process. Vol. 5747. pp. 1844–1854.
- Gamble, G., Zorn, J., Sanders, G., MacMahon, S., Sharpe, N., 1994. Estimation of Arterial Stiffness, Compliance, and Distensibility From M-Mode Ultrasound Measurements of the Common Carotid Artery. Stroke 25 (1), 11–16.
- Ganten, M.-K., Krautter, U., von Tengg-Kobligh, H., Böckler, D., Schumacher, H., Stiller, W., Delorme, S., Kauczor, H.-U., Kauffmann, G. W., Bock, M., 2008. Quantification of Aortic Distensibility in Abdominal Aortic Aneurysm Using ECG-Gated Multi-Detector Computed Tomography. Eur. Radiol. 18 (5), 966–973.
- Geladi, P., Kowalski, B., 1986. Partial Least-Squares Regression: A Tutorial. Anal. Chim. Acta 185, 1–17.
- Geng, X., Kumar, D., Christensen, G. E., 2005. Transitive Inverse-Consistent Manifold Registration. In: Proc. Inf. Process. Med. Imaging. Vol. 3565 of Lect. Notes Comput. Sci. pp. 468–479.
- Goodall, C., 1991. Procrustes Methods in the Statistical Analysis of Shape. J. Roy. Stat. Soc. B. 53 (2), 285–339.
- Grech, E. D., 2011. ABC of Interventional Cardiology. Wiley-Blackwell.
- Groher, M., Baust, M., Zikic, D., Navab, N., 2010. Monocular Deformable Model-to-Image Registration of Vascular Structures. In: Proc. Int. Workshop Biomed. Image Regis. Vol. 6204 of Lect. Notes Comput. Sci. pp. 37–47.
- Groher, M., Jakobs, T. F., Padoy, N., Navab, N., 2007. Planning and Intraoperative Visualization of Liver Catheterizations: New CTA Protocol and 2D-3D Registration Method. Acad. Radiol. 14 (11), 1325–1340.
- Groher, M., Zikic, D., Navab, N., 2009. Deformable 2D-3D Registration of Vascular Structures in a One View Scenario. IEEE Trans. Med. Imaging 28 (6), 847–860.
- Gulsun, M. A., Tek, H., 2008. Robust Vessel Tree Modeling. In: Proc. Int. Conf. Med. Image Comput. Comput. Assist. Interv. Vol. 5241 of Lect. Notes Comput. Sci. pp. 602–611.
- Haase, J., Schäfers, H.-J., Sievert, H., Waksman, R. (Eds.), 2008. Cardiovascular Interventions in Clinical Practice. Wiley-Blackwell.
- Hastie, T., Tibshirani, R., Friedman, J., 2009. The Elements of Statistical Learning. Springer.

- Hawkes, D. J., Barratt, D., Blackall, J. M., Chan, C., Edwards, P. J., Rhode, K., Penney, G. P., McClelland, J., Hill, D. L. G., 2005. Tissue Deformation and Shape Models in Image-Guided Interventions: A Discussion Paper. *Med. Image Anal.* 9 (2), 163–175.
- Hecht, H. S., 2008. Applications of Multislice Coronary Computed Tomographic Angiography to Percutaneous Coronary Intervention: How Did We Ever Do Without It? *Catheter. Cardiovasc. Interv.* 71 (4), 490–503.
- Heimann, T., Meinzer, H.-P., 2009. Statistical Shape Models for 3D Medical Image Segmentation: A Review. *Med. Image Anal.* 13 (4), 543–563.
- Hennemuth, A., Bock, S., Boskamp, T., Fritz, D., Kühnel, C., Rinck, D., Scheuering, M., Peitgen, H. O., 2005. One-Click Coronary Tree Segmentation in CT Angiographic Images. In: *Proc. Int. Conf. Comput. Ass. Radiol. and Surg.* pp. 317–321.
- Hernández Hoyos, M., Orkisz, M., Douek, P. C., Magnin, I. E., 2005. Assessment of Carotid Artery Stenoses in 3D Contrast-Enhanced Magnetic Resonance Angiography, Based on Improved Generation of the Centerline. *Mach. Graphics & Vision* 14 (4), 349–378.
- Hernández Hoyos, M., Zuluaga, M. A., Lozano, M., Prieto, J. C., Douek, P. C., Magnin, I. E., Orkisz, M., 2008. Coronary Centerline Tracking in CT Images With Use of an Elastic Model and Image Moments. *Midas J. - Proc. MICCAI Workshop - Grand Challenge Coronary Artery Tracking*, <<http://hdl.handle.net/10380/1401>>.
- Hill, D., Batchelor, P., Holden, M., Hawkes, D., 2001. Medical Image Registration. *Phys. Med. Biol.* 46 (3), R1–R45.
- Hipwell, J., Penney, G., McLaughlin, R., Rhode, K., Summers, P., Cox, T., Byrne, J., Noble, J., Hawkes, D., 2003. Intensity-Based 2-D-3-D Registration of Cerebral Angiograms. *IEEE Trans. Med. Imaging* 22 (11), 1417–1426.
- Hoffmann, U., Moselewski, F., Nieman, K., Jang, I.-K., Ferencik, M., Rahman, A. M., Cury, R. C., Abbata, S., Joneidi-Jafari, H., Achenbach, S., Brady, T. J., 2006. Noninvasive Assessment of Plaque Morphology and Composition in Culprit and Stable Lesions in Acute Coronary Syndrome and Stable Lesions in Stable Angina by Multidetector Computed Tomography. *J. Am. Coll. Cardiol.* 47 (8), 1655–1662.
- Hong, M.-K., Mintz, G., et al., 2005. The Site of Plaque Rupture in Native Coronary Arteries: A Three-Vessel Intravascular Ultrasound Analysis. *J. Am. Coll. Cardiol.* 46 (2), 261–265.
- Hoogendoorn, C., Sukno, F., Ordás, S., Frangi, A., 2009. Bilinear Models for Spatio-Temporal Point Distribution Analysis. *Int. J. Comput. Vision* 85 (3), 237–252.
- Hoover, A., Jean-Baptiste, G., Jiang, X., Flynn, P., Bunke, H., Goldgof, D., Bowyer, K., Eggert, D., Fitzgibbon, A., Fisher, R., 1996. An Experimental Comparison of Range Image Segmentation Algorithms. *IEEE Trans. Pattern Anal. Mach. Intell.* 18 (7), 673–689.
- Hoye, A., van Domburg, R. T., Sonnenschein, K., Serruys, P. W., 2005. Percutaneous Coronary Intervention for Chronic Total Occlusions: The Thoraxcenter Experience 1992-2002. *Eur. Heart J.* 26 (24), 2630–2636.
- Iglesias, J. E., de Bruijne, M., 2007. Semiautomatic Segmentation of Vertebrae in Lateral X-Rays Using a Conditional Shape Model. *Acad. Radiol.* 14 (10), 1156–1165.
- Imamura, H., Ida, N., Sugimoto, N., Eiho, S., i. Urayama, S., Ueno, K., Inoue, K., 2002. Registration of Preoperative CTA and Intraoperative Fluoroscopic Images for Assisting Aortic Stent Grafting. In: *Proc. Int. Conf. Med. Image Comput. Comput. Assist. Interv. Vol. 2489 of Lect. Notes Comput. Sci.* pp. 477–484.
- Izenman, A., 2008. Modern Multivariate Statistical Techniques: Regression, Classification, and Manifold Learning. Springer Texts in Statistics. Springer.
- Jeong, J., Stough, J., Marron, J., Pizer, S., 2008. Conditional-mean Initialization Using Neighboring Objects in Deformable Model Segmentation. In: *Proc. SPIE Med Imaging: Image Process.* pp. 69144R–1–69144R–9.



- Jeron, A., Fredersdorf, S., Debl, K., Oren, E., Izmirli, A., Peleg, A., Nekovar, A., Herscovici, A., Riegger, G. A., Luchner, A., 2009. First-in-Man (FIM) Experience With the Magnetic Medical Positioning System (MPS) for intraCoronary navigation. *EuroIntervention* 5 (5), 552–557.
- Jomier, J., Bullitt, E., Horn, M. V., Pathak, C., Aylward, S. R., 2006. 3D/2D Model-to-Image Registration Applied to TIPS Surgery. In: *Proc. Int. Conf. Med. Image Comput. Comput. Assist. Interv.* Vol. 3023 of *Lect. Notes Comput. Sci.* pp. 662–669.
- Joshi, S., Davis, B., Jomier, M., Gerig, G., 2004. Unbiased Diffeomorphic Atlas Construction For Computational Anatomy. *NeuroImage* 23 Suppl 1, S151–S160.
- Kabus, S., Klinder, T., Murphy, K., van Ginneken, B., Lorenz, C., Pluim, J., 2009. Evaluation of 4D-CT Lung Registration. In: *Proc. Int. Conf. Med. Image Comput. Comput. Assist. Interv.* Vol. 5761 of *Lect. Notes Comput. Sci.* pp. 747–757.
- Kanitsar, A., Fleischmann, D., Wegenkittl, R., Felkel, P., Gröller, M. E., 2002. CPR - Curved Planar Reformation. In: *Proc. IEEE Visualization.* pp. 37–44.
- Kasper, D. L., Braunwald, E., Fauci, A. S., Hauser, S. L., Longo, D. L., Jameson, J. L., 2005. *Harrison's Principles of Internal Medicine*, 2nd Edition. McGraw-Hill.
- Kaus, M., Netsch, T., Kabus, S., Pekar, V., McNutt, T., Fischer, B., 2004. Estimation of Organ Motion From 4D CT for 4D Radiation Therapy Planning of Lung Cancer. In: *Proc. Int. Conf. Med. Image Comput. Comput. Assist. Interv.* Vol. 3217 of *Lect. Notes Comput. Sci.* pp. 1017–1024.
- Khan, M. F., Wesarg, S., Gurung, J., Dogan, S., Maataoui, A., Brehmer, B., Herzog, C., Ackermann, H., Assmus, B., Vogl, T. J., 2006. Facilitating Coronary Artery Evaluation in MDCT Using a 3D Automatic Vessel Segmentation Tool. *Eur. Radiol.* 16 (8), 1789–1795.
- Kirisli, H., Schaap, M., Klein, S., Neefjes, L., Weustink, A., van Walsum, T., Niessen, W., 2010. Fully Automatic Cardiac Segmentation From 3D CTA Data: A Multiatlas Based Approach. In: *Proc. SPIE Med Imaging: Image Process.* pp. 762305–1–762305–9.
- Kitslaar, P., Frenay, M., Oost, E., Dijkstra, J., Stoel, B., Reiber, J. H., 2008. Connected Component and Morphology Based Extraction of Arterial Centerlines of the Heart (CocomoBeach). *Midas J. - Proc. MICCAI Workshop - Grand Challenge Coronary Artery Tracking*, <<http://hdl.handle.net/10380/1460>>.
- Klein, S., Pluim, J. P., Staring, M., Viergever, M. A., 2009. Adaptive Stochastic Gradient Descent Optimisation for Image Registration. *Int. J. Comput. Vision* 81 (3), 227–239.
- Klein, S., Staring, M., , Pluim, J. P W., 2007. Evaluation of Optimisation Methods for Nonrigid Medical Image Registration Using Mutual Information and B-Splines. *IEEE Trans. Image Process.* 16 (12), 2879–2890.
- Klein, S., Staring, M., Murphy, K., Viergever, M., Pluim, J., 2010. *elastix*: A Toolbox for Intensity Based Medical Image Registration. *IEEE Trans. Med. Imaging* 29 (1), 196–205.
- Klinder, T., Lorenz, C., Ostermann, J., 2010. Prediction Framework for Statistical Respiratory Motion Modeling. In: *Proc. Int. Conf. Med. Image Comput. Comput. Assist. Interv.* Vol. 6363 of *Lect. Notes Comput. Sci.* pp. 327–334.
- Krissian, K., Bogunovic, H., Pozo, J., Villa-Uriol, M., Frangi, A., 2008. Minimally Interactive Knowledge-based Coronary Tracking in CTA using a Minimal Cost Path. *Midas J. - Proc. MICCAI Workshop - Grand Challenge Coronary Artery Tracking*, <<http://hdl.handle.net/10380/1435>>.
- Laguitton, S., Boldak, C., Bousse, A., Yang, G., Toumoulin, C., 2006. Temporal Tracking of Coronaries in MSCTA by Means of 3D Geometrical Moments. In: *Proc. IEEE Eng. Med. Biol. Soc.* pp. 924–927.
- Lapp, R., Lorenzo-Valdés, M., Rueckert, D., 2004. 3D/4D Cardiac Segmentation Using Active Appearance Models, Non-Rigid Registration, and the Insight Toolkit. In: *Proc. Int. Conf. Med. Image Comput. Comput. Assist. Interv.* Vol. 3216 of *Lect. Notes Comput. Sci.* pp. 419–426.

- Larralde, A., Boldak, C., Garreau, M., Toumoulin, C., Boulmier, D., Rolland, Y., 2003. Evaluation of a 3D Segmentation Software for the Coronary Characterization in Multi-slice Computed Tomography. In: Proc. Funct. Imaging Model. Heart. Vol. 2674 of Lect. Notes Comput. Sci. pp. 1005–1005.
- Lavi, G., Lessick, J., Johnson, P., Khullar, D., 2004. Single-Seeded Coronary Artery Tracking in CT angiography. In: Proc. IEEE Nucl. Sci. Symp. Conf. pp. 3308–3311.
- Law, M., Chung, A., 2009. Efficient Implementation for Spherical Flux Computation and Its Application to Vascular Segmentation. IEEE Trans. Med. Imaging 18 (3), 596–612.
- Leber, A., Becker, A., Knez, A., von Ziegler, F., Sirol, M., Nikolaou, K., Ohnesorge, B., Fayad, Z., Becker, C., Reiser, M., Steinbeck, G., Boekstegers, P., 2006. Accuracy of 64-Slice Computed Tomography to Classify and Quantify Plaque Volumes in the Proximal Coronary System: a Comparative Study Using Intravascular Ultrasound. J. Am. Coll. Cardiol. 47 (3), 672–677.
- Lehman, S. J., Schlett, C. L., Bamberg, F., Lee, H., Donnelly, P., Shturman, L., Kriegel, M. F., Brady, T. J., Hoffmann, U., 2009. Assessment of Coronary Plaque Progression in Coronary Computed Tomography Angiography Using a Semiquantitative Score. J. Am. Coll. Cardiol. Cardiovasc. Imaging 2 (11), 1262–1270.
- Lesage, D., Angelini, E., Bloch, I., Funka-Lea, G., 2008. Medial-Based Bayesian Tracking for Vascular Segmentation: Application to Coronary arteries in 3D CT Angiography. In: Proc. IEEE Int. Symp. Biomed. Imaging. pp. 268–271.
- Leschka, S., Alkadhi, H., Plass, A., Desbiolles, L., Grünenfelder, J., Marincek, B., Wildermuth, S., 2005. Accuracy of MSCT Coronary Angiography With 64-Slice Technology: First Experience. Eur. Heart J. 26 (15), 1482–1487.
- Li, G., Citrin, D., Camphausen, K., Mueller, B., Burman, C., Mychalczak, B., Miller, R. W., Song, Y., 2008a. Advances in 4D Medical Imaging and 4D Radiation Therapy. Technol. Cancer Res. Treat. 7 (1), 67–81.
- Li, H., Yezzi, A., 2007. Vessels as 4-D Curves: Global Minimal 4-D Paths to Extract 3-D Tubular Surfaces and Centerlines. IEEE Trans. Med. Imaging 26, 1213–1223.
- Li, Z.-Y., Howarth, S., Graves, M., Gillard, J. H., 2008b. Measurement of Stenotic Carotid Arterial Compliance With MRI. In: Proc. IEEE Eng. Med. Biol. Soc. pp. 1403–1406.
- Lindeberg, T., 1996. Edge Detection and Ridge Detection With Automatic Scale Selection. In: Proc. IEEE Conf. Comput. Vision Pattern Recognit. pp. 465–470.
- Liu, X., Oguz, I., Pizer, S., Mageras, G., 2010. Shape-Related Deformation Statistics for Respiratory Motion Prediction in 4D Lung. In: Proc. SPIE Med Imaging: Image Process. pp. 76252D–1–76252D–10.
- Lopez, A., Fritscher, K. D., Trieb, T., Schubert, R., Mattes, J., 2008. 3D Inter-subject Cardiac Registration Using 4D Information. In: Proc. SPIE Med Imaging: Image Process. pp. 691413–1–691413–10.
- Lorenz, C., Renisch, S., Schlathoelter, T., Buelow, T., 2003. Simultaneous Segmentation and Tree Reconstruction of the Coronary Arteries in MSCT Images. In: Proc. SPIE Med Imaging: Image Process. pp. 167–177.
- Lorenz, C., von Berg, J., 2006. A Comprehensive Shape Model of the Heart. Med. Image Anal. 10 (4), 657–670.
- Lorenzo-Valdés, M., Sanchez-Ortiza, G. I., Mohiaddin, R., Rueckert, D., 2002. Atlas-Based Segmentation and Tracking of 3D Cardiac MR Images Using Non-rigid Registration. In: Proc. Int. Conf. Med. Image Comput. Comput. Assist. Interv. Vol. 2488 of Lect. Notes Comput. Sci. pp. 642–650.
- Luengo-Oroz, M. A., Ledesma-Carbayo, M. J., Gómez-Diego, J. J., García-Fernández, M. A., Desco, M., Santos, A., 2007. Extraction of the Coronary Artery Tree in Cardiac Computer Tomographic Images Using Morphological Operators. In: Proc. Funct. Imaging Model. Heart. Vol. 3749 of Lect. Notes Comput. Sci. pp. 424–432.



- Mahnken, A. H., Bruners, P., Schmidt, B., Bornikoel, C., Flohr, T., Günther, R. W., 2009. Left Ventricular Function Can Reliably Be Assessed From Dual-Source CT Using ECG-Gated Tube Current Modulation. *Invest. Radiol.* 44 (7), 384–389.
- Maintz, J. B., Viergever, M. A., 1998. A Survey of Medical Image Registration. *Med. Image Anal.* 2 (1), 1–36.
- Mansi, T., Peyrat, J.-M., Sermesant, M., Delingette, H., Blanc, J., Boudjemline, Y., Ayache, N., 2009. Physically-Constrained Diffeomorphic Demons for the Estimation of 3D Myocardium Strain From Cine-MRI. In: *Proc. Funct. Imaging Model. Heart*. Vol. 5528 of *Lect. Notes Comput. Sci.* pp. 201–210.
- Marieb, E., 2007. *Human Anatomy & Physiology*. Addison Wesley Longman.
- Markelj, P., Tomaževič, D., Likar, B., Pernuš, F., in press. A Review of 3D/2D Registration Methods for Image-Guided Interventions. *Med. Image Anal.*
- Marquering, H. A., Dijkstra, J., de Koning, P. J. H., Stoel, B. C., Reiber, J. H. C., 2005. Towards Quantitative Analysis of Coronary CTA. *Int. J. Cardiovasc. Imaging* 21 (1), 73–84.
- Marsland, S., Twining, C., Taylor, C., 2003. Groupwise Non-Rigid Registration Using Polyharmonic Clamped-Plate Splines. In: *Proc. Int. Conf. Med. Image Comput. Comput. Assist. Interv.* Vol. 2879 of *Lect. Notes Comput. Sci.* pp. 771–779.
- Marsland, S., Twining, C., Taylor, C., 2008. A Minimum Description Length Objective Function for Groupwise Non-Rigid Image Registration. *Image Vision Comput.* 26 (3), 333–346.
- Martin, D., Fowlkes, C., Tal, D., Malik, J., 2001. A Database of Human Segmented Natural Images and Its Application to Evaluating Segmentation Algorithms and Measuring Ecological Statistics. In: *Proc. Int. Conf. Comput. Vision*. pp. 416–423.
- McLaughlin, R. A., Hipwell, J., Hawkes, D. J., Noble, J. A., Byrne, J. V., Cox, T. C., 2005. A Comparison of a Similarity-Based and a Feature-Based 2-D-3-D Registration Method for Neurointerventional Use. *IEEE Trans. Med. Imaging* 24 (8), 1058–1066.
- Metz, C., Baka, N., Kirisli, H., Schaap, M., van Walsum, T., Klein, S., Neefjes, L., Mollet, N., Lelieveldt, B., de Bruijne, M., et al., 2010. Conditional Shape Models for Cardiac Motion Estimation. In: *Proc. Int. Conf. Med. Image Comput. Comput. Assist. Interv.* Vol. 6361 of *Lect. Notes Comput. Sci.* pp. 452–459.
- Metz, C., Schaap, M., Klein, S., Neefjes, L., Capuano, E., Schultz, C., van Geuns P.W. Serruys T. van Walsum, R., Niessen, W., 2009a. Patient Specific 4D Coronary Models From ECG-gated CTA Data for Intra-operative Dynamic Alignment of CTA With X-ray Images. In: *Proc. Int. Conf. Med. Image Comput. Comput. Assist. Interv.* Vol. 5761 of *Lect. Notes Comput. Sci.* pp. 369–376.
- Metz, C., Schaap, M., Klein, S., Weustink, A., Mollet, N., Schulz, C., Geuns, R., Serruys, P., Niessen, W., 2009b. GPU Accelerated Alignment of 3-D CTA With 2-D X-Ray Data for Improved Guidance in Coronary Interventions. In: *Proc. IEEE Int. Symp. Biomed. Imaging*. pp. 959–962.
- Metz, C., Schaap, M., van der Giessen, A., van Walsum, T., Niessen, W., 2007. Semi-Automatic Coronary Artery Centerline Extraction in Computed Tomography Angiography Data. In: *Proc. IEEE Int. Symp. Biomed. Imaging*. pp. 856–859.
- Metz, C., Schaap, M., van Walsum, T., Niessen, W., 2008a. Two Point Minimum Cost Path Approach for CTA Coronary Centerline Extraction. *Midas J. - Proc. MICCAI Workshop - Grand Challenge Coronary Artery Tracking*, <<http://hdl.handle.net/10380/1510>>.
- Metz, C., Schaap, M., van Walsum, T., van der Giessen, A., Weustink, A., Mollet, N., Krestin, G., Niessen, W., 2008b. 3D Segmentation in the Clinic: A Grand Challenge II - Coronary Artery Tracking. *Midas J. - Proc. MICCAI Workshop - Grand Challenge Coronary Artery Tracking*, <<http://hdl.handle.net/10380/1399>>.
- MeVisLab, Software for Medical Image Processing and Visualization. <http://www.mevislab.de>.

- Miller, E., Matsakis, N., Viola, P., 2000. Learning From One Example Through Shared Densities on Transforms. In: Proc. IEEE Conf. Comput. Vision Pattern Recognit. pp. 464–471.
- Milles, J., van der Geest, R. J., Jerosch-Herold, M., Reiber, J. H. C., Lelieveldt, B. P. F., 2008. Fully Automated Motion Correction in First-Pass Myocardial Perfusion MR Image Sequences. *IEEE Trans. Med. Imaging* 27 (11), 1611–1621.
- Mitchell, S., Bosch, J., Lelieveldt, B., van der Geest, R., Reiber, J., Sonka, M., 2002. 3-D Active Appearance Models: Segmentation of Cardiac MR and Ultrasound Images. *IEEE Trans. Med. Imaging* 21 (9), 1167–1178.
- Mowatt, G., Cummins, E., Waugh, N., Walker, S., Cook, J., Jia, X., Hillis, G. S., Fraser, C., 2008. Systematic Review of the Clinical Effectiveness and Cost-Effectiveness of 64-Slice or Higher Computed Tomography Angiography as an Alternative to Invasive Coronary Angiography in the Investigation of Coronary Artery Disease. *Health Technol. Assess.* 12 (17), iii–iv, ix–143.
- Nain, D., Yezzi, A., Turk, G., 2004. Vessel Segmentation Using a Shape Driven Flow. In: Proc. Int. Conf. Med. Image Comput. Comput. Assist. Interv. Vol. 3216 of Lect. Notes Comput. Sci. pp. 51–59.
- Olabarriaga, S., Breeuwer, M., Niessen, W., 2003. Minimum Cost Path Algorithm for Coronary Artery Central Axis Tracking in CT Images. In: Proc. Int. Conf. Med. Image Comput. Comput. Assist. Interv. Vol. 2879 of Lect. Notes Comput. Sci. pp. 687–694.
- Ordas, S., Oubel, E., Leta, R., Carreras, F., Frangi, A., 2007. A Statistical Shape Model of the Heart and Its Application to Model-Based Segmentation. In: Proc. SPIE Med Imaging: Image Process. pp. 65111K–1–65111K–11.
- Perperidis, D., Mohiaddin, R., Rueckert, D., 2005. Construction of a 4D Statistical Atlas of the Cardiac Anatomy and Its Use in Classification. In: Proc. Int. Conf. Med. Image Comput. Comput. Assist. Interv. Vol. 3750 of Lect. Notes Comput. Sci. pp. 402–410.
- Peyrat, J., Delingette, H., Sermesant, M., Xu, C., Ayache, N., 2010. Registration of 4D Cardiac CT Sequences Under Trajectory Constraints With Multichannel Diffeomorphic Demons. *IEEE Trans. Med. Imaging* 29 (7), 1351–1368.
- Ramcharitar, S., Patterson, M. S., van Geuns, R. J., van der Ent, M., Sianos, G., Welten, G. M. J. M., van Domburg, R. T., Serruys, P. W., 2007. A Randomised Controlled Study Comparing Conventional and Magnetic Guidewires in a Two-Dimensional Branching Tortuous Phantom Simulating Angulated Coronary Vessels. *Catheter. Cardiovasc Interv.* 70 (5), 662–668.
- Ramcharitar, S., Patterson, M. S., van Geuns, R. J., van Meighem, C., Serruys, P. W., 2008. Technology Insight: Magnetic Navigation in Coronary Interventions. *Nat. Clin. Pract. Cardiovasc. Med.* 5 (3), 148–156.
- Ramcharitar, S., Pugliese, F., Schultz, C., Ligthart, J., de Feyter, P., Li, H., Mollet, N., van de Ent, M., Serruys, P. W., van Geuns, R. J., 2009. Integration of Multislice Computed Tomography With Magnetic Navigation Facilitates Percutaneous Coronary Interventions Without Additional Contrast Agents. *J. Am. Coll. Cardiol.* 53 (9), 741–746.
- Ramcharitar, S., van der Giessen, W. J., van der Ent, M., Serruys, P. W., van Geuns, R. J., in press. Randomized Comparison of the Magnetic Navigation System vs. Standard Wires in the Treatment of Bifurcations. *Eur. Heart J.*
- Rao, A., Aljabar, P., Rueckert, D., 2008. Hierarchical Statistical Shape Analysis and Prediction of Sub-Cortical Brain Structures. *Med. Image Anal.* 12 (1), 55–68.
- Rao, A., Sanchez-Ortiz, G. I., Chandrashekhara, R., Lorenzo-Valdés, M., Mohiaddin, R., Rueckert, D., 2002. Comparison of Cardiac Motion Across Subjects Using Non-Rigid Registration. In: Proc. Int. Conf. Med. Image Comput. Comput. Assist. Interv. Vol. 2488 of Lect. Notes Comput. Sci. pp. 722–729.



- Reinhardt, J. M., Ding, K., Cao, K., Christensen, G. E., Hoffman, E. A., Bodas, S. V., 2008. Registration-Based Estimates of Local Lung Tissue Expansion Compared to Xenon CT Measures of Specific Ventilation. *Med. Image Anal.* 12 (6), 752–763.
- Renard, F., Yang, Y., 2008. Image Analysis for Detection of Coronary Artery Soft Plaques in MDCT Images. In: *Proc. IEEE Int. Symp. Biomed. Imaging*. pp. 25–28.
- Rietzel, E., Chen, G. T. Y., 2006. Deformable Registration of 4D Computed Tomography Data. *Med. Phys.* 33 (11), 4423–4430.
- Rollano-Hijarrubia, E., Stokking, R., van der Meer, F., Niessen, W., 2006. Imaging of Small High-Density Structures in CT: A Phantom Study. *Acad. Radiol.* 13 (7), 893–908.
- Ropers, D., Rixe, J., Anders, K., Küttner, A., Baum, U., Bautz, W., Daniel, W. G., Achenbach, S., 2006. Usefulness of Multidetector Row Spiral Computed Tomography With 64- x 0.6-mm Collimation and 330-ms Rotation for the Noninvasive Detection of Significant Coronary Artery Stenoses. *Am. J. of Cardiol.* 97 (3), 343–348.
- Rosamond, W., Flegal, K., Furie, K., Go, A., Greenlund, K., Haase, N., Hailpern, S. M., Ho, M., Howard, V., Kissela, B., Kittner, S., Lloyd-Jones, D., McDermott, M., Meigs, J., Moy, C., Nichol, G., O'Donnell, C., Roger, V., Sorlie, P., Steinberger, J., Thom, T., Wilson, M., Hong, Y., 2008. Heart Disease and Stroke Statistics – 2008 Update: Report From the American Heart Association Statistics Committee and Stroke Statistics Subcommittee. *Circulation* 117, 25–146.
- Rueckert, D., Sonoda, L. I., Hayes, C., Hill, D. L., Leach, M. O., Hawkes, D. J., 1999. Nonrigid Registration Using Free-Form Deformations: Application to Breast MR Images. *IEEE Trans. Med. Imaging* 18 (8), 712–721.
- Ruijters, D., ter Haar Romeny, B. M., Suetens, P., 2009. Vesselness-Based 2D-3D Registration of the Coronary Arteries. *Int. J. Comput. Assist. Radiol. Surg.* 4 (4), 391–397.
- Saur, S., Kühnel, C., Boskamp, T., Székely, G., Cattin, P., 2008. Automatic Ascending Aorta Detection in CTA Datasets. In: *Proc. Bildverarb. für der Med.* pp. 323–327.
- Schaap, M., 2010. Quantitative Image Analysis in Cardiac CT Angiography. Ph.D. thesis, Erasmus University Rotterdam.
- Schaap, M., Manniesing, R., Smal, I., van Walsum, T., Niessen, W., 2007. Bayesian Tracking of Tubular Structures and Its Application to Carotid Arteries in CTA. In: *Proc. Int. Conf. Med. Image Comput. Comput. Assist. Interv.* Vol. 4792 of *Lect. Notes Comput. Sci.* pp. 562–570.
- Scharstein, D., Szeliski, R., 2002. A Taxonomy and Evaluation of Dense Two-Frame Stereo Correspondence Algorithms. *Int. J. Comput. Vision* 47, 7–42.
- Schreibmann, E., Thorndyke, B., Li, T., Wang, J., Xing, L., 2008. Four-Dimensional Image Registration for Image-Guided Radiotherapy. *Int. J. Radiat. Oncol. Biol. Phys.* 71 (2), 578–586.
- Schroeder, W., Martin, K., Lorensen, B., 1997. *The Visualization Toolkit: An Object-Oriented Approach to 3-D Graphics (2nd Edition)*. Prentice Hall.
- SDika, M., 2008. A Fast Nonrigid Image Registration With Constraints on the Jacobian Using Large Scale Constrained Optimization. *IEEE Trans. Med. Imaging* 27 (2), 271–281.
- Serruys, P. W., 2006. Fourth Annual American College of Cardiology International Lecture: A Journey in the Interventional Field. *J. Am. Coll. Cardiol.* 47 (9), 1754–1768.
- Shang, Y., Dossel, O., 2004. Statistical 3D Shape-Model Guided Segmentation of Cardiac Images. In: *Proc. Comp. in Cardiol.* pp. 553–556.
- Shechter, G., Ozturk, C., Resar, J. R., McVeigh, E. R., 2004. Respiratory Motion of the Heart From Free Breathing Coronary Angiograms. *IEEE Trans. Med. Imaging* 23 (8), 1046–1056.

- Shechter, G., Resar, J. R., McVeigh, E. R., 2006. Displacement and Velocity of the Coronary Arteries: Cardiac and Respiratory Motion. *IEEE Trans. Med. Imaging* 25 (3), 369–375.
- Shoemake, K., 1985. Animating Rotation With Quaternion Curves. In: *Proc. Annu. Conf. Comput. Graphics and Interact. Tech. - SIGGRAPH*. pp. 245–254.
- Staal, J., Abramoff, M., Niemeijer, M., Viergever, M., van Ginneken, B., 2004. Ridge-Based Vessel Segmentation in Color Images of the Retina. *IEEE Trans. Med. Imaging* 23 (4), 501–509.
- Sundar, H., Litt, H., Shen, D., 2009. Estimating Myocardial Motion by 4D Image Warping. *Pattern. Recognit.* 42 (11), 2514–2526.
- Szymczak, A., 2008. Vessel Tracking by Connecting the Dots. *Midas J. - Proc. MICCAI Workshop - Grand Challenge Coronary Artery Tracking*, <<http://hdl.handle.net/10380/1406>>.
- Szymczak, A., Stillman, A., Tannenbaum, A., Mischaikow, K., 2006. Coronary Vessel Trees From 3D Imagery: A Topological Approach. *Med. Image Anal.* 10 (4), 548–559.
- Tek, H., Gulsun, M. A., Laguitton, S., Grady, L., Lesage, D., Funka-Lea, G., 2008. Automatic Coronary Tree Modeling. *Midas J. - Proc. MICCAI Workshop - Grand Challenge Coronary Artery Tracking*, <<http://hdl.handle.net/10380/1426>>.
- Tsuchida, K., Colombo, A., Lefèvre, T., Oldroyd, K. G., Guetta, V., Guagliumi, G., von Scheidt, W., Ruzyllo, W., Hamm, C. W., Bressers, M., Stoll, H.-P., Wittebols, K., Donohoe, D. J., Serruys, P. W., 2007. The Clinical Outcome of Percutaneous Treatment of Bifurcation Lesions in Multivessel Coronary Artery Disease With the Sirolimus-Eluting Stent: Insights From the Arterial Revascularization Therapies Study Part II (ARTS II). *Eur. Heart J.* 28 (4), 433–442.
- Turgeon, G.-A., Lehmann, G., Guiraudon, G., Drangova, M., Holdsworth, D., Peters, T., 2005. 2D-3D Registration of Coronary Angiograms for Cardiac Procedure Planning and Guidance. *Med. Phys.* 32 (12), 3737–3749.
- Unser, M., 1999. Splines: A Perfect Fit for Signal and Image Processing. *IEEE Signal. Process. Mag.* 16 (6), 22–38.
- van Assen, H., Danilouchkine, M., Dirksen, M., Reiber, J., Lelieveldt, B., 2008. A 3-D Active Shape Model Driven by Fuzzy Inference: Application to Cardiac CT and MR. *IEEE Trans. Inf. Technol. Biomed.* 12 (5), 595–605.
- van Bommel, J. H., Kors, J. A., van Herpen, G., 1990. Methodology of the Modular ECG Analysis System MEANS. *Methods Inf. Med.* 29 (4), 346–353.
- van de Kraats, E., Penney, G., Tomazevic, D., van Walsum, T., Niessen, W., 2005. Standardized Evaluation Methodology for 2-D-3-D Registration. *IEEE Trans. Med. Imaging* 24 (9), 1177–1189.
- van Ginneken, B., Heimann, T., Styner, M., 2007. 3D Segmentation in the Clinic: A Grand Challenge. In: *Proc. 3D Segmentation in the Clinic: A Grand Challenge workshop*, *Int. Conf. Med. Image Comput. Comput. Assist. Interv.* pp. 7–15.
- van Walsum, T., Schaap, M., Metz, C., van der Giessen, A., Niessen, W., 2008. Averaging Center Lines: Mean Shift on Paths. In: *Proc. Int. Conf. Med. Image Comput. Comput. Assist. Interv.* Vol. 5241 of *Lect. Notes Comput. Sci.* pp. 900–907.
- Vandemeulebroucke, J., Sarrut, D., Clarysse, P., 2007. The POPI-Model, a Point-Validated Pixel-Based Breathing Thorax Model. In: *Proc. Int. Conf. Comput. in Radiat. Ther.*
- Wang, C., Smedby, O., 2007. Coronary Artery Segmentation and Skeletonization Based on Competing Fuzzy Connectedness Tree. In: *Proc. Int. Conf. Med. Image Comput. Comput. Assist. Interv.* Vol. 4791 of *Lect. Notes Comput. Sci.* pp. 311–318.




- Wang, C., Smedby, O., 2008. An Automatic Seeding Method For Coronary Artery Segmentation and Skeletonization in CTA. Midas J. - Proc. MICCAI Workshop - Grand Challenge Coronary Artery Tracking, <<http://hdl.handle.net/10380/1434>>.
- Wang, J. C., Normand, S.-L. T., Mauri, L., Kuntz, R. E., 2004. Coronary Artery Spatial Distribution of Acute Myocardial Infarction Occlusions. *Circulation* 110 (3), 278–284.
- Warfield, S., Zou, K., Wells, W., 2004. Simultaneous Truth and Performance Level Estimation (STAPLE): An Algorithm for the Validation of Image Segmentation. *IEEE Trans. Med. Imaging* 23 (7), 903–921.
- Wesarg, S., Firle, E., 2004. Segmentation of Vessels: The Corkscrew Algorithm. In: *Proc. SPIE Med Imaging: Image Process.* pp. 1609–1620.
- Wesarg, S., Khan, M. F., Firle, E. A., 2006. Localizing Calcifications in Cardiac CT Data Sets Using a New Vessel Segmentation Approach. *J. Digital Imaging* 19 (3), 249–257.
- West, J., Fitzpatrick, J. M., Wang, M. Y., Dawant, B. M., Maurer, C. R., Kessler, R. M., Maciunas, R. J., Barillot, C., Lemoine, D., Collignon, A., Maes, F., Suetens, P., Vandermeulen, D., van den Elsen, P. A., Napel, S., Sumanaweera, T. S., Harkness, B., Hemler, P. F., Hill, D. L., Hawkes, D. J., Studholme, C., Maintz, J. B., Viergever, M. A., Malandain, G., Woods, R. P., 1997. Comparison and Evaluation of Retrospective Intermodality Brain Image Registration Techniques. *J. Comput. Ass. Tomogr.* 21 (4), 554–566.
- Weustink, A. C., Mollet, N. R., Neeffes, L. A., Meijboom, W. B., Galema, T. W., van Mieghem, C. A., Kyrzopoulos, S., Eu, R. N., Nieman, K., Cademartiri, F., van Geuns, R.-J., Boersma, E., Krestin, G. P., de Feyter, P. J., 2010. Diagnostic Accuracy and Clinical Utility of Noninvasive Testing for Coronary Artery Disease. *Ann. Intern. Med.* 152 (10), 630–639.
- Weustink, A. C., Mollet, N. R., Neeffes, L. A., van Straten, M., Neoh, E., Kyrzopoulos, S., Meijboom, B. W., van Mieghem, C., Cademartiri, F., de Feyter, P. J., Krestin, G. P., 2009. Preserved Diagnostic Performance of Dual-Source CT Coronary Angiography With Reduced Radiation Exposure and Cancer Risk. *Radiology* 252 (1), 53–60.
- Weustink, A. C., Mollet, N. R., Pugliese, F., Meijboom, W. B., Nieman, K., Heijnenbroek-Kal, M. H., Flohr, T. G., Neeffes, L. A. E., Cademartiri, F., de Feyter, P. J., Krestin, G. P., 2008. Optimal Electrocardiographic Pulsing Windows and Heart Rate: Effect on Image Quality and Radiation Exposure at Dual-Source Coronary CT Angiography. *Radiology* 248 (3), 792–798.
- Wierzbicki, M., Drangova, M., Guiraudon, G., Peters, T., 2004. Validation of Dynamic Heart Models Obtained Using Non-Linear Registration for Virtual Reality Training, Planning, and Guidance of Minimally Invasive Cardiac Surgeries. *Med. Image Anal.* 8 (3), 387–401.
- Wink, O., Frangi, A., Verdonck, B., Viergever, M., Niessen, W., 2002. 3D MRA Coronary Axis Determination Using a Minimum Cost Path Approach. *Magn. Reson. Med.* 47 (6), 1169–1175.
- Wink, O., Niessen, W., Verdonck, B., Viergever, M., 2001. Vessel Axis Determination Using Wave Front Propagation Analysis. In: *Proc. Int. Conf. Med. Image Comput. Comput. Assist. Interv. Vol. 2208 of Lect. Notes Comput. Sci.* pp. 845–853.
- Wink, O., Niessen, W., Viergever, M., 2000a. Fast Delineation and Visualization of Vessels in 3-D Angiographic Images. *IEEE Trans. Med. Imaging* 19, 337–346.
- Wink, O., Niessen, W., Viergever, M., 2000b. Minimum Cost Path Determination Using a Simple Heuristic Function. In: *Proc. Int. Conf. Pattern Recog.* pp. 998–1001.
- Wink, O., Niessen, W., Viergever, M., 2004. Multiscale Vessel Tracking. *IEEE Trans. Med. Imaging* 23 (1), 130–133.
- Wong, W., Chunga, A., 2007. Probabilistic Vessel Axis Tracing and Its Application to Vessel Segmentation With stream surfaces and minimum cost paths. *Med. Image Anal.* 11 (6), 567–587.

- Woolf, N., 1998. Pathology: Basic and Systemic. W.B. Saunders.
- World Health Organization, 2007. The Top Ten Causes of Death - Fact Sheet N° 310.
- World Health Organization, 2009. The Top Ten Causes of Death - Fact Sheet N° 317.
- Xu, C., Prince, J. L., 1998. Snakes, Shapes, and Gradient Vector Flow. *IEEE Trans. Image Process.* 7 (3), 359–369.
- Xue, H., Guehring, J., Srinivasan, L., Zuehlsdorff, S., Saddi, K., Chefdhotel, C., Hajnal, J. V., Rueckert, D., 2008. Evaluation of Rigid and Non-Rigid Motion Compensation of Cardiac Perfusion MRI. In: *Proc. Int. Conf. Med. Image Comput. Comput. Assist. Interv.* Vol. 5242 of *Lect. Notes Comput. Sci.* pp. 35–43.
- Yang, D., Lu, W., Low, D. A., Deasy, J. O., Hope, A. J., Naqa, I. E., 2008. 4D-CT Motion Estimation Using Deformable Image Registration and 5D Respiratory Motion Modeling. *Med. P* 35 (10), 4577–4590.
- Yang, G., Bousse, A., Toumoulin, C., Shu, H., 2006. A Multiscale Tracking Algorithm for the Coronary Extraction in MSCT Angiography. In: *Proc. IEEE Eng. Med. Biol. Soc.* pp. 3066–3069.
- Yang, G., Zhou, J., Boulmier, D., Garcia, M.-P., Luo, L., Toumoulin, C., 2010. Characterization of 3-D Coronary Tree Motion from MSCT Angiography. *IEEE Trans. Inf. Technol. Biomed.* 14 (1), 101–106.
- Yang, Y., Tannenbaum, A., Giddens, D., 2007. Automatic Segmentation of Coronary Arteries Using Bayesian Driven Implicit Surfaces. In: *Proc. IEEE Int. Symp. Biomed. Imaging.* pp. 856–859.
- Yang, Y., Zhu, L., Haker, S., Tannenbaum, A. R., Giddens, D. P., 2005. Harmonic Skeleton Guided Evaluation of Stenoses in Human Coronary Arteries. In: *Proc. Int. Conf. Med. Image Comput. Comput. Assist. Interv.* Vol. 3749 of *Lect. Notes Comput. Sci.* pp. 490–497.
- Yoo, T., Ackerman, M., Lorensen, W., Schroeder, W., Chalana, V., Aylward, S., Metaxes, D., Whitaker, R., 2002a. Engineering and Algorithm Design for an Image Processing API: A Technical Report on ITK - The Insight Toolkit.
- Yoo, T., Ackerman, M. J., Lorensen, W. E., Schroeder, W., Chalana, V., Aylward, S., Metaxes, D., Whitaker, R., 2002b. Engineering and Algorithm Design for an Image Processing API: A Technical Report on ITK - The Insight Toolkit. In: *Proc. Med. Meets Virtual Reality.* pp. 586–592.
- Zambal, S., Hladuvka, J., Kanitsar, A., Bühler, K., 2008. Shape and Appearance Models for Automatic Coronary Artery Tracking. *Midas J. - Proc. MICCAI Workshop - Grand Challenge Coronary Artery Tracking*, <<http://hdl.handle.net/10380/1420>>.
- Zanzonico, P., Rothenberg, L. N., Strauss, H. W., 2006. Radiation Exposure of Computed Tomography and Direct Intra-Coronary Angiography: Risk Has Its Reward. *J. Am. Coll. Cardiol.* 47 (9), 1846–1849.
- Zhang, D., Risser, L., Friman, O., Metz, C., Neefjes, L., Mollet, N., Niessen, W., Rueckert, D., 2010a. Nonrigid Registration and Template Matching for Coronary Motion Modeling From 4D CTA. In: *Proc. Int. Workshop Biomed. Image Regis.* Vol. 6204 of *Lect. Notes Comput. Sci.* pp. 210–221.
- Zhang, D., Risser, L., Metz, C., Neefjes, L., Mollet, N., Niessen, W., Rueckert, D., 2010b. Coronary Artery Motion Modeling From 3D Cardiac CT Sequences Using Template Matching and Graph Search. In: *Proc. IEEE Int. Symp. Biomed. Imaging.* pp. 1053–1056.
- Zhang, D., Risser, L., Vialard, F.-X., Edwards, P., Metz, C., Neefjes, L., Mollet, N., Niessen, W., Rueckert, D., 2010c. Coronary Motion Estimation From CTA Using Probability Atlas and Diffeomorphic Registration. In: *Proc. Int. Workshop Med. Imaging and Augm. Reality.* Vol. 6326 of *Lect. Notes Comput. Sci.* pp. 78–87.
- Zhang, H., Wahle, A., Johnson, R. K., Scholz, T. D., Sonka, M., 2010d. 4-D Cardiac MR Image Analysis: Left and Right Ventricular Morphology and Function. *IEEE Trans. Med* 29 (2), 350–364.



- Zhang, Y., Chen, K., Wong, S., 2008. 3D Interactive Centerline Extraction. Midas J. - Proc. MICCAI Workshop - Grand Challenge Coronary Artery Tracking, <<http://hdl.handle.net/10380/1417>>.
- Zhu, H., Ding, Z., Piana, R. N., Gehrig, T. R., Friedman, M. H., 2009. Cataloguing the Geometry of the Human Coronary Arteries: A Potential Tool for Predicting Risk of Coronary Artery Disease. *Int. J. Cardiol.* 135 (1), 43–52.
- Zikic, D., Groher, M., Khamene, A., Navab, N., 2008. Deformable Registration of 3D Vessel Structures to a Single Projection Image. In: *Proc. SPIE Med Imaging: Image Process.* pp. 691412–1–691412–12.
- Zöllei, L., Learned-Miller, E., Grimson, E., Wells, W., 2005. Efficient Population Registration of 3D Data. In: *Proc. Int. Workshop Comput. Vision Biomed. Image Appl.* pp. 291–301.

Samenvatting

The background of the page is a solid light gray. Overlaid on this background are several thin, white, hand-drawn style lines. These lines are abstract and fluid, starting from the left edge and extending across the page. Some lines are relatively straight, while others are highly curved and looping. There are approximately 10-12 distinct line elements, some of which are parallel to each other, creating a sense of movement and depth. The lines vary in length and orientation, with some extending from the top left towards the bottom right, and others more horizontal or vertical.

In dit proefschrift beschreven we de ontwikkeling en evaluatie van technieken voor het relateren van diagnostische CTA-scans aan intraoperatieve röntgenangiografie beelden. We introduceerden een strategie gebaseerd op het modelleren van de patiënt-specifieke vorm en beweging van de kransslagaderen. Deze bewegingsmodellen werden geëxtraheerd uit 4D cardiale CTA-beelden door de vorm van de kransslagaders op één tijdpunt te bepalen en de beweging met behulp van registratie af te leiden uit de complete 4D scan. Vervolgens werden deze modellen gerelateerd aan de intraoperatieve röntgenangiografie beelden, waarbij gelijktijdig meerdere tijdspunten werden meegenomen.

In de eerste hoofdstukken presenteerden we technieken die toegepast kunnen worden om een model van de kransslagaderbeweging te maken. In hoofdstuk 2 beschreven we de toepassing en evaluatie van kortstepadalgoritmes voor het vinden van de centrale as van de kransslagaders in 3D CTA-beelden. We toonden met een kwantitatieve evaluatie op 48 kransslagaders aan dat de methode in 88% van de gevallen de centrale as correct lokaliseerde. De gevonden locatie week gemiddeld 0.64 mm af van de daadwerkelijke locatie. Een extra evaluatie op 252 kransslagaders in 63 andere CTA-beelden liet zien dat de methode in 233 van de 252 gevallen in staat was de kransslagaders te lokaliseren.

Naast ons werk uit hoofdstuk 2 zijn in de literatuur meerdere methoden beschreven voor het (semi-)automatisch vinden van de kransslagaders in CTA-scans. Er was echter geen gestandaardiseerde manier om deze methodes en nieuw te ontwikkelen methodes te evalueren en vergelijken. In hoofdstuk 3 presenteerden we daarom een gestandaardiseerd evaluatieraamwerk voor methodes die de centrale as van de kransslagaders in CTA-beelden vinden. Dit raamwerk bestaat uit 32 publiek beschikbare CTA-scans, een referentiestandaard die is afgeleid uit het handmatig aangeven van de centrale assen en duidelijk gedefinieerde evaluatiematen. We vergeleken 13 verschillende technieken die door onderzoeksgroepen wereldwijd geïmplementeerd zijn en lieten daarmee de toepasbaarheid van het raamwerk zien. Op dit moment staan meer dan 100 teams ingeschreven om gebruik te kunnen maken van de data en de evaluatiemethode. Voor het publiceren van nieuwe resultaten in toonaangevende wetenschappelijke tijdschriften is het noodzakelijk dit raamwerk te gebruiken voor het evalueren van de beschreven methode.

Gebruikmakend van de methodes uit hoofdstuk 2 of één van de methodes die geëvalueerd zijn in hoofdstuk 3 kan een statisch model van de kransslagaderen worden bepaald, bijvoorbeeld voor de einddiastole fase van de hartslag. Om een dynamisch model voor de complete hartcyclus te maken moet echter ook de beweging van de kransslagaders worden bepaald. In hoofdstuk 4 presenteerden we een methode die de beweging van anatomie in medische beelden kan bepalen. De methode bepaalt de beweging voor alle tijdspunten gelijktijdig zodat er geen voorkeur naar een bepaald tijdpunt ontstaat en houdt zowel rekening met spatiële en temporele gladheid van het resultaat. Daarnaast kan de methode afdwingen dat de afgeschatte beweging cyclisch verloopt. De methode gebruikt een 3D (2D+tijd) of 4D (3D+tijd) B-spline transformatiemodel, een similariteitsmaat die de variatie van de intensiteit over tijd meet en begrensd optimalisatie met een stochastische gradiëntdalingsmethode waarin de stapgrootte automatisch wordt bijgesteld. Kwantitatieve evaluatie toonde aan dat de methode de beweging kan vinden met een afwijking die kleiner is dan de grootte van de voxels in het beeld en consistente

resultaten oplevert.

Het bepalen van een 4D kransslagadermodel door de vorm van de slagaders te vinden op één tijdpunt van de hartslag en die te combineren met een bewegingsmodel is een voor de hand liggende aanpak wanneer dynamische beelden beschikbaar zijn. De toename in de stralingsdosis voor het maken van deze dynamische beelden is echter niet altijd te verantwoorden. Er wordt daarom steeds meer gebruik gemaakt van prospectieve gating tijdens het scannen. Dit betekent dat alleen gescand wordt in een vooraf bepaalde fase van de hartslag, in plaats van tijdens de hele hartslag. Dit levert een aanzienlijke vermindering van de stralingsdosis op, maar er kan tegelijkertijd maar één 3D beeld gemaakt worden. Daarom ontwikkelden we in hoofdstuk 5 een methode voor het voorspellen van hartbeweging op basis van de vorm van het hart. Deze methode is gebaseerd op hoofdcomponentenregressie en statistische modellen van zowel de vorm als de beweging van het hart. Onze hypothese was dat de beweging van het hart in tenminste bepaalde mate afhangt van zijn vorm. Kwantitatieve evaluatie op 150 4D CTA-beelden toonde aan dat het op deze manier meenemen van de vorm in het voorspellen van de beweging een kleine, maar significante verbetering opleverde ten opzichte van vormonafhankelijke bewegingsafschatting.

In het laatste hoofdstuk onderzochten we de haalbaarheid van een 3D+tijd/2D+tijd registratie methode voor het relateren van diagnostische CTA-scans aan de röntgenangiografie beelden van een interventie. We pasten de methodes uit de voorgaande hoofdstukken toe voor het modelleren van de beweging van de kransslagaders en registreerden dit 4D kransslagadermodel temporeel met de intraoperatieve situatie door het relateren van ECG signalen. Daarna bepaalden we de positie en oriëntatie van het model ten opzichte van de patiënt. Een niet-lineaire geconjugeerde gradiënt-methode werd gebruikt voor het optimaliseren van een similariteitsmaat op basis van het projecteren van de centrale assen uit het model en een grove segmentatie van de röntgenbeelden. De registratie werd gelijktijdig uitgevoerd voor alle röntgenbeelden binnen één hartslag, waarbij ook de rotatie en verplaatsing van het hart door de ademhaling werd meegenomen. De methode werd geëvalueerd door geprojecteerde assen uit het kransslagadermodel te vergelijken met handmatig, in de röntgenbeelden aangegeven, assen. We lieten zien dat de gepresenteerde strategie voordelen heeft ten opzichte van een 3D/2D registratie methode wat betreft het succespercentage en de reproduceerbaarheid van de resultaten.

Ten slotte concluderen we dat de gepresenteerde registratie methodologie, gebaseerd op het modelleren van de kransslagaderbeweging, een veelbelovende strategie is voor het relateren van preoperatief gemaakte CTA beelden en intraoperatieve röntgenangiografie.

The background of the page is a solid light gray. Overlaid on this background are several thin, white, wavy lines that flow from the top left towards the bottom right. These lines vary in length and curvature, creating a sense of movement and depth. Some lines are more horizontal, while others are more vertical or diagonal. They appear to be layered, with some lines crossing over others, giving the impression of a complex, organic structure.

Publications

Journal Papers

- M. Schaap, **C.T. Metz**, T. van Walsum, A.G. van der Giessen, A.C. Weustink, N.R.A. Mollet, C. Bauer, H. Bogunović, C. Castro, X. Deng, E. Dikici, T. O'Donnell, M. Frenay, O. Friman, M. Hernández Hoyos, P.H. Kitslaar, K. Krissian, C. Kühnel, M. A. Luengo-Oroz, M. Orkisz, Ö. Smedby, M. Styner, A. Szymczak, H. Tek, C. Wang, S. K. Warfield, S. Zambal, Y. Zhang, G. P. Krestin and W.J. Niessen, Standardized Evaluation Methodology and Reference Database for Evaluating Coronary Artery Centerline Extraction Algorithms, *Medical Image Analysis*, 13/5: 701–714, 2009.
- **C.T. Metz**, M. Schaap, A.C. Weustink, N.R.A. Mollet, T. van Walsum and W.J. Niessen, Coronary Centerline Extraction from CT Coronary Angiography Images Using a Minimum Cost Path Approach, *Medical Physics*, 36(12): 5568–5579, 2009.
- **C.T. Metz**, S. Klein, M. Schaap, T. van Walsum and W.J. Niessen, Nonrigid Registration of Dynamic Medical Imaging Data Using nD+t B-splines and a Groupwise Optimization Approach, *Medical Image Analysis*, 15(2): 238–249, 2011.
- K. Hameeteman, M.A. Zuluaga, M. Freiman, L. Joskowicz, O. Cuisenaire, L. Flórez Valencia, M.A. Gülsün, K. Krissian, J. Mille, W.C.K. Wong, M. Orkisz, H. Tek, M. Hernández Hoyos, F. Benmansour, A.C.S. Chung, S. Rozie, M. van Gils, L. van den Borne, J. Sosna, P. Berman, N. Cohen, P.C. Douek, I. Sánchez, M. Aissat, M. Schaap, **C.T. Metz**, G.P. Krestin, A. van der Lugt, W.J. Niessen and T. van Walsum, Evaluation Framework for Carotid Bifurcation Lumen Segmentation and Stenosis Grading *Medical Image Analysis*, *in press*.
- M. Schaap, T. van Walsum, M. de Bruijne, L.A. Neefjes, **C.T. Metz**, E. Capuano and W.J. Niessen, Robust Shape Regression for Supervised Vessel Segmentation and its Application to Coronary Segmentation in CTA, *submitted*.
- **C.T. Metz**, N. Baka, H. Kirisli, M. Schaap, S. Klein, L.A. Neefjes, N.R. Mollet, B. Lelieveldt, M. de Bruijne, W.J. Niessen and T. van Walsum, Cardiac Motion Prediction from Single-Phase CTA by Principle Component Regression, *submitted*.
- A. Firouzian, R. Manniesing, **C.T. Metz**, R. Risselada, S. Klein, F. van Kooten, M.C. Sturkenboom, A. van der Lugt, W.J. Niessen, Quantification of Intracranial Aneurysm Morphodynamics from ECG-Gated CT Angiography, *submitted*.
- **C.T. Metz**, M. Schaap, S. Klein, P.R. Rijnbeek, L.A. Neefjes, N.R. Mollet, C. Schultz, P.W. Serruys, W.J. Niessen, T. van Walsum, Alignment of 4D Coronary CTA with Monoplane X-Ray Angiography: A Feasibility Study, *in preparation*.

Conference Papers

- E. Vansteenkiste, **C.T. Metz**, P. Govaert, W.J. Niessen and W. Philips, Preterm Brain Ventricle Reconstruction from 3D Ultrasound Volumes, *3rd annual IEEE Benelux/DSP Valley Signal Processing Symposium - SPS-DARTS*, pages 167–172, 2007.



- **C.T. Metz***, M. Schaap*, A.G. van der Giessen, T. van Walsum and W.J. Niessen, Semi-Automatic Coronary Artery Centerline Extraction in Computed Tomography Angiography Data, *4th IEEE International Symposium on Biomedical Imaging: From Nano to Macro - ISBI*, pages 856–859, 2007. *: joint first authorship.
- M. Schaap, I. Smal, **C.T. Metz**, T. van Walsum and W.J. Niessen, Bayesian Tracking of Elongated structures in 3D Images, *20th International Conference on Information Processing in Medical Imaging - IPMI*, 74–85, 2007.
- T. van Walsum, M. Schaap, **C.T. Metz**, A.G. van der Giessen and W.J. Niessen, Averaging Centerlines: Mean Shift on Paths, *11th International Conference on Medical Image Computing and Computer Assisted Intervention - MICCAI*, pages 900–907, 2008.
- **C.T. Metz**, M. Schaap, T. van Walsum and W.J. Niessen, Two Point Minimum Cost Path Approach for CTA Coronary Centerline Extraction, *3D Segmentation in the Clinic: a Grand Challenge II: MICCAI 2008 workshop*, 2008.
- M. Schaap, L. Neefjes, **C.T. Metz**, A.G. van der Giessen, A.C. Weustink, N.R.A. Mollet, J.J. Wentzel, T. van Walsum and W.J. Niessen, Coronary Lumen Segmentation using Graph Cuts and Robust Kernel Regression, *Information Processing in Medical Imaging*, pages 528–539, 2009.
- **C.T. Metz**, M. Schaap, S. Klein, A.C. Weustink, N.R.A. Mollet, C. Schultz, R.J. van Geuns, P.W. Serruys, T. van Walsum and W.J. Niessen, GPU Accelerated Alignment of 3-D CTA with 2-D X-Ray Data for Improved Guidance in Coronary Interventions, *6th IEEE International Symposium on Biomedical Imaging: From Nano to Macro - ISBI*, pages 959–962, 2009.
- M. Schaap, **C.T. Metz**, T. van Walsum, A.G. van der Giessen, A.C. Weustink, N.R.A. Mollet, G. P. Krestin and W.J. Niessen, On the Evaluation of Coronary Artery Centerline Extraction Algorithms - a Standardized Methodology and Reference Database, *11th World Congress 2009 on Medical Physics and Biomedical Engineering*, pages 1897–1900, 2009.
- **C.T. Metz**, M. Schaap, S. Klein, L. Neefjes, E. Capuano, C. Schultz, R.J. van Geuns, P.W. Serruys, T. van Walsum and W.J. Niessen, Patient Specific 4D Coronary Models from ECG-Gated CTA Data for Intra-Operative Dynamic Alignment of CTA with X-Ray Images, *12th International Conference on Medical Image Computing and Computer Assisted Intervention - MICCAI*, pages 369–376, 2009.
- D.P. Zhang, L. Risser, **C.T. Metz**, L. Neefjes, N.R.A. Mollet, W.J. Niessen and D. Rueckert, Coronary Artery Motion Modeling from 3D Cardiac CT Sequences Using Template Matching and Graph Search, *7th IEEE International Symposium on Biomedical Imaging: From Nano to Macro - ISBI*, pages 1053–1056, 2010.

- K. Hameeteman, S. Rozie, **C.T. Metz**, S. Klein, T. van Walsum, A. van der Lugt and W.J. Niessen, Automated Carotid Artery Distensibility Measurements from CTA Using Nonrigid Registration, *7th IEEE International Symposium on Biomedical Imaging: From Nano to Macro - ISBI*, pages 13–16, 2010.
- D.P. Zhang, L. Risser, O. Friman, **C.T. Metz**, L. Neefjes, N.R.A. Mollet, W.J. Niessen and D. Rueckert, Nonrigid Registration and Template Matching for Coronary Motion Modeling from 4D CTA, *4th International Workshop on Biomedical Image Registration - WBIR*, pages 210–221, 2010.
- **C.T. Metz***, N. Baka*, H.A. Kirisli, M. Schaap, T. van Walsum, S. Klein, L. Neefjes, N.R.A. Mollet, B.P.F. Lelieveldt, M. de Bruijne and W.J. Niessen, Conditional Shape Models for Cardiac Motion Estimation, *13th International Conference on Medical Image Computing and Computer Assisted Intervention - MICCAI*, pages 452–459, 2010. *: joint first authorship.
- D.P. Zhang, L. Risser, F.-X. Vialard, P. Edwards, **C.T. Metz**, L. Neefjes, N.R.A. Mollet, W.J. Niessen and D. Rueckert, Coronary Motion Estimation from CTA Using Probability Atlas and Diffeomorphic Registration, *5th International Workshop on Medical Imaging and Augmented Reality, MIAR*, pages 78–87, 2010.

Conference Abstracts

- **C.T. Metz**, M. Schaap, N.R.A. Mollet, T. van Walsum and W.J. Niessen, Semi-Automatic Multi Planar Reformatting of the Coronary Arteries from Computed Tomography Angiography Data, *European Congress of Radiology*, 2008.
- **C.T. Metz**, M. Schaap, S. Klein, E. Capuano, L. Neefjes, T. van Walsum and W.J. Niessen, Extracting Coronary Artery Motion from ECG-Pulsed and Gated CTA Data, *Radiological Society of North America, 95th Annual Meeting*, 2009.
- A.A. Isola, **C.T. Metz**, M. Schaap, S. Klein, W.J. Niessen and M. Grass, Coronary Segmentation Based Motion Corrected Cardiac CT Reconstruction, *IEEE Nuclear Science Symposium and Medical Imaging Conference - NSS-MIC*, 2010.

Workshop Proceedings

- **C.T. Metz***, M. Schaap*, T. van Walsum, A.G. van der Giessen, A.C. Weustink, N.R.A. Mollet, G. P. Krestin and W.J. Niessen, Editorial: 3D Segmentation in the Clinic: A Grand Challenge II - Coronary Artery Tracking, *MICCAI 2008 workshop*, 2008. *: joint first authorship.



Patents

- **C.T. Metz**, M. Schaap, T. van Walsum and W.J. Niessen, Image Processing Method and System, W.I.P.O. Patent Application, Application nr. PCT/NL2009/050549, filed September 14, 2009.

PhD portfolio

PhD period: 2006 – 2011
Departments: Radiology & Medical Informatics
Research schools: ASCI, COEUR.

Courses

Introduction to Data Analysis (NIHES)	2006
Cardiovascular Imaging and Diagnostics (COEUR)	2006
Front-End Vision and Multiscale Image Analysis (ASCI)	2006
MeVisLab Introduction Course	2006
Angina Pectoris (curriculum Health Sciences)	2007
Advanced Pattern Recognition (ASCI)	2008
Heart Failure (COEUR)	2008
Knowledge-Driven Image Segmentation (ASCI)	2009
Principles in Research and Medicine (NIHES)	2009

International Conferences (attendance/presentation)

IEEE International Symposium on Biomedical Imaging - ISBI, Washington, USA (poster presentation)	2007
Medical Image Computing and Computer-Assisted Intervention - MICCAI, New York, USA (workshop organization)	2008
European Congress of Radiology 2008 - ECR, Vienna, Austria (oral presentation)	2008
Medical Image Computing and Computer-Assisted Intervention, London, UK - MICCAI (poster presentation)	2009
IEEE International Symposium on Biomedical Imaging - ISBI, Boston, USA (poster presentation)	2009
Annual Meeting of the Radiological Society of North America - RSNA, Chicago, USA (oral presentation)	2009
IEEE International Symposium on Biomedical Imaging - ISBI, Rotterdam, The Netherlands (attendance)	2010
Medical Image Computing and Computer-Assisted Intervention - MICCAI, Beijing, China (poster presentation)	2010

Seminars and Workshops

Machine Learning for Biomedical Image Analysis, Rotterdam, The Netherlands	2006/2007
Feature extraction and classification, Washington, USA	2007
Image Guidance and Computer Assistance for Soft-Tissue Interventions, New York, USA	2008
Advanced MeVisLab Developers' Workshop, Bremen, Germany	2009
Statistical Shape Analysis: Theory, Software, and Applications, Boston, USA	2009
Geometric accuracy in image guided intervention, Boston, USA	2009
Image-guided Interventions: Technology and Applications, London, UK	2009
Spatio-Temporal Image Analysis for Longitudinal and Time-Series Image Data, Beijing, China	2010
Ultrasound imaging and therapeutics, Rotterdam, The Netherlands	2010

Other

Organization of international workshop: '3D Segmentation in the Clinic: a Grand Challenge II', New York, USA	2008
Demonstrations at the Medical Delta booth at ECR, Vienna, Austria	2008
Reviewing for International Journal of Computer Assisted Radiology and Surgery and the International Conference on Medical Image Computing and Computer-Assisted Intervention	2010 - now

Other presentations

Advanced MeVisLab Developers' Workshop	2009
Research seminars Biomedical Imaging Group Rotterdam (5x), Department of Medical Informatics (3x) and Department of Radiology (2x)	2006 - 2011
Medical Informatics PhD days	2007
Medical Imaging Symposium for PhD students	2010
Several other presentations at (inter)national meetings with researchers and industry	2006-2011

Dankwoord

Het proefschrift en de stellingen zijn goedgekeurd, de voorkant en lay-out zijn klaar en de drukker is geregeld. Toch zit ik weer achter de computer; het dankwoord moet nog geschreven worden. En ook al lijkt dat misschien relatief eenvoudig vergeleken met het schrijven van wetenschappelijke artikelen - er komen immers niet één (of meerdere) tijdrovende review rondes aan te pas voordat het gepubliceerd wordt -, toch is het lastiger dan gedacht. Dit gedeelte schrijf je namelijk echt alleen, kan opeens wel in het Nederlands en is waarschijnlijk het meest gelezen gedeelte van een proefschrift.

Promoveren is een leertraject en ik besef dat ik enorm veel geleerd heb in de afgelopen jaren. Heel wat artikelen, boeken, cursussen, conferenties en seminars later verwacht je dat natuurlijk ook wel. Toch leer je misschien wel het meeste van de mensen waar je mee samenwerkt.

Mijn promotor, professor Niessen. Beste Wiro, bedankt dat je me de kans gaf om na het ultrasound project aan dit promotieonderzoek te beginnen. Toen ik als research assistent in 2005 bij BIGR kwam, telde de groep 4 onderzoekers in opleiding. Inmiddels zijn er al een aantal gepromoveerd en nog 20 hard aan het werk. Het is bewonderenswaardig hoe je in korte tijd BIGR op de kaart hebt gezet. Ik heb erg geprofiteerd van jouw overzicht van het vakgebied, je scherpe inzichten tijdens besprekingen en snelle reacties op artikelen. Je gevoel voor humor en je enthousiasme maakt(e) BIGR tot een plezierige plek om te werken.

Mijn co-promotor, Theo van Walsum. Jouw enthousiasme voor beeldgeleide interventies is aanstekelijk! Hartelijk dank voor alle uren dat we mijn project besproken, zowel in grote lijnen als in detail. De snelle correcties op mijn artikelen en jouw inzicht bij het oplossen van praktische problemen hebben me erg geholpen.

De kleine commissie, professor van der Steen, professor Reiber en professor Breeuwer, wil ik bedanken voor het lezen en beoordelen van mijn proefschrift. Uiteraard gaat mijn dank ook uit naar de extra leden voor de grote commissie.

Het was een voorrecht (tijdelijke) kamergenoten te hebben die hetzelfde traject met ongeveer dezelfde tijdsplanning doorliepen. Michiel, ik denk dat je bijna net zoveel over mijn proefschrift weet als ik zelf. Ik wil je hartelijk bedanken voor alle discussies die we hadden over onze onderzoeksprojecten en de gesprekken over het plezier en de frustratie die soms met onderzoek gepaard gaat. Ik heb erg veel profijt gehad en geleerd van je wetenschappelijk inzicht, snelheid van denken en innovatieve ideeën. Renske, je begon 2 weken later dan ik met je promotieonderzoek, maar bent uiteindelijk toch 1,5 week eerder gepromoveerd. Respect! Het was erg leuk om zo gelijk op te lopen en daarover van gedachten te wisselen. Bedankt ook voor alle initiatieven op het BIGR-social vlak!

Stefan, ik heb met veel plezier samen met jou aan het registratie hoofdstuk gewerkt. De praktijk was soms weerbarstiger dan de theorie wat tot interessante discussies

leidde. Het gemak waarmee jij de afgeleide van een kostenfunctie uitschrijft is bewonderenswaardig. Hartelijk dank voor alle tijd die je in dit project, maar ook in de laatste twee hoofdstukken van mijn proefschrift hebt gestoken!

I would also like to thank my C-VIP and IGI colleagues: Rahil, Nora and Hortense. Nora and Hortense, it was fun to work together on the motion estimation project. Thanks for your commitment; the fruitful discussions and the hard work in a very limited amount of time! Ook Marleen en Boudewijn wil ik bedanken voor hun bijdrage aan dit hoofdstuk!

Reinhard, ondertussen zijn we al een aantal koffiezetapparaten verder, maar jij blijft een constante factor op de afdeling. Toen ik bij BIGH begon was je nog aan het afstuderen, maar inmiddels ben je ook aan het promoveren. Het was (en is) erg leuk om tijdens de koffiepauzes, onder het genot van een goede (of soms wat minder goede) kop koffie, van gedachten te wisselen.

Marcel van Straten, ik heb erg genoten van de trip naar de RSNA in Chicago. Bedankt voor het rondleiden en de gezelligheid!

I would also like to thank all other people from BIGH and the people from the departments of Medical Informatics and Radiology. I enjoyed working in such an inspiring environment in which multiple disciplines meet. Thanks also for the nice social gatherings. Petra Assems en Desiree de Jong: bedankt voor jullie hulp bij de administratieve zaken tijdens en bij het afronden van mijn promotieonderzoek.

Het grote voordeel van het werken in een academisch medisch centrum is het directe contact met de kliniek. Dat is niet alleen essentieel om data voor je onderzoek te verzamelen, maar ook om erachter te komen wat echt relevant is. Dank gaat daarom naar de mensen van de cardio-radiologie groep: professor de Feijter, Nico Mollet, Annick Weustink, Lisan Neeffjes en Ermanno Capuano. Hartelijk bedankt voor de hulp bij het verzamelen van data en een kijkje in de keuken van de radiologie. Ook de collega's van interventie cardiologie wil ik bedanken: professor Serruys, Robert Jan van Geuns en Carl Schultz. Naast de altijd beschikbare data, waren de vele discussies die we gevoerd hebben erg nuttig voor mijn onderzoek. Samen met de CTO-meetings tussen onderzoekers en industrie, heeft het me erg geholpen om een beeld te vormen uitdagingen die jullie in de kliniek tegenkomen. Baie dankie! Van de afdeling Biomedical Engineering wil ik Alina van der Giessen, Hans Bosch en Esther Leung bedanken. Alina, bedankt voor je hand en spandiensten in de eerste 2 jaren van mijn promotieonderzoek. Hans en Esther, bedankt voor het enthousiasme over het registratiehoofdstuk en de bijdrage daaraan in de vorm van de ultrasound data. Voor deze data gaat mijn dank ook uit naar W. Vletter van de afdeling cardiologie. Professor Tiddens en Riccarda Failo van de afdeling Pediatric Radiology and Pulmonology wil ik bedanken voor het mogen gebruiken van de MR ademhalingsbeelden.

Ook buiten de werksfeer zijn er mensen waar mijn dank naar uit gaat. Onder andere vrienden. Het was heerlijk om gezellige avonden, dagen of weekenden te plannen, waarin we het over van alles en nog wat (maar vooral niet te veel over de details van mijn onderzoek) konden hebben. Hetzelfde geldt natuurlijk voor mijn familie. Ook bij jullie kon ik even mijn werk achter me laten en genieten van de gezelligheid. Bedankt ook voor jullie interesse in mijn werk door de jaren heen. Het is boeiend om te zien hoe iedereen zijn eigen weg gaat en erg leuk om daar van gedachten over te wisselen. Gijsbert en Matthijs: erg leuk dat jullie mijn paranimfen willen zijn. Bedankt!



Tenslotte: Annelene. Bedankt dat je er altijd voor me bent! Je hebt me de ruimte gegeven om over te kunnen werken voor deadlines, thuis met papers voor mijn neus te zitten of je geregeld een week alleen achter te laten om naar conferenties te gaan. Ik kijk uit naar onze toekomst samen!

Coert Metz, April 2011.

Curriculum vitae

Coert Metz was born on February 26, 1981 in Ede, the Netherlands. He started his studies in Computer Science in 2000 at Utrecht University, the Netherlands. The last two years of his study he joined the Biomedical Image Sciences Master's program and received his M.Sc. degree in 2005.

The subject of his Master's thesis was the real-time computation of high-quality digitally reconstructed radiographs for radiology treatment planning. The project was carried out at Nucletron B.V, Veenendaal, the Netherlands.

After his graduation he worked for six months as a research assistant at the Biomedical Imaging Group Rotterdam (BIGR), Erasmus MC, the Netherlands, developing a 3D ultrasound acquisition protocol to image the neonatal brain.

In may 2006 he started working on his PhD project at BIGR on 'Coronary Motion Modeling for CTA to X-Ray Angiography Registration'. The results of this work are described in this thesis. After his defense, he will continue working as a post-doc researcher at BIGR, Erasmus MC, the Netherlands.

**CORONARY MOTION MODELING FOR
CTA TO X-RAY ANGIOGRAPHY REGISTRATION**

ISBN: 978-90-6464-473-3